



PhD's thesis XXXI Cycle

**SLOW DYNAMICS IN SUPERCOOLED
AQUEOUS SOLUTIONS FOR
CRYOPRESERVATION**

A Molecular Dynamics Study

Antonio Iorio

PhD Program Coordinator
Prof. Giuseppe Degrassi

Supervisor
Prof.ssa Paola Gallo

Department of Mathematics and Physics
Università degli Studi Roma Tre
Rome, Italy 2019

Contents

Introduction	5
1 Water	9
1.1 The water molecule	9
1.2 Anomalous properties of water	13
1.3 Supercooled and glassy water	17
1.4 Biological solutions	22
2 Dynamics of supercooled water	27
2.1 The Mode Coupling Theory	27
2.2 Fragile and Strong Liquids	36
3 Molecular Dynamics Simulations	41
3.1 Classical Molecular Dynamics simulations	41
3.2 Integrate the equations of motion	45
3.3 Thermostats and Barostats	50
3.4 Force fields and potentials	52
3.5 Ewald summation	53
3.6 The SPC/E model of water	55
3.7 The CHARMM FF for proteins, disaccharides and DMSO	56
3.8 MD observables	58
3.8.1 Dynamical quantities	58
3.8.2 Structural quantities	62
4 Water-Trehalose solutions	69
4.1 Systems and simulation details	69
4.2 Trehalose clusters	77
4.3 Translational dynamics	80
4.3.1 Relaxation times	89
4.4 The Dynamical Transition	94
4.5 Hydrogen Bonds	100

4.6	Conclusions	104
5	Lyso-Treha-DMSO aqueous solutions	107
5.1	Systems and simulation details	107
5.2	Translational dynamics of hydration water	115
5.2.1	Relaxation times	121
5.3	Mean Square displacement	125
5.4	Lysozyme-Water solution	128
5.5	Protein Dynamical Transition	130
5.6	Hydrogen Bonds	132
5.7	Conclusions	139
6	General conclusions	143
A	Parallel Implementation of HBs analysis code	147
B	List of Activities	151

Introduction

Water is one of the most common elements on Earth and plays a key role in many different and important physical, chemical and biological processes. Moreover water is one of the most prominent complex liquid that shows anomalies when cooled [1]. Supercooled liquids are liquids whose low temperature state is not solid even below their melting points. If the temperature of a liquid is lowered below the melting point fast enough, the dynamics of the system becomes so slow that it is not able to equilibrate on a time scale comparable with that of the experiment [2]. Such a system is said to undergo a glass transition.

Thermodynamic and dynamic properties of supercooled water present rather unusual characteristics, like for example the increase of some response function (isothermal compressibility and isobaric heat capacity) [3], and all these features are enhanced upon cooling. It is thought that such a behaviour stems from the fundamental role played by the hydrogen bonds between water molecules [4, 5]. Moreover water presents at least two different states in the glassy region, characterized by different density and entropy (polyamorphism). Up to now there are several different scenarios proposed to account for its puzzling behaviour [1].

From a dynamical point of view the most prominent microscopic theory that is able to partially explain water behaviour upon supercooling is the Mode Coupling Theory [6]. MCT was initially developed in the framework of simple liquids but its predictions are remarkably good also in explaining the glassy dynamic of supercooled water [7, 8]. According to MCT, such a behaviour is due to the temporary confinement of a molecule of water in a cage composed of other neighbour molecules.

There are several ways to study the properties of water, however all these experimental techniques have to overcome the important problem of a crystallization time that is much shorter than the typical experimental time, especially in the deep supercooled region. Some of the methods used to prevent crystallization are confined water and aqueous solutions [1]. A way to

approach the problem is through computer simulations [9] where fast cooling rates prevent crystallization. Using molecular dynamics algorithms one can probe different points of the phase space and sample many thermodynamic and dynamic quantities.

The aim of this work is to characterize some of the properties of supercooled water close to the surface of biomolecules in the supercooled region and how to exploit these properties for cryopreservation.

This Thesis is divided in two main parts. The first part is focused on dynamical and structural properties of two different aqueous solutions of trehalose [10], a disaccharide. These solutions are very common in nature and their interesting properties may help to understand the anomalies of supercooled water, e.g. how the disruption of water hydrogen bonds due to the presence of other molecules may affect the dynamic of supercooled water. Moreover aqueous solutions of this kind are relevant in many technological applications, such as cryopreservation of organic molecules [11, 12]. In this context, trehalose has been proven to be especially effective. When added to a solution of water, trehalose is able to slow down the dynamic of water near the surface of a biomolecule and to change the arrangement of nearby water molecules. One of the possible explanation of the cryoprotecting ability of trehalose is that molecules of this disaccharide arrange themselves around a biomolecule preventing the crystallization of the hydration water upon cooling, thus avoiding the damage of organic molecules [12, 13]. It is thus interesting to study trehalose in its interaction with water molecules in order to better understand their mutual influence.

The second part of this work is about the investigation of the interesting properties of aqueous solutions of trehalose in a solutions composed of a protein (in this case lysozyme), trehalose and dimethyl sulfoxide (DMSO). Dimethyl sulfoxide is a relatively simple molecule that is widely used in medicine as cryoprotectant. Unfortunately DMSO is also know to be harmful to the cells at high concentration, thus it will be useful to exploit the combined properties of a mixture of trehalose and DMSO to diminish the concentration of the latter. Mixture of DMSO and trehalose are already used in cryopreservation to exploit their combined action in the reduction of osmotic pressure and ice crystals formation. Moreover they act synergistically as intracellular and extracellular cryoprotecting agents.

This Thesis is structured in the following way.

In **Chapter 1** an overview of the intriguing properties of water is reported. This Chapter presents some of the anomalies of water, together with their connection with the ability of water molecules to form hydrogen bonds and the resulting phase diagram. A brief introduction on supercooled and glassy states is given. At the end of the Chapter the importance of water in the biological context is described.

Chapter 2 is devoted to Mode Coupling Theory. This is the framework in which some of the results of this work are analyzed. A sketch of the derivation of the Mode Coupling Theory equations is presented, together with the main physical idea behind the ability of this theory to explain glassy dynamics of supercooled liquids.

In **Chapter 3** illustrates the methodology used in this work. The main elements of the Molecular Dynamics technique are presented: an algorithm for the integration of the equations of motion, how to constraint pressure and temperature during a simulation and how to handle the interaction potentials between the constituents of the system. The end of the Chapter contains a presentation of the dynamical and structural observables used to analyze the trajectories generated during a MD simulation.

Chapter 4 deals with the simulations of the water-trehalose mixtures. Several aspects of these two systems are analyzed, starting from the formation of clusters of trehalose and continuing with dynamical and structural quantities concerning water. The focus of this work is on hydration water, that is water molecules that are at the interface with trehalose molecules. From the study of the translational dynamics of water molecules and the properties of the formed hydrogen bonds, several conclusions are drawn.

In **Chapter 5** simulations of the multicomponent mixture of water-trehalose-DMSO-lysozyme are presented, together with results from the study of the produced trajectories. In this case the focus is on water molecules in the hydration layer of the lysozyme protein. Translational dynamics and properties of hydrogen bonds network are analyzed and conclusions on the role of DMSO in such solutions are present in the final part of this Chapter.

In **Chapter 6** general conclusions on the work done and on results obtained are summarized.

Appendix A contains some comments on the implementation and performance of the program used for the study of the hydrogen bonds network that has been written implementing a routine for the execution on a multi-core machine.

Appendix B contains a list of publications, Schools and Conferences attended where parts of the work contained in this Thesis have been presented.

Chapter 1

Water

This Chapter is devoted to a general introduction to the properties of liquid water and its importance in this work. Section 1.1 and 1.2 present the water molecule, its phase diagram and its peculiar anomalies. Section 1.3 deals with supercooled glassy water. In Section 1.4 the importance of water in the biological context is described.

1.1 The water molecule

A water molecule is made of one oxygen and two hydrogen atoms disposed in a non-linear planar v-shaped molecule. The two hydrogen atoms occupy the external vertices and the oxygen atom occupies the central vertex. The geometry of the molecule can be described using the value of the H–O–H angle and the O–H distance. In the gas phases the H–O–H angle is 104.5° and the O–H distance is 0.957\AA [14, 15]. Each oxygen-hydrogen pair is covalently bonded. The valence electrons of the oxygen atom form two lone pairs that together with the hydrogen atoms form a tetrahedral structure. A schematic representation of the water molecule is shown in Figure 1.1

Water is a polar molecule. Due to the O-H covalence bonds, hydrogen atoms are attracted towards the oxygen thus leaving the proton of the hydrogen atoms partially unscreened. The total electronic molecular distribution is strongly condensed towards the oxygen atom [16] and because of its non-linear shape, water molecule presents a permanent molecular dipole moment of 1.85 D [17]. The disposition of charges in a water molecule makes possible to form Hydrogen Bonds (HBs) between hydrogen and oxygen atoms of different molecules.

An Hydrogen Bond is a strongly directional attractive force along the O–H \cdots O axis (the lone pair - hydrogen direction). The energy associated with an

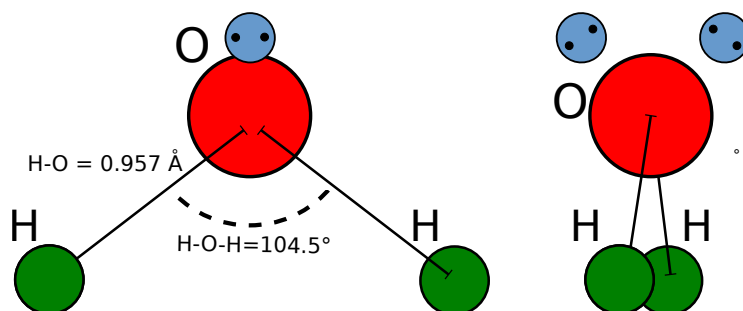


Figure 1.1: *Schematic picture of water molecule. The position of the lone pairs of oxygen electrons are evident in the picture on the right. Lone pairs and the two hydrogen atoms arrange together into a tetrahedral structure.*

HB is circa 20 kJ/mol, higher than the typical intra-molecular interaction, as for example the dipole-dipole van der Waals of circa 1 kJ/mol. Due to its structure, each water molecule is capable to form four HBs with other molecules, two as a donor and two as an acceptor. Bonding to each other, water molecules form a network of hydrogen bonds, arranging themselves in a tetrahedral structure (see Fig. 1.2). The formation of hydrogen bonds decreases the ionic character of the covalent O–H bond and, as a consequence, the structure of a water molecule in the liquid phase results relaxed with respect to the one of an isolated molecule.

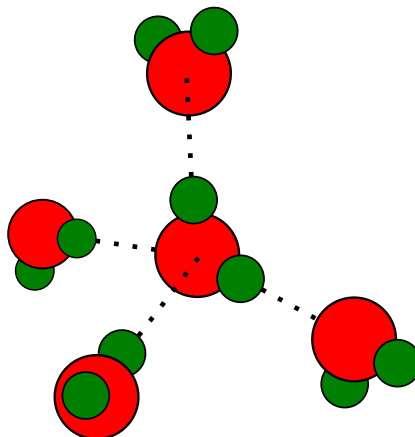


Figure 1.2: *Picture of the tetrahedral hydrogen bond network that water locally forms.*

The ability to form an extended HB-network and to behave cooperatively

characterize the structure and the dynamics of water in both the liquid and the crystalline phases and plays a crucial role in determining the peculiar properties of water.

Fig. 1.3 shows the phase diagram for the stable phases of water. At ambient condition ($T \approx 298,15$ K and $P = 1$ bar) the stable phase of water is the liquid one.

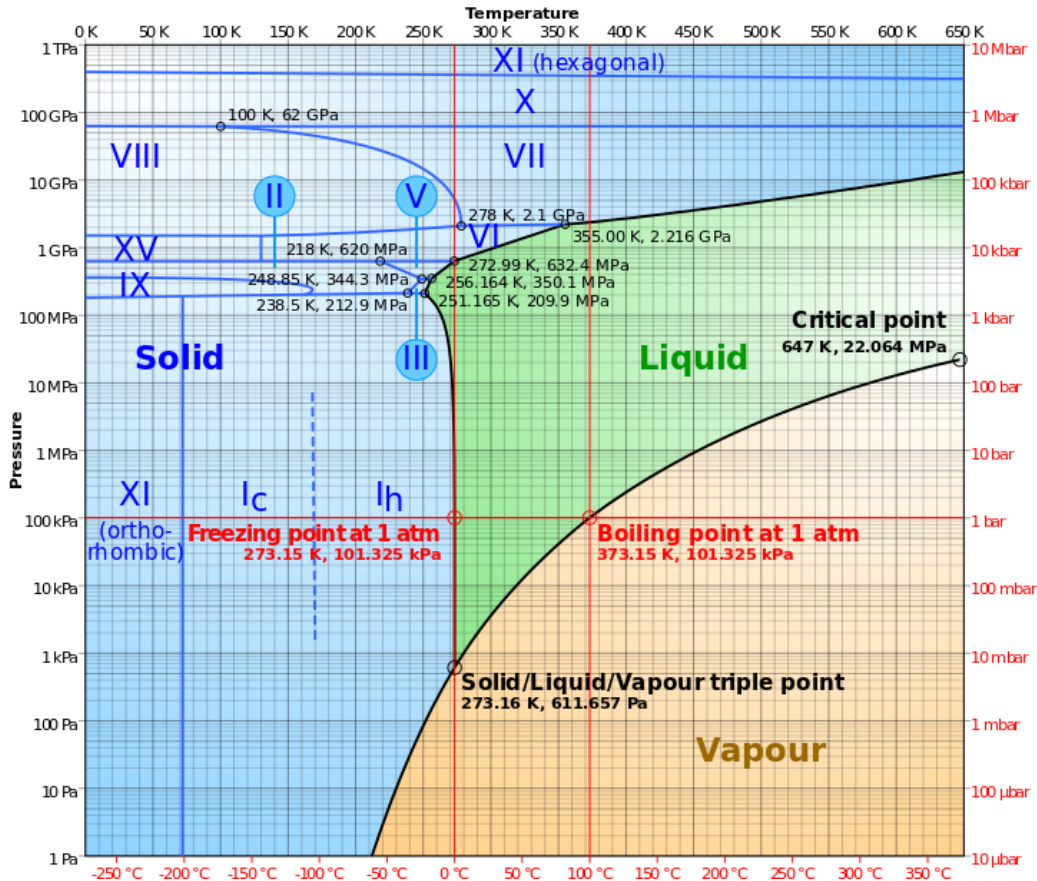


Figure 1.3: Phase diagram of the stable phases of water in the $P - T$ plane. Figure from Ref. [18].

For temperatures below 273 K at ambient pressure the HBs network becomes more stable and the water freeze in the ice phase known as I_h (*hexagonal ice*). Ice I_h is one of the stable phase of solid water and is the most common form of ice on Earth. When the temperature is raised above 373 K the HBs broke and the water becomes steam. Steam is the only stable phase of water above this temperature. Because of the polymorphism of crystalline water, the hexagonal ice I_h its not the only solid phase of water. There are

indeed sixteen different crystalline phases, each of them stable in a certain region of the P - T plane. Consequently there are also several triple points besides the most known one, the solid-liquid-vapor triple point.

The peculiarities of water extend over all the phase diagram, not being limited to the solid phase. As an example, from the liquid-vapor critical point emanates the so called Widom line, a line that divides a region with a more liquid-like vapor from a region with a more gas-like form of steam.

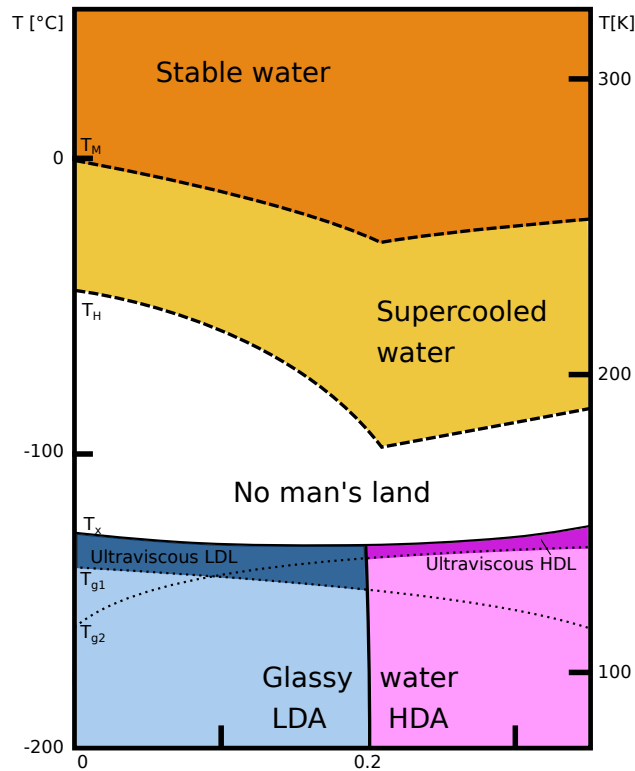


Figure 1.4: Schematic representation of the non-crystalline forms of water in the P - T plane. Figure adapted from Ref. [1]

Including also the *metastable states* of water the phase diagram appears even more complex (see Fig. 1.4). Confined in the low temperature region of the phase diagram, water presents three forms of solid amorphous ice: High Density Amorphous (HDA) ice and Low Density Amorphous (LDA) ice are two glassy states separated by a first order phase transition. The third glassy state of water is the Very High Density Amorphous (VHDA) ice [19]. Cooled very rapidly below the melting temperature $T_M(p)$, water enters in the metastable liquid phase called *supercooled water*. If cooled further down

the homogeneous nucleation temperature $T_H(p)$, supercooled liquid water rapidly turns into ice by spontaneous thermal fluctuations. Heating glassy water above the glass transition temperature $T_g(p)$, water enters in the ultraviscous liquid metastable phase. This region is bounded from above by the spontaneous crystallization temperature $T_x(p)$, above which ultraviscous liquid becomes ice. In between $T_H(p)$ and $T_x(p)$ lays the *no man's land*, a region in which the fast ice nucleation prevents any experimental attempts to keep water in a liquid form. It is important to stress that the presence of metastable liquid water in this region is not forbidden by thermodynamic constraints. The fast crystallization rate and the consequent decrease of the lifetime of the metastable liquid state make impossible the observation of liquid water with available experimental techniques.

Molecular Dynamics (MD) simulations, using very fast cooling rates, can enter the *no man's land*.

1.2 Anomalous properties of water

Water is the most common liquid on Earth and is also the most anomalous one as it exhibits more than 60 thermodynamic and dynamical anomalies [3, 20–22]. Those anomalies are encountered in all the phase diagram and are due to the peculiar ability of water to form an hydrogen bonds network.

Fig. 1.5 reports a schematic representation of four thermodynamic anomalies of water compared to simple liquids. Each panel shows the temperature dependence at ambient pressure of different physical quantities: the density ρ , the isothermal compressibility κ_T , the coefficient of thermal expansion α_P and the isobaric specific heat c_P respectively. It is evident how the deviation from the behaviour of a simple liquid increases with decreasing temperatures [1–3, 23]. Top left panel of Fig. 1.5 shows probably the most known among water anomalies, the density anomaly. A simple liquid is expected to contract upon lowering the temperature, thus monotonically increasing its density. On the contrary water density ρ shows a maximum for $T = 277$ K at ambient pressure. This maximum moves towards lowers temperatures upon increasing pressure. The positions of these maxima as a function of the temperature results in a line called Temperature of Maximum Density (**TMD**).

Fig. 1.6 reports the experimental **TMD** for D_2O . Related to the presence of the **TMD** is the behaviour of the thermal expansion coefficient α_P . The latter is defined as

$$\alpha_P = \frac{1}{V} \left(\frac{\partial V}{\partial T} \right)_P = -\frac{1}{\rho} \left(\frac{\partial \rho}{\partial T} \right)_P \quad (1.1)$$

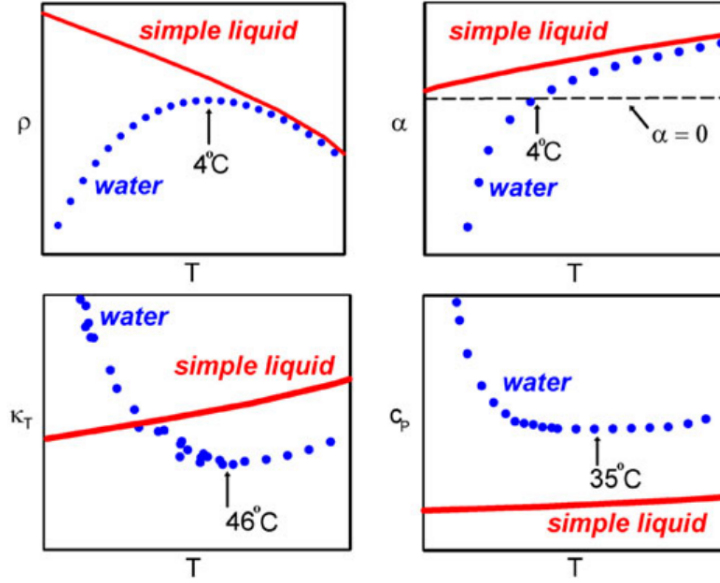


Figure 1.5: Temperature trends of density ρ (top left), thermal expansion coefficient α_P (top right), isothermal compressibility κ_T (bottom left) and isobaric heat capacity c_P (bottom right). For comparison red lines report the expected behaviour for a simple liquid. Figure from Ref [1].

and, as a consequence of the maximum in the density, α_P vanishes and then changes sign, becoming negative at low temperature. Moreover, provided the negative slope of the **TMD**, the values of temperatures at which α_P changes sign decreases upon compression of the system. Also the isothermal compressibility κ_T and the isobaric heat capacity c_P behave anomalously. In a simple liquid these two response functions decrease monotonically upon lowering the temperature, whereas in water they show a minimum at $T = 319$ K and $T = 308$ K respectively. Below these temperatures they show a rapid increase, abruptly departing from the behaviour of a simple liquid. The abrupt increase of the three response function (α_P , κ_T , c_P), suggests the presence of an apparent divergence of these quantities upon further cooling. These steep increase can be described by a power law [23, 25] of the form

$$X \sim \left(\frac{T}{T_S} - 1 \right)^{\lambda_X} \quad (1.2)$$

where X is the generic response function, λ_X the associated exponent and T_S the singular temperature. At ambient pressure the estimated singular temperature is the same for all the response functions, $T_S = 228$ K. This value of

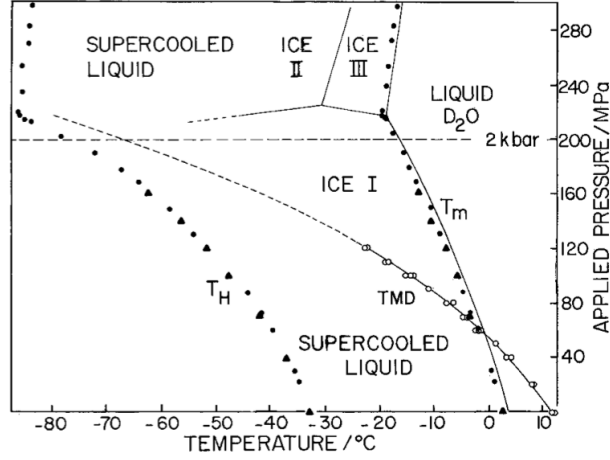


Figure 1.6: Temperature of Maximum Density for D_2O in the P - T plane. Circles are from experiments, dashed line is a low temperature extrapolation. Figure from Ref [24].

T_S is below the homogeneous nucleation temperature T_H , thus laying in the *no man's land*. Being these divergences in a region of phase space difficult to probe, they are named *apparent divergences*.

It is interesting to relate the divergences of the response functions to thermodynamic fluctuations in the liquid. The three response functions just seen are defined as

$$\kappa_T = -\frac{1}{V} \left(\frac{\partial V}{\partial P} \right)_T, \quad (1.3)$$

$$c_P = \frac{T}{N} \left(\frac{\partial S}{\partial T} \right)_P, \quad (1.4)$$

$$\alpha_P = \frac{1}{V} \left(\frac{\partial V}{\partial T} \right)_P, \quad (1.5)$$

and are connected to the fluctuations of volume and entropy by the equations:

$$\langle (\delta V)^2 \rangle = V k_B T \kappa_T, \quad (1.6)$$

$$\langle (\delta S)^2 \rangle = N k_B C_P, \quad (1.7)$$

$$\langle \delta S \delta V \rangle = V k_B T \alpha_P. \quad (1.8)$$

Isothermal compressibility and isobaric heat capacity coefficients are connected to the fluctuations of volume and entropy, respectively. The anomalous increase of these two response functions corresponds to an increase of the self correlations of the liquid upon lowering the temperature, at odd with what happens in simple liquids, where lower temperatures correspond to smaller fluctuations. In addition, the apparent divergence of the thermal expansion coefficient is a signature of the cross-correlation between volume and entropy. The change in the sign of α_P from positive to negative signals a loss of entropy by increasing the volume, contrary to what is common in simple liquids. The fact that entropy and volume anti-correlate is a consequence of the formation of hydrogen bonds, for which a decrease in orientational entropy is accompanied by an increase in volume.

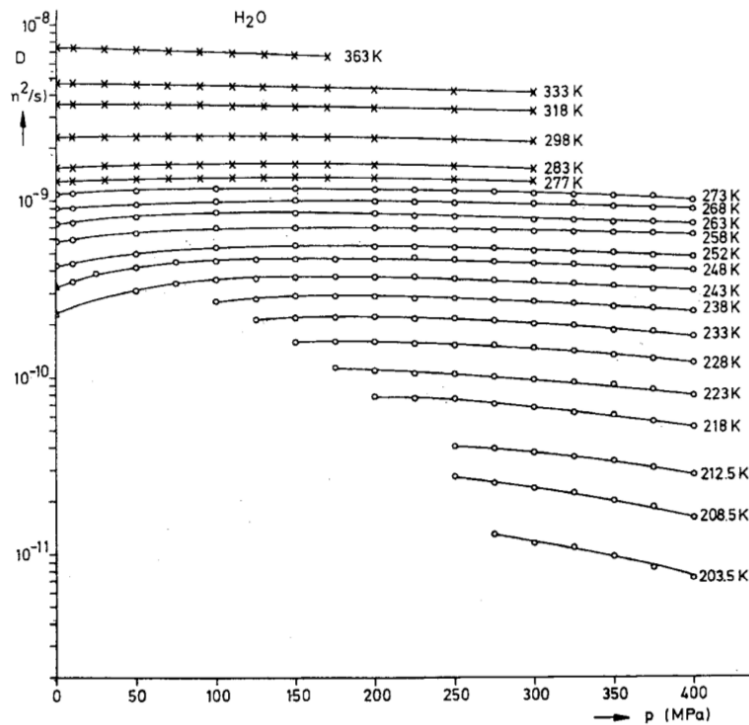


Figure 1.7: Experimental self-diffusion coefficient D of water as a function of the pressure at constant temperature. Figure from Ref [3].

Water is an anomalous liquid also with respect to dynamics. One example is given by the diffusion anomaly. The diffusion coefficient D is defined through the mean square displacement (MSD), that in three dimension is

$$D = \lim_{t \rightarrow \infty} \frac{\langle |r_j(t+t) - r_j(t)|^2 \rangle}{6t} \quad (1.9)$$

and related to the viscosity η of the liquid through the mobility coefficient μ in the Stokes-Einstein relation

$$D = \mu k_B T.$$

Since in simple liquids the compression is usually correlated to a loss of fluidity, the coefficient D should decrease upon increasing pressure. As shown in Fig. 1.7, the self-diffusion coefficient of water at $T \sim 283$ K increases upon compression of the system until it reaches a maximum ($P \approx 150$ MPa at that temperature). As seen for thermodynamic quantities, also the anomaly in the self-diffusion coefficient is related to the presence of an HB network: when the pressure increases an increasing number of hydrogen bonds between water molecules break, implying an overall greater mobility of particles within the liquid.

All the water anomalies shown in this section seems to continue and become more pronounced in the supercooled region of the phase diagram of water.

1.3 Supercooled and glassy water

Supercooled water is water in its liquid phase even below the melting temperature T_M . This state is a metastable state with a finite lifetime. A stable state occupies the global minimum of the appropriate thermodynamic potential, whereas metastable states are trapped in local minima of the potential for a certain amount of time. Metastable state is an out of equilibrium state being the true stable state the crystalline phase. However a metastable state could be considered stable if its typical lifetime τ_{life} exceeds the observation time of an experiment τ_{obs} . In turn the latter must be greater than the relaxation time, that is the time the system takes to rearrange and equilibrate, τ_{rel} . Thus, for a metastable state must hold the relation

$$\tau_{rel} \ll \tau_{obs} < \tau_{life}.$$

To avoid the crystallization of liquid water before the experiment has been performed, special caution must be taken. Purity of the sample, absence of external mechanical and thermal perturbations and smoothness of the walls of the container are conditions that help to extend the life time of the

supercooled liquid. However, being a metastable state, supercooled water cannot last forever: it can either crystallize in a solid stable phase or turn into a glass. Which of the two depends on the relative values of two times that characterize a supercooled liquid: the nucleation time τ_1 , that is the time a given fraction of volume takes to crystallize, and the relaxation time τ_2 . The nucleation time is a non monotonic function of the temperature, it diverges at T_M and at $T = 0$ K and has a minimum in between (see Fig. 1.8 and Fig. 1.9). Its behavior stems from the competing thermodynamic driving force for nucleation and the increasing viscosity of the liquids, that hampers the fast grow of ice nuclei [21,26]. The relaxation time is small near T_M and increases sharply as the temperature lowers. When the relaxation time τ_2 becomes comparable to the duration of an experiment, the molecules have no longer time to rearrange and the system appears arrested in that time scale.

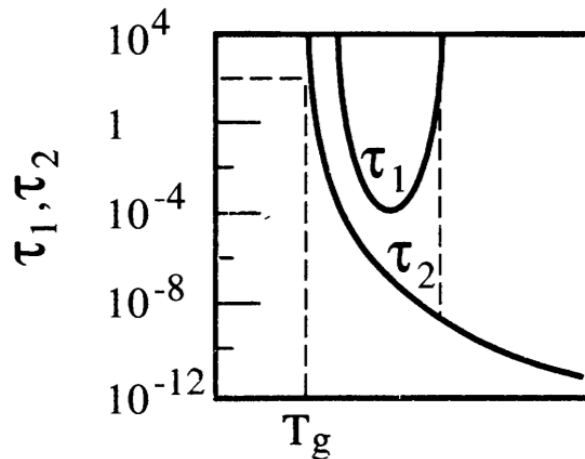


Figure 1.8: Nucleation time τ_1 and relaxation time τ_2 as a function of the temperature. T_G is the glass transition temperature. Figure from Ref. [21].

With an ad hoc cooling schedule one can avoid the crystallization of the sample and at the same time keep the system at equilibrium, thus preventing the formation of an out of equilibrium glassy state. With a too small cooling rate the system crystallize, with a too high one becomes a glass (*quenching*).

The glass transition temperature is defined as temperature at which the viscosity reaches the value $\eta = 10^{13}$ poise. It is interesting to note that, due to the kinetic nature of the glass transition, the glass transition temperature T_g varies, albeit slightly, using different cooling procedures. The location of

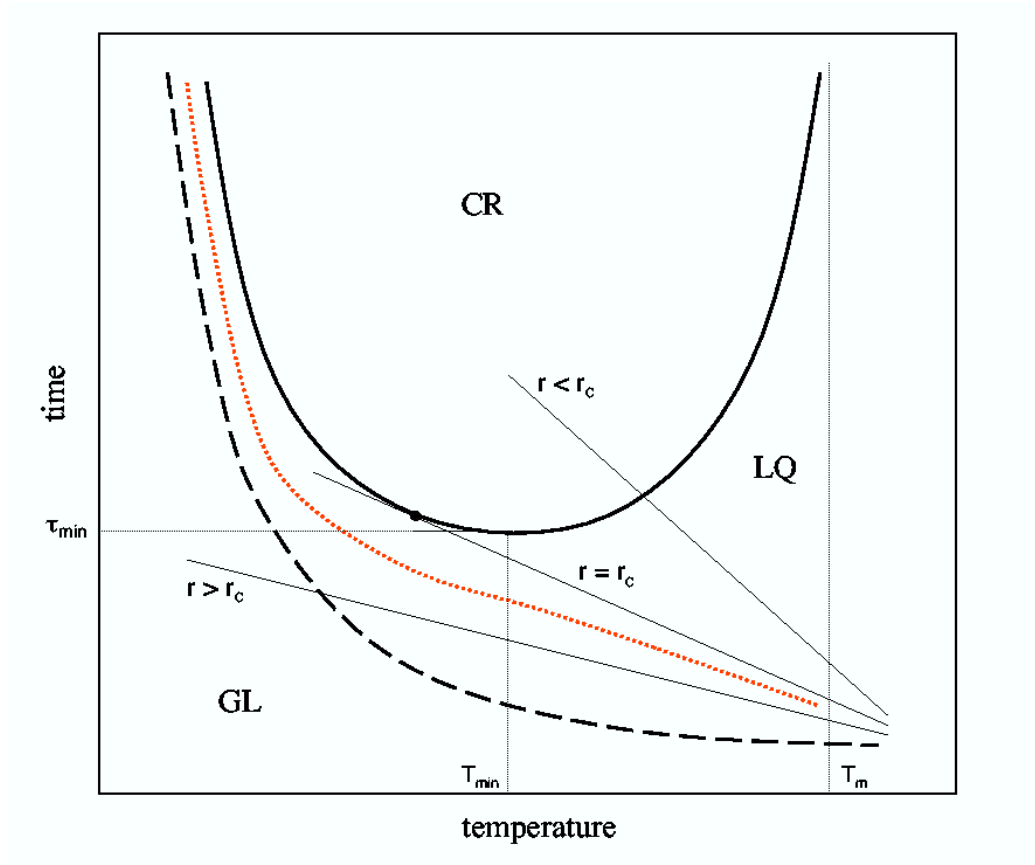


Figure 1.9: Nucleation time (continuous line) and relaxation time (dashed line) as a function of the temperature. Straight lines refers to linear cooling schedules with different cooling rate, dotted red line to a non linear cooling schedule. CR stands for crystal, LQ for liquid, GL for glass. Figure from Ref. [26].

the glass transition of water is still debated: it is usually accepted that water vitrifies at 136 K [27, 28], but recent measures moved T_g around 165 K [29, 30]. As already mentioned water is a polyamorphic liquid, in that it presents three glassy state in the low temperature region. The most common amorphous phases are Low Density Amorphous ice (LDA), for low values of the pressure, and High Density Amorphous ice (HDA), for higher values of the pressure. These two disordered solid phases are separated by a first order phase transition discovered by Mishima and co-workers in 1985 [31] and confirmed later by other experimental works [32, 33].

The presence of two amorphous phases of arrested water and its anomalies in all the phase diagram has led to many theoretical works in the attempt to explain such peculiar behavior [3, 34–36]. Some of the most relevant scenarios proposed are the stability limit conjecture [25], the second critical point scenario [34], the critical point free scenario [4] and the singularity free scenario [35]. The second critical point scenario has been extensively debated and is perhaps the most influential one.

The main idea behind this theory is the presence of a second critical point besides the liquid-vapour one, the Liquid-Liquid Critical Point (LLCP). The LLCPP lays in the no man's land and is the terminal point of a first order phase transition that separate two state of supercooled water: the Low Density Liquid water (LDL) and the High Density Liquid water (HDL). This Liquid-Liquid Phase Transition (LLPT) goes down in the glassy region of the phase diagram, where it separate LDA and HDA ice, that are thus the vitreous counterpart of LDA and HDA respectively. From the Liquid-Liquid Critical Point emanates a line of maxima of the thermodynamic response functions, the Widom line. This hypothesis is able to explain the experimentally observed apparent divergences of response functions, connecting them to the progressive increase of a correlation length as one approach the critical point. The divergence of a thermodynamic response function is supposed to happen only at the critical point, that is in the no man's land and therefore cannot be directly probed by experiment. Nonetheless studying the maxima of response functions in the mild supercooled region by experiment and simulation works, one could track down the position of the LLCPP. The Widom line is indeed the first detectable feature that one encounters upon cooling and that indicates the presence of the LLCPP. Poole and co-workers were the first to hypothesize a LLCPP [34]. In their work on molecular dynamics simulations of ST2 water potential the existence of a LLCPP came out from four points:

- low-temperature isotherms showing inflection point at $\rho \approx 1$ g/cm.

- Observation of two distinct phases below the estimated critical point.
- Observation of the phase transition HDL-LDL.
- Validation of ST2 model of water versus experimental results above the no man's land.

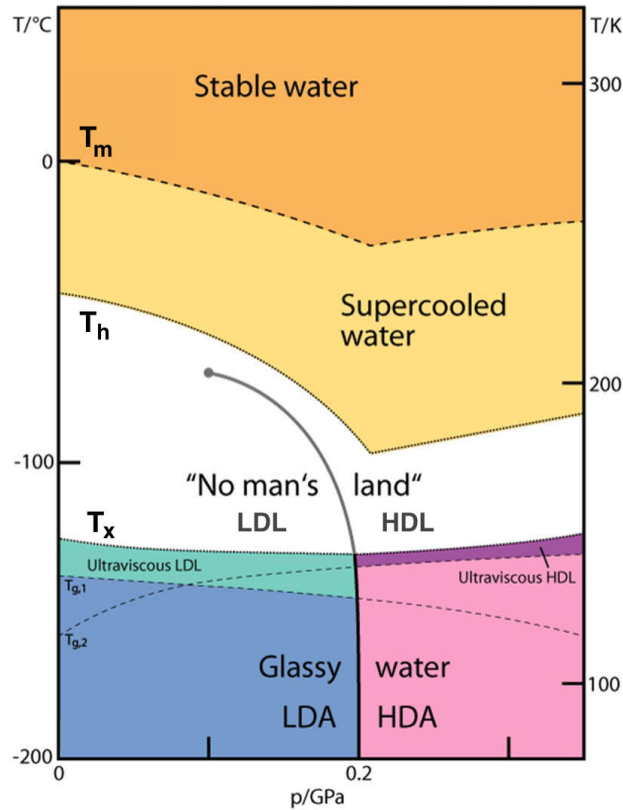


Figure 1.10: Schematic representation of the non-crystalline forms of water in the P - T plane according to the LLCP scenario. The coexistence line that divide LDL and HDL start from the LLCP in the no man's land and goes down in the glassy region of the phase diagram, separating the structurally arrested counterpart of supercooled water, LDA and HDA ice. Figure adapted from Ref. [1].

Fig. 1.10 reports the phase diagram of real water according to the second critical point scenario. Further studies located the LLCP in the supercooled region also for other water model potentials, like for example TIP4P, TIP5P, TIP4P/2005 and SPC/E (See Ref. [1] and references therein). The second critical point scenario was investigated also experimentally. A decisive experiment to corroborate this scenario was carried by Mishima and

Stanley [2]. Studying the melting of different high-pressure crystalline phase of water induced by decompression, they located the LLCPC at $T_C = 220$ K and $P_C = 100$ MPa, which is today considered the estimated position of the liquid-liquid critical point of bulk water. Recently the scenario has been corroborated by the experimental finding of a point in the widom line [37,38]

1.4 Biological solutions

Water plays a fundamental role in biological systems at all level, from a single molecule bonded to a biological macromolecule to the inside of a cell [39]. Of particular interest is the behaviour of aqueous solutions of different disaccharides and disaccharides with proteins. These solutions are very common in nature and their interesting properties may also help to understand the anomalies of supercooled water, e.g. how the disruption of water hydrogen bonds due to the presence of other molecules may affect the dynamics of supercooled water. Moreover aqueous solutions of this kind are relevant in many technological applications, such as cryopreservation of organic molecules. In this context, the influence of disaccharides in a ternary solution together with water and proteins has been extensively investigated both by experiment and by computer simulations [11,12].

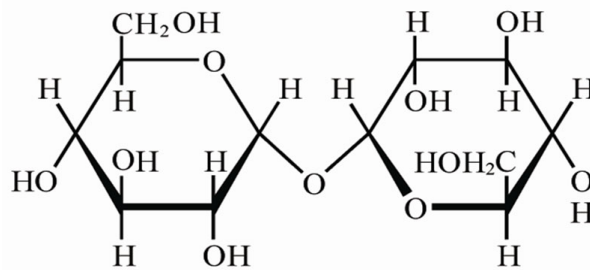


Figure 1.11: *Schematic representation of a trehalose molecule.*

Trehalose as cryoprotectant

Trehalose is a disaccharide formed from two glucose rings linked by a 1-1 α -bond (see Fig. 1.11) and it has been proven to be especially effective, when added to a solutions of water, to alter the properties of water. Through the interaction with water molecules, it is able to destroy the hydrogen-bonds

network formed by water, thus hampering the formation of ice. It has also a strong effect on the dynamics of water molecules, as it is capable to greatly slow down their dynamics upon cooling. Due to these characteristics trehalose is widely used as cryoprotectant.

Historically three main scenarios have been proposed to explain the bioprotection mechanism of carbohydrates. Within the *water replacement scenario* by Crowe *et al.* [40], the source of their bio-preserving power is their ability in establishing strong hydrogen-bond interactions with the polar groups of biomaterials, thus excluding water molecules from the direct interaction with the latter. In the *vitrification scenario* by Green and Angell [41] the mobility of the biomolecule is hindered because of the vitrification of the entire trehalose-water solution upon cooling. According to the *water entrapment scenario* by Belton and Gil [13], trehalose is capable of forming a cage around the protected biostructure that contains slow water molecules.

Some works point to a certain scenario, but in literature several results are compatible with more than one scenario at the same time, basically because all these hypothesis are not mutually exclusive. This last point motivated the work of Fedorov *et al.* [42], that with the attempt to include previous findings proposed the fourth hypothesis for explaining bioprotection, the *broken glass scenario*, in which the mobility of the protein is reduced by the formation of trehalose non-uniform cluster interacting with the protein but leaving the protein hydrated.

An interesting review on the role of trehalose in bioprotection and the last results concerning this research field is Ref. [10] by Cordone *et al.*

The Protein Dynamical Transition

An important example of the biological role of supercooled water is the low-temperature activation of hydrated proteins. In fact all the functions of a protein are inhibited if a minimum critical level of hydration is not secured. Without hydration water proteins can not access nor switch between different conformations and therefore fulfill their roles in biological environment. From the dynamical point of view, this importance is embedded in the dynamical coupling between the protein internal motion and its hydration water. Many studies using a variety of techniques have been carried out on biological macromolecules from the stable liquid phase to the supercooled regime aimed to understand this coupling [43–45].

In addition to being important for protein stability, surface water also has a profound influence on the dynamics of a protein molecule as a whole.

Assessed the role of hydration water in protein functioning and the connec-

tion of this last with protein flexibility, one of the most striking example of the biological role of supercooled hydration water is that the flexibility of a protein, strongly suppressed at very low temperature, suddenly enhances, upon heating, inside the *no-man's land* of the phase diagram of water (see Fig. 1.12).

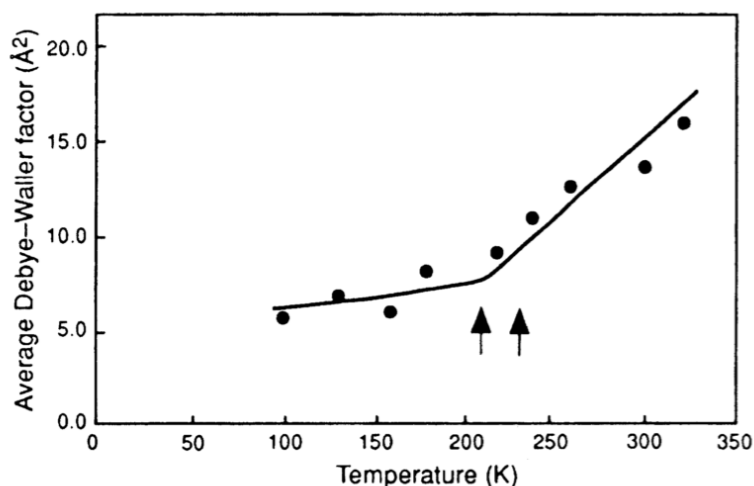


Figure 1.12: *Dependence with temperature of the average Debye-Waller factor calculated in the protein ribonuclease A. Figure from Ref. [46].*

This dynamical feature is called Protein Dynamical Transition (PDT) and it is driven by the hydration water because dry protein samples do not experience this flexibility increase. Changes in the flexibility of a protein can be monitored by looking at the temperature dependences of mean square fluctuations of protein structure, i.e. the atomic mean square displacement of protein atoms, $\langle x^2(t) \rangle$. For large macromolecules like proteins, this can be written as a sum of a vibrational component and a conformational component [47]:

$$\langle x^2(t) \rangle = \langle x^2(t) \rangle_v + \langle x^2(t) \rangle_c.$$

Below the PDT, $\langle x^2(t) \rangle$, is dominated by vibrations, and thus is linear with the temperature. This is also the normal behavior of $\langle x^2(t) \rangle$ for small organic molecules and harmonic solids [46]. If the protein is hydrated, the behavior of $\langle x^2(t) \rangle$ deviates from this linear behavior and the additional conformation contribution is observed. The onset of this last contribution defines the PDT itself. The conformational contribution is due to the activated surface motion

of protein domains and gives the extra mobility to hydrated proteins. Thus above the PDT, the $\langle x^2(t) \rangle$ results to be dominated by anharmonic collective motion of protein atoms [48]. Importantly, in coincidence with the PDT, biochemical activity of many proteins is restored upon increasing temperature. For instance, enzymes have been observed to rapidly bind substrates or inhibitor above the dynamical transition, probably because without collective motions of protein atoms the enzymes are too “frozen” to accommodate them [48]. This transition has been observed in neutron scattering experiments [49, 50], as well as in simulation works [51–54] and terahertz dielectric response experiment [55] not only in proteins, but in a variety of biological macromolecules like RNA, DNA and membranes [53]. For all these different system, PDT occurs between 200 K and 260 K. It is therefore in the super-cooled region that hydration water influences most the internal dynamics of hydrated biosystems.

It is important to note that the position of the Protein Dynamical Transition is influenced by the solvent in which the protein is diluted. Changing the components of a solution shifts the PDT temperature. This means that by choosing the components of a solution one can select the range of temperatures at which the PDT happens [56, 57].

Chapter 2

Dynamics of supercooled water

The anomalous dynamics is probably the most striking and peculiar feature of supercooled and glassy liquids. Indeed the definition of a glassy transition is dynamic [6, 26, 58, 59].

Glassy systems show a slow, two step relaxation with well defined and separated timescales. Correlators stretch over time, extending over several orders of magnitude.

The first part of this Chapter deals with the Mode Coupling Theory, by now the only microscopic theory that is able to describe the glassy dynamics starting from first principles [6]. At the end of this Chapter the issue of the Fragile to Strong Crossover in supercooled liquid is introduced.

2.1 The Mode Coupling Theory

The main idea behind Mode Coupling Theory (MCT) is the mutual interactions between the dynamics of a single particle and the dynamics of its surrounding environment. These two interact in a strongly non linear way and the feedback mechanism involved leads to the observed huge increase of the typical time scale characterizing the system. As an extreme consequence, the system undergoes a glassy transition to an arrested state.

The first formulation of MCT relies on Mori-Zwanzig projection formalism [58, 59]. A series of calculations (here only shortly sketched) results in an exact equation of motion for the evolution of a generic correlator involving the density ρ . After some approximations, a solution is derived and discussed [6, 60, 61].

Let us consider a function $A(t)$ of the positions \mathbf{r}_i and momenta \mathbf{p}_i of N

particles composing a system, its equation of motion is

$$\frac{d\mathcal{L}}{dt} = \{\mathbf{A}(t), \mathcal{H}\} \equiv i\mathcal{L}\mathbf{A}(t) \quad (2.1)$$

where \mathcal{L} and \mathcal{H} are the Lagrangian and Hamiltonian of the system. Introducing the projection operator \mathcal{P} defined as

$$\mathcal{P} \equiv (\mathbf{A}, \dots) (\mathbf{A}, \mathbf{A})^{-1} \mathbf{A},$$

with $(\mathbf{A}, \mathbf{B}) \equiv \langle \mathbf{B}\mathbf{A}^* \rangle$ the equilibrium correlation function, as an operator that project a generic quantity in the \mathbf{A} space, it is possible to extract the \mathbf{A} component from a variable. If, for example, \mathbf{A} is a slow varying with time variable, using the projector operator \mathcal{P} on \mathbf{B} , only the slow component of \mathbf{B} is retained.

With this formalism, the equation of motion 2.1 can be rewritten as

$$\frac{d\mathbf{A}(t)}{dt} = i\boldsymbol{\Omega} \cdot \mathbf{A}(t) - \int_0^t \mathbf{K}(\tau) \cdot \mathbf{A}(t - \tau) d\tau + \mathbf{f}(t) \quad (2.2)$$

with

$$\mathbf{f}(t) \equiv e^{i(1-\mathcal{P})\mathcal{L}t} i(1-\mathcal{P})\mathcal{L}\mathbf{A} \quad (2.3)$$

the *fluctuating random force*,

$$\mathbf{K} \equiv (\mathbf{f}, \mathbf{f}(t)) \cdot (\mathbf{A}, \mathbf{A})^{-1} \quad (2.4)$$

the *memory function matrix* and

$$i\boldsymbol{\Omega} \equiv (\mathbf{A}, i\mathcal{L}\mathbf{A}) \cdot (\mathbf{A}, \mathbf{A})^{-1} \quad (2.5)$$

the *characteristic frequency matrix*.

\mathbf{A} and \mathbf{f} denote the initial values of $\mathbf{A}(t)$ and $\mathbf{f}(t)$, $\mathbf{A} = \mathbf{A}(0)$ and $\mathbf{f} = \mathbf{f}(0)$.

Eq. (2.2) is the generalized Langevin equation and is an exact equation for the time evolution of $\mathbf{A}(t)$. It is composed by two parts: a slow one and a fast one. The *fluctuating random force* $\mathbf{f}(t)$ is the time evolution of the fast component of $\dot{\mathbf{A}}$ in the fast subspace orthogonal to \mathbf{A} , thus embodying the fast contribution to the evolution of \mathbf{A} . The *memory function* \mathbf{K} , given by the autocorrelation of the fluctuating random force, and the *frequency matrix*, that accounts for the part of $\dot{\mathbf{A}}$ that remains in the slow subspace, compose the slow varying part.

Defining the correlation matrix

$$\mathbf{C}(t) \equiv \langle \mathbf{A}(t)\mathbf{A}^* \rangle = (\mathbf{A}, \mathbf{A}(t)) \quad (2.6)$$

and using the generalized Langevin equation, Eq. (2.2), the equation of motion for the correlation matrix is

$$\frac{d\mathbf{C}(t)}{dt} = i\boldsymbol{\Omega} \cdot \mathbf{C}(t) - \int_0^t \mathbf{K}(\tau) \cdot \mathbf{C}(t - \tau) d\tau. \quad (2.7)$$

The last term, involving the fluctuating force, vanished because of the orthogonality with \mathbf{A} , $(\mathbf{A}, \mathbf{f}(t)) = 0$. The main problem in solving this equation lies in the determination of the memory function. \mathbf{K} is a non local in time, non Markovian term that takes into account the previous history of the particle trajectory.

Eq. (2.7) is an exact equation for a generic correlation function. If the variable \mathbf{A} is chosen to be

$$\mathbf{A} = \begin{bmatrix} \delta\rho_{\mathbf{q}} \\ j_{\mathbf{q}}^L \end{bmatrix} \quad (2.8)$$

where $\delta\rho_{\mathbf{q}}$ is the Fourier Transform of the density, save for a constant proportional to the uniform density $\rho = N/V$:

$$\delta\rho_{\mathbf{q}} = \sum_i^N e^{i\mathbf{q}\cdot\mathbf{r}_i} - (2\pi)^3 \rho \delta(\mathbf{q}) \quad (2.9)$$

and $j_{\mathbf{q}}^L$ the longitudinal component of the associated current:

$$j_{\mathbf{q}}^L = \frac{1}{m} \sum_i^N (\mathbf{q} \cdot \mathbf{p}_i) e^{i\mathbf{q}\cdot\mathbf{r}_i} \quad (2.10)$$

with m the particle mass, then the correlation matrix becomes

$$\mathbf{C}(t) = \begin{bmatrix} \langle \delta\rho_{-\mathbf{q}} \delta\rho_{\mathbf{q}}(t) \rangle & \langle \delta\rho_{-\mathbf{q}} j_{\mathbf{q}}^L(t) \rangle \\ \langle j_{-\mathbf{q}}^L \delta\rho_{\mathbf{q}}(t) \rangle & \langle j_{-\mathbf{q}}^L j_{\mathbf{q}}^L(t) \rangle \end{bmatrix} \quad (2.11)$$

and

$$i\boldsymbol{\Omega} = \begin{bmatrix} 0 & i q \\ i \frac{q k_B T}{m S(q)} & 0 \end{bmatrix} \quad (2.12)$$

$$\mathbf{K}(\mathbf{q}, t) = \begin{bmatrix} 0 & 0 \\ 0 & \frac{m \langle R_{-\mathbf{q}} R_{\mathbf{q}}(t) \rangle}{N k_B T} \end{bmatrix} \quad (2.13)$$

with

$$R_{\mathbf{q}} = \frac{d j_{\mathbf{q}}^L}{dt} - i \frac{q k_B T}{m S(q)} \delta\rho_{\mathbf{q}} \quad (2.14)$$

where $S(q)$ is the static structure factor.

Lower left components of the matrices in the terms of Eq. (2.7) give the equation of motion for the evolution of the Intermediate Scattering Function which is the density-density correlation function in the \mathbf{q}, t space and will be introduced in more details in Section 3.8

$$F(\mathbf{q}, t) = \frac{1}{N} \langle \delta\rho_{\mathbf{q}}(t) \delta\rho_{-\mathbf{q}} \rangle. \quad (2.15)$$

It reads

$$\frac{d^2 F(\mathbf{q}, t)}{dt^2} + \frac{q^2 k_B T}{m S(q)} F(\mathbf{q}, t) + \int_0^t \mathbf{K}(\mathbf{q}, t - \tau) \frac{d}{dt} F(\mathbf{q}, t - \tau) d\tau = 0 \quad (2.16)$$

where $S(q) = F(q, 0)$ is the Static Structure Factor. Eq. (2.16) has the form of an harmonic oscillator with frequency $\Omega^2 = q^2 k_B T / m S(q)$ dumped by a time-retarded frictional force proportional to the memory function $\mathbf{K}(\mathbf{q}, t - \tau)$. It can be showed that inside the memory function there are products of density function $\rho_{\mathbf{q}}$ [60].

It should be noted that there is no a priori recipe for deciding which quantities are relevant to describe the behaviour of a system. Appropriate choice should be made based on the knowledge of the system under investigation and on physical intuition.

Eq. (2.16) is an exact equation of motion but some simplifications have to be made to find an equation that is analytically solvable. The basic version of MCT relies on two approximations [61, 62]:

- Approximate the memory function as a four-point density correlation function. This is done by projecting the random fluctuating force onto a subspace, with a new basis of products of two density modes.
- Factorize four-point correlation functions into two-point correlation functions, in order to have a simple memory function that is non trivially zero.

After some manipulations, the resulting memory function is

$$\mathbf{K}(\mathbf{q}, t) = \frac{\rho^2 k_B T}{2Nm} \sum_{\mathbf{K}} |V_{\mathbf{q}-\mathbf{k}, \mathbf{k}}|^2 F(\mathbf{k}, t) F(\mathbf{q} - \mathbf{k}, t) \quad (2.17)$$

where the vertices $V_{\mathbf{q}-\mathbf{k}, \mathbf{k}}$ are defined as

$$V_{\mathbf{q}-\mathbf{k}, \mathbf{k}} \equiv (\hat{\mathbf{q}} \cdot \mathbf{k}) c(k) + \hat{\mathbf{q}} \cdot (\mathbf{q} - \mathbf{k}) c(|\mathbf{q} - \mathbf{k}|) \quad (2.18)$$

with [63]

$$c(k) = \frac{1}{\rho} \left(1 - \frac{1}{S(k)} \right). \quad (2.19)$$

The resulting equation, Eq. (2.17), represents the long time contribution to the total memory function, the one that is most important in the deep supercooled region. Another, short time, part accounts for the instantaneous collisions between particles

$$\mathbf{K}^{(0)}(\mathbf{q}, t) = \gamma_{\mathbf{q}} \delta(t). \quad (2.20)$$

Putting together these two pieces the memory function becomes

$$\mathbf{K}(\mathbf{q}, t) = \gamma_{\mathbf{q}} \delta(t) + \Omega_{\mathbf{q}}^2 \mathbf{K}^L(\mathbf{q}, t), \quad (2.21)$$

where the last term is given by Eq. (2.17).

The final, non linear, equation of motion for the correlator $F(\mathbf{q}, t)$ is

$$\frac{d^2 F(\mathbf{q}, t)}{dt^2} + \Omega_{\mathbf{q}}^2 F(\mathbf{q}, t) + \gamma_{\mathbf{q}} \frac{d}{dt} F(\mathbf{q}, t) + \Omega_{\mathbf{q}}^2 \int_0^t \mathbf{K}^L(\mathbf{q}, t-\tau) \frac{d}{dt} F(\mathbf{q}, t-\tau) d\tau = 0. \quad (2.22)$$

The Mode Coupling Equations, Eq. (2.17) and Eq. (2.22), are a set of coupled closed equations from which the evolution of the correlator $F(\mathbf{q}, t)$ can be calculated.

Before discussing the features of the solution of MCT equations, some remarks are in order:

1. MCT predictions apply also on all the correlators with a non zero overlap with the density ρ .
2. MCT equations take as only input the Static Structure Factor $S(\mathbf{q})$. The main contribution to the slow dynamics comes from the non linear feedback embedded in the memory function. Small changes in static quantities such as the Static Structure Factor produce a huge change in the dynamics of the system.
3. The temperature enters in the MCT equations through the Static Structure Factor $S(\mathbf{q})$.

To discuss the implications of MCT, a further approximation can be done. Due to the fact that the main contribution to the vertices, Eq. (2.18), comes from the first peak of the Static Structure Factor at $\mathbf{q} \sim \mathbf{q}_{max}$ [64], the

substitution of the sum on the wavevectors space with the single value \mathbf{q}_{max} leads to the *schematic* MCT

$$\frac{d^2 F(t)}{dt^2} + \Omega^2 F(t) + \gamma \frac{d}{dt} F(t) + \Omega^2 \lambda \int_0^t F^2(t - \tau) \frac{d}{dt} F(t - \tau) d\tau = 0 \quad (2.23)$$

where λ is the *exponent parameter* and $F(t) = F(\mathbf{q}_{max}, t)$. λ and Ω play the role of the density ρ and the temperature T in the *real*, full MCT. Schematic MCT is particularly useful because, despite its relative simplicity, retains all the important features of the full MCT.

For particular values of Ω and λ , schematic MCT predicts a transition

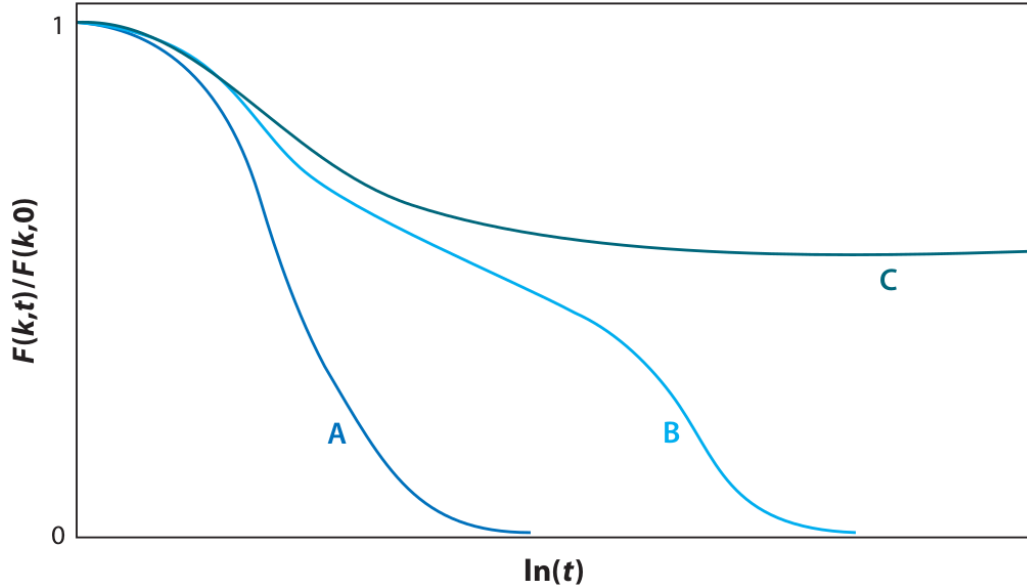


Figure 2.1: *Schematic representation of the evolution in time of a correlator as predicted by Mode Coupling Theory. Curve A represents the decay of the correlator for an hot liquid, curve B refers to a mild supercooled liquid, curve C depicts the decay of the correlator in a non-ergodic phase. Figure from Ref. [65].*

to a non-ergodic phase in which the system is no longer able to relax. A simple sketch of the time evolution of the correlator as a function of time and for different values of the exponent parameter is depicted in Fig. 2.1. For values of the *exponent parameter* smaller than a critical value, $\lambda < \lambda_C$, the correlators decay to zero (curves A and B in the figure). As the value of λ approaches the critical value, the dynamics is slowed down, the correlator stretches in time and the two steps relaxation peculiar of glassy dynamics is enhanced. The first decay to a plateau value is called β -relaxation, the

second, long time, decay to zero is known as α -relaxation. Finally, for $\lambda \geq \lambda_C$, the correlator no longer relaxes to zero (curve C in the figure). Ergodicity is lost and the system undergoes a transition to a dynamically arrested phase. The plateau value

$$\lim_{t \rightarrow \infty} F(t) = f$$

is called *non-ergodicity parameter*.

Mode Coupling Theory is also able to describe in a quantitative way the decay of the correlator (see Fig. 2.2). The part in which the correlator approaches the plateau value $f_{\mathbf{q}}$ (the \mathbf{q} dependence is restored in the full MCT) is called β -relaxation regime. MCT predicts that the time scale of this β -regime, t_ϵ , behaves as

$$t_\epsilon = t_0 |\epsilon|^{\frac{1}{2a}} \quad (2.24)$$

where t_0 is a microscopic time and

$$\epsilon = \frac{T - T_{MCT}}{T_{MCT}} \quad (2.25)$$

is the *distance parameter*. T_{MCT} is the MCT temperature, the value of the temperature at which the system is no longer able to relax.

In the first part of the β -regime, $F(\mathbf{q}, t)$ has the power law behaviour

$$F(\mathbf{q}, t) - f_{\mathbf{q}} \propto t^{-a}. \quad (2.26)$$

When the correlator departs from the plateau region, it has the power law behaviour

$$f_{\mathbf{q}} - F(\mathbf{q}, t) \propto t^b. \quad (2.27)$$

The second relaxation of the correlator, starting from the plateau region down to zero, can be modeled with a Kohlrausch-Williams-Watts function (a stretched exponential)

$$e^{-(t/\tau_\alpha)^\beta} \quad (2.28)$$

with β the stretching parameter and τ_α the characteristic time of the α -relaxation. MCT predicts that τ_α scales as

$$\tau_\alpha = t_0 |\epsilon|^{-\gamma} \quad (2.29)$$

and diverges at T_{MCT} .

a , b and γ are parameters of the theory and are related by

$$\frac{\Gamma^2(1+b)}{\Gamma(1+2b)} = \frac{\Gamma^2(1-a)}{\Gamma(1-2a)} \quad (2.30)$$

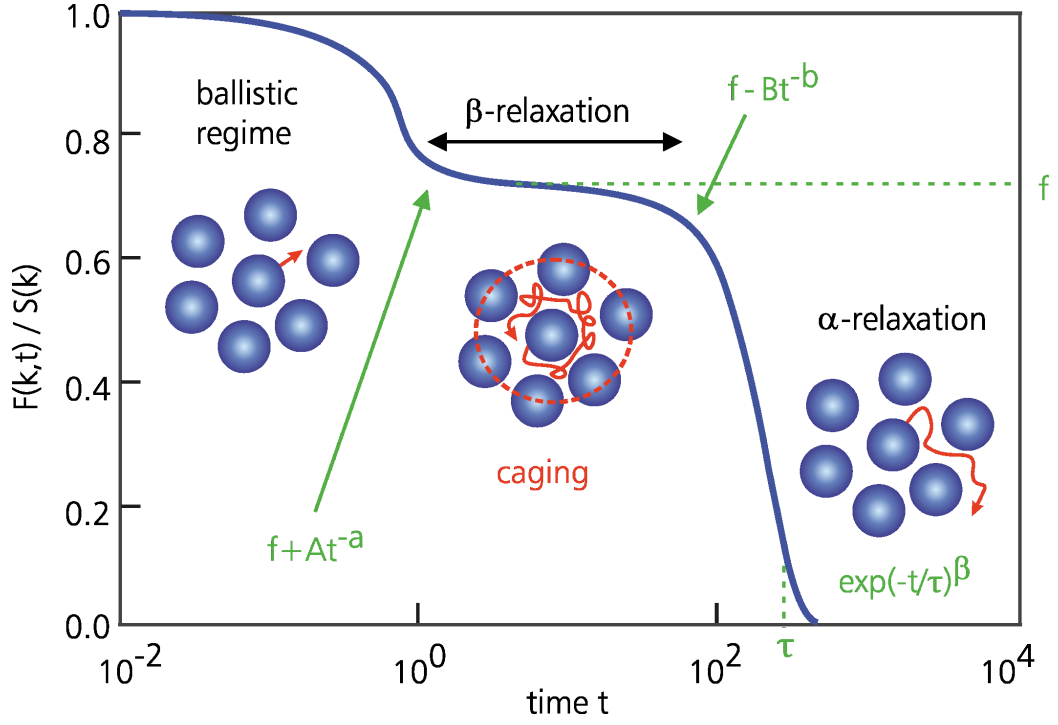


Figure 2.2: Representation of the two steps relaxation of a supercooled liquid along with the functional form of the different stages as predicted by MCT. Figure from Ref. [61].

where Γ is the gamma function, and

$$\gamma = \frac{1}{2a} + \frac{1}{2b}. \quad (2.31)$$

Moreover a and b are bounded in the range $0 < a < 0.5$ and $0 < b < 1$.

MCT also predicts that the correlators rescaled by temperature dependent time scale $\tau_\alpha(T)$ collapse into a master curve Φ in the α -relaxation part of the decay

$$\Phi(t) = F(t/\tau_\alpha). \quad (2.32)$$

This feature is called the Time-Temperature Superposition Principle and from the master curve the exponent b can be extracted.

Central to the physical understanding of the peculiar glassy dynamics of supercooled liquids is the *cage effect*. For short time the particle moves ballistically near its initial position, without significant interactions with other particles. As the time goes by and the tagged particle moves around and explores more space, it finds itself trapped in a cage formed by the surrounding nearest neighbours particles. Due to this confinement it spends a certain

amount of time rattling in the cage. Finally for longer time, the cage relaxes, the particle moves out of it and it is able to recover the usual, long time diffusive regime. This implies a collective rearrangement of a large number of particles. As the temperature is lowered the dynamics is slowed down, the system takes more time to relax and the particle remains trapped in the cage for an increasing amount of time. All these stages can be tracked in the decay of the correlation functions. The first decay corresponds to the ballistic motion, the plateau region is the fingerprint of the movements inside the cage and the final α -relaxation signals the break of the cage and the transition to a diffusive regime, as shown in Fig. 2.2 .

MCT is able to account for this microscopic mechanism of vitrification and embeds it in the MCT equations when considering that most of the contribution of the Static Structure Factor to the *memory function* comes from its first peak, at $q_{max} \sim 2.25 \text{ \AA}^{-1}$. This value corresponds to the typical size of a cage. The interactions of a molecule with molecules whose distances are of the order of the first neighbours shell (thus local interactions) are the most important for a global structural arrest.

Mode Coupling Theory has been developed in the framework of simple liquids and has been extensively tested with hard sphere systems [6] and in simple liquids [66,67]. Nonetheless it has been proved to work also very well with an associative complex liquid, water [7, 8, 68]. MCT is in fact able to capture the main features of the dynamics of water in the mild supercooled region.

Fig. (2.3) shows the oxygen-oxygen Self Intermediate Scattering Function for a Molecular Dynamics simulation of SPC/E water model. The correlators clearly show the characteristic two steps relaxation, with a plateau region that lasts longer the lower the temperature is. Superimposed black lines are best fit with the functional form [7, 8]

$$F(q, t) = (1 - f_\alpha)e^{-(t/\tau_{short})^2} + f_\alpha e^{-(t/\tau_\alpha)^{\beta\alpha}}. \quad (2.33)$$

where the Gaussian term with characteristic time τ_{short} accounts for the initial ballistic regime while the stretched exponential describes the structural α -relaxation. As shown in the picture, this functional form, predicted by MCT, describes very well the decay of the correlator.

It is now important to discuss one of the main failures of MCT in its original formulation. MCT predicts a complete structural arrest of the system with a characteristic relaxation time that diverges as a power law (see Eq. (2.29)) for a given critical value of the temperature T_{MCT} , or of another control parameter. When the system undergoes this transition the correlator no longer relaxes to zero, reaching and maintaining the stable value of the plateau.

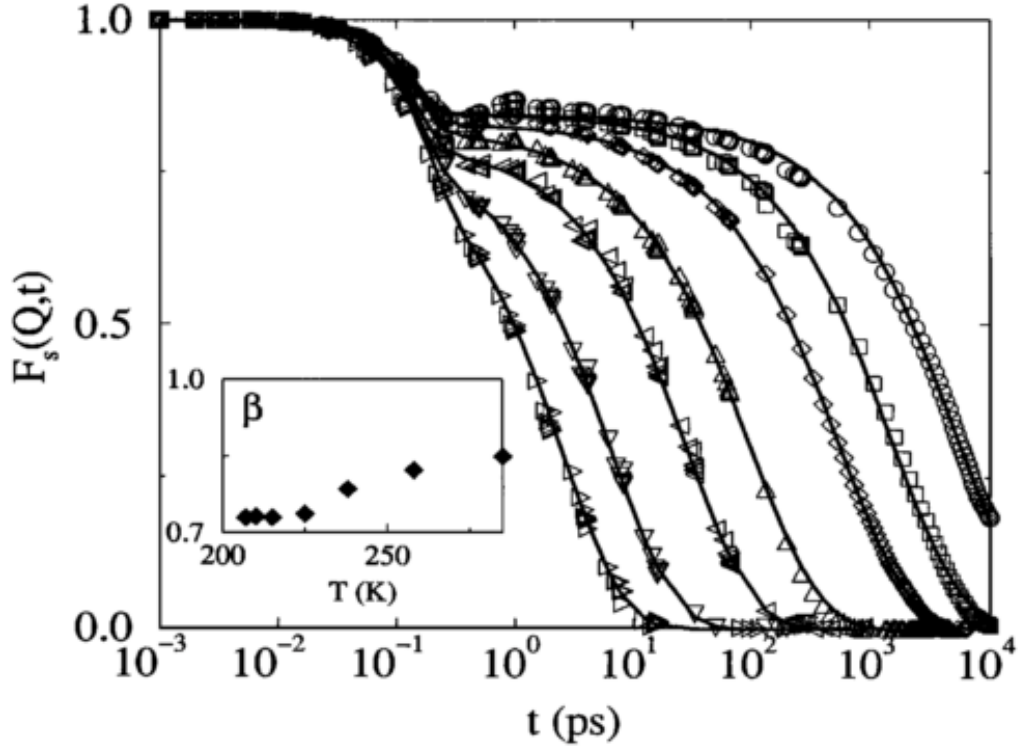


Figure 2.3: Oxygen-oxygen Self Intermediate Scattering Function for different temperatures calculated from MD simulations of SPC/E water. Continuous black lines are best fits to Eq. (2.33). The inset reports the values of the stretching parameter β . Figure from Ref. [7].

It is instead known by experiments and simulations that correlators always relax to zero below T_{MCT} . A microscopic mechanism neglected by MCT restores the ergodicity of the sample and avoids the structural arrest of the system. This additional mechanism is the movement of atoms or molecules by activated process for which they are able to move outside their cages when they are frozen or almost frozen. This process is known as *hopping*. The onset of this new mechanism for the diffusion is connected to the *Fragile to Strong Crossover* observed in water that is discussed in the next Paragraph.

2.2 Fragile and Strong Liquids

Supercooled liquids can be classified in two types according to a method proposed by Angell. Plotting the logarithm of the relaxation time or the

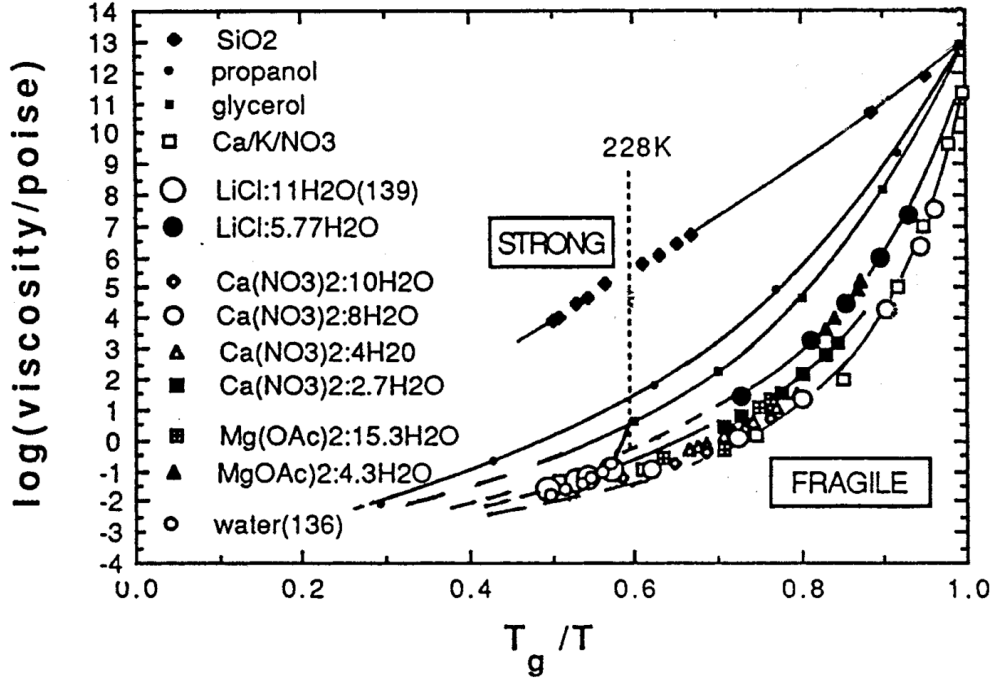


Figure 2.4: Angell plot of viscosity of glass forming liquids. Figure from Ref. [30].

viscosity versus the temperature scaled by the glass transition temperature, liquids behave in two distinctive ways (see Fig. 2.4). A straight line is associated to liquids that show an Arrhenius behaviour, fingerprint of activated processes. Those liquids are named *strong*. Liquids that exhibit deviation from the Arrhenius behaviour are named *fragile*.

Transport in *strong* liquids is governed by thermally activated phenomena (hopping processes). In such liquids the structural relaxation time (or the viscosity) is described by an Arrhenius law

$$\tau_{\alpha} = \tau_0 e^{\frac{E_A}{k_B T}} \quad (2.34)$$

with E_A the activation energy. Relaxation times (or viscosity) of *fragile* liquids follow a Vogel-Fulcher-Tamman law

$$\tau_{\alpha} = \tau_0 e^{\frac{D T_0}{T - T_0}} \quad (2.35)$$

where D , the fragility parameter, and T_0 are constants. T_0 is the *ideal* glass transition temperature. This temperature is in general different from the

experimentally measured real glass transition of a material. Relaxation times of fragile liquids can be described as well with an MCT power law

$$\tau_\alpha = \tau_0 (T - T_{MCT})^{-\gamma}. \quad (2.36)$$

It is interesting to note that the MCT temperature, T_{MCT} , the ideal glass transition temperature, T_0 , and the real glass transition temperature, T_G , are in general non coincident and ordered as [69]

$$T_0 < T_G < T_{MCT} < T_{melting}.$$

Water behaves anomaly also in respect to their fragile/strong classification. It has been shown by MD simulations that water shows a fragile behaviour in the mild supercooled region but it also exhibits a strong behaviour in a region of its phase space [7, 68]. It thus experiences a Fragile to Strong Crossover (FSC) depending on the pressure or density of the isothermal path followed upon cooling.

This deviation is explained by the onset of hopping phenomena before the temperature approaches the T_{MCT} value and that completely drive the diffusive dynamics of the system for lower temperatures [70]. The α -relaxation time switches from a power law typical of MCT to an Arrhenius law characteristic of activated processes.

Simulations of different water models [7, 68, 70, 71] and experiment and simulations in confined water [72, 73] demonstrated that the Fragile to Strong Crossover happens if the path followed upon cooling intersect the LLCW Widom line, as can be seen for example in Fig. 2.5 for the case of TIP4P/2005 [70]. This finding establishes a very important connection between the dynamics and the thermodynamics of supercooled water.

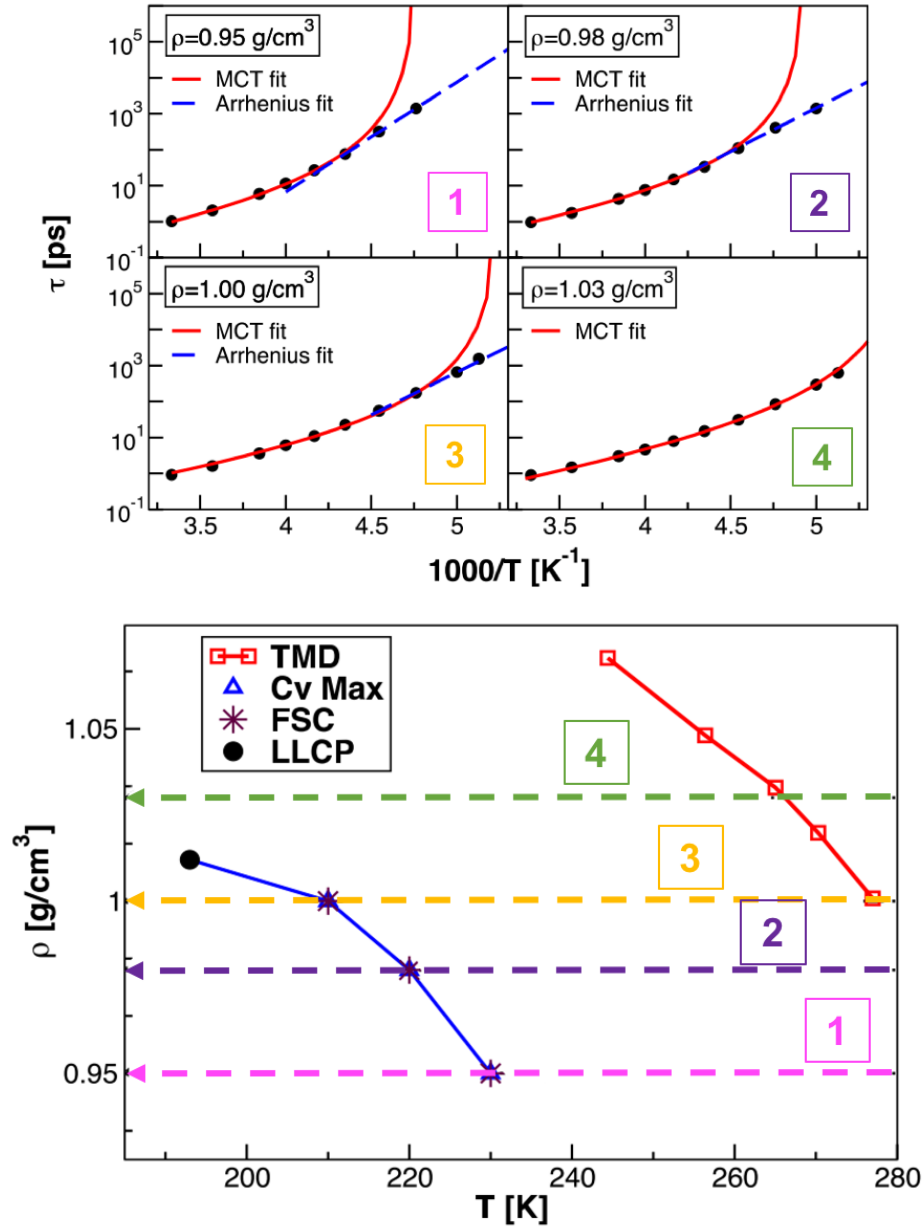


Figure 2.5: Occurrence of FSC in bulk TIP4P/2005 water model. The Widom line is defined through the c_v maxima connected to the LLCP by the blue line. Figures adapted from Ref. [70].

Chapter 3

Molecular Dynamics Simulations

In this Chapter some of the techniques used in the computer simulations of liquids are presented. Algorithms to treat integration of the equations of motions, pressure and temperature. The water model and force field used in this Thesis are presented in Section 3.6 and 3.7. Section 3.8 introduces some of the dynamical and structural quantities used to characterize the properties of a liquid using the trajectories produced by a Molecular Dynamics simulation.

3.1 Classical Molecular Dynamics simulations

Molecular Dynamics (MD) is one of the most diffuse computational techniques used in physics. This technique was developed in the late 1950s within the field of theoretical physics [74, 75]. but nowadays it is applied in a large number of other fields like for example chemical physics, materials science and biophysics. In MD the evolution of a system is obtained by numerical integration of the Newton's law of motion. This technique permits to obtain the trajectories of the particles that compose the system, providing a description of how the positions and velocities of such particles vary with time.

In the physics of liquid state an analytical approach to a problem is often not possible so MD simulations are widely used in this field.

The starting point of a MD simulation is the Hamiltonian \mathcal{H} of a system. For a system which contains a fixed number of particles N the Hamiltonian can be written as:

$$\mathcal{H}(\{\mathbf{r}_i\}_N, \{\mathbf{p}_i\}_N) = \mathcal{K}(\{\mathbf{p}_i\}_N) + \mathcal{U}(\{\mathbf{r}_i\}_N), \quad (3.1)$$

where \mathcal{K} is kinetic energy term and \mathcal{U} is the many-body interaction potential. The potential \mathcal{U} can be assumed to be approximated with the sum of the

radial potentials u_{ij} between pairs of particles.

$$\mathcal{U}(\{\mathbf{r}_i\}_N) = \frac{1}{2} \sum_i \sum_{j \neq i} u_{ij}(|\mathbf{r}_i - \mathbf{r}_j|).$$

As previously stated, the trajectory of the particles are obtained by solving the differential equations embodied in Newton's second law:

$$m_i \ddot{\mathbf{r}}_i = \dot{\mathbf{p}}_i = \mathbf{F}_i = -\nabla_{\mathbf{r}_i} \mathcal{U}, \quad (3.2)$$

$$v_i = \dot{\mathbf{r}}_i = \frac{\mathbf{p}_i}{m_i}. \quad (3.3)$$

A finite difference method is used to integrate these equations with a discretization of the temporal axis in a series of time steps of length δt . Given the positions and the velocities of the particles at time t , the positions and the velocities of the particles at time $t + \delta t$ are computed. Thus positions and velocities of particles are calculated in a deterministic way. Details about integration algorithms are given in Section 3.2.

To perform an MD simulation it is necessary to provide an initial configuration of the particles. Suitable initial space configurations are usually assembled by placing the particle at the vertices of standard lattices. In more complex solute-solvent systems it is often necessary to provide a more realistic conformations of molecules and these configuration are taken from crystallographic data. Stated the relation between temperature and kinetic energy, the velocity configurations are generated by extracting random values taken from a Maxwell-Boltzmann distribution. Along the x -axis for example

$$P(v_{ix}) = \sqrt{\frac{m_i}{2\pi k_B T}} \exp\left[-\frac{m_i v_{ix}^2}{2k_B T}\right], \quad (3.4)$$

which provides the probability that at the temperature T , the particle i of mass m_i has a velocity v_{ix} along the x axis.

The first stage of an equilibrium MD simulation is the equilibration of the system (*equilibration run*). In this first part, starting from the initial configuration, the system is allowed to run for a period of time long enough to fully relax. Special care must be taken to ensure that the system equilibrates properly, monitoring total and potential energies for an appropriate amount of time. Once the energy is minimized, all counters are set to zero and the system is allowed to further evolve. This second stage is commonly named *production run* as trajectories can be used to calculate the equilibrium quantities.

The trajectories produced by MD simulations correspond to a sequence of points in the phase space as a function of time. In order to face off experimental data it is necessary to evaluate from this microscopic quantities macroscopic properties as energy or other thermodynamic functions of the system. To convert from microscopic to macroscopic properties we can use the statistical mechanics.

In statistical mechanics, average values are defined as ensemble averages. The ensemble average of the observable of interest $A = A(\mathbf{r}, \mathbf{p})$ is given by:

$$\langle A \rangle = \int \int A(\{\mathbf{d}\mathbf{r}_i\}_N, \{\mathbf{d}\mathbf{p}_i\}_N) \rho(\{\mathbf{d}\mathbf{r}_i\}_N, \{\mathbf{d}\mathbf{p}_i\}_N) \mathbf{d}\mathbf{r}^N \mathbf{d}\mathbf{p}^N, \quad (3.5)$$

where integrations are over all the values of \mathbf{r} and \mathbf{p} of the phase space and $\rho(\mathbf{r}, \mathbf{p})$ is the probability density of the ensemble. This can be written through the partition function \mathcal{Z} of the ensemble as:

$$\rho(\mathbf{r}, \mathbf{p}) = \frac{1}{\mathcal{Z}} \exp(-\beta \mathcal{H}(\mathbf{r}, \mathbf{p})) \quad (3.6)$$

where \mathcal{H} is the Hamiltonian, k_B the Boltzmann constant and T the temperature. The connection between statistical mechanics and MD simulations requires the validity of the ergodic hypothesis, which is implied. Then the time average is equal to the ensemble average:

$$\langle A \rangle_{time} = \langle A \rangle \quad (3.7)$$

and the latter can be therefore written as:

$$\langle A \rangle = \langle A \rangle_{time} = \lim_{t \rightarrow \infty} \frac{1}{t} \int_0^t A(\mathbf{r}^N, \mathbf{p}^N) \mathbf{d}\tau \simeq \frac{1}{M} \sum_{t=1}^M A(\mathbf{r}^N, \mathbf{p}^N) \quad (3.8)$$

where t is the length of the simulation, M is the number of time steps in the simulation and $A(\mathbf{r}, \mathbf{p})$ is the instantaneous value of A . The validity of the ergodic hypothesis in MD simulations is strictly related to the generation of enough representative conformations of the phase space. If this is the case, the equality (3.7) is satisfied and the significant observables regarding structure, dynamics and thermodynamics can be calculated via Eq. (3.8).

The sampling of enough phase space during a MD simulation requires that the simulation time exceeds by far the characteristic time of molecular motions. For this reason the MD simulation of a given state point is divided in two part as previously mentioned, i.e. the *equilibration run* during which trajectories are evolved until the equilibrium is reached (typically with algorithms that rescale velocities), and *production run* during which equilibrated trajectories are stored and from which quantities of interest are calculated.

There exist different ensembles with different characteristics depending on the thermodynamic state of the collection of configuration. These comprehend:

- The Microcanonical Ensemble (NVE), when the thermodynamic state is characterized by a fixed number of particles N , a fixed volume V , and a fixed total energy E .
- The Canonical Ensemble (NVT), when the thermodynamic state is characterized by a fixed number of particles N , a fixed volume V and a fixed temperature, T .
- The Isobaric-Isothermal Ensemble (NPT), when the thermodynamic state is characterized by a fixed number of particles N , a fixed pressure P and a fixed temperature T .
- The Grand canonical Ensemble (μ V T): when the thermodynamic state is characterized by a fixed chemical potential μ , a fixed volume V and a fixed temperature T .

Since in the Microcanonical Ensemble the total energy of the system $E = \mathcal{K} + \mathcal{U}$ is conserved, this corresponds to the natural ensemble of MD when no rescaling of velocity is performed. There, for example, the temperature of the system is a calculated property. This can be accomplished via the equipartition theorem by:

$$T = \frac{2\langle \mathcal{K} \rangle}{(3N - N_C)k_B}, \quad (3.9)$$

where N_C is the number of constraints (for example $N_C = 3$ if the the system center of mass motion is removed). The pressure can be calculated using the virial theorem:

$$P = \frac{Nk_B - \frac{1}{3}\langle \mathcal{V} \rangle}{V}, \quad (3.10)$$

where $\mathcal{V} = \sum_{i=1}^N \mathbf{r}_i \cdot \mathbf{F}_i$ is the virial. MD simulations can run in different ensemble such the (NPT) and (NVT) introducing thermostats and barostats, this tools will be discussed in Section 3.3.

Relevant to MD simulations is the suitable treatment of boundaries. Periodic boundary conditions (PBC) are usually applied to calculate properties of bulk gases, liquids and crystals. This has indeed a twofold importance, because it avoids artifacts due to the boundaries of the finite simulation box (that can act as an external field) and, from the computational point of view, it enables to perform MD simulations with a relatively small number

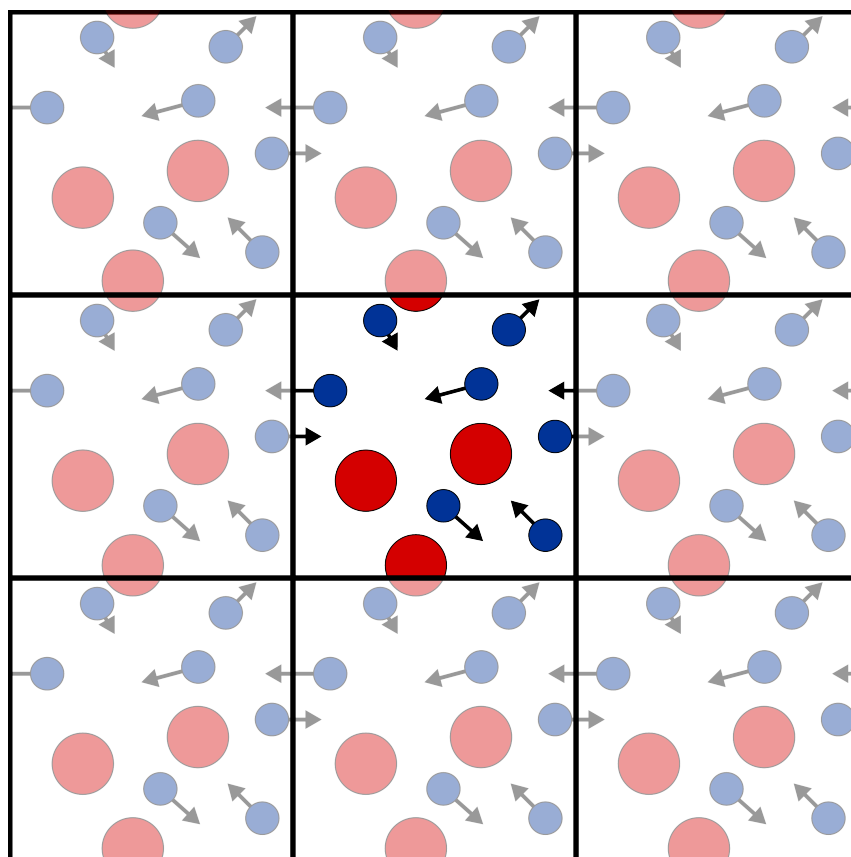


Figure 3.1: *Illustration of PBC in MD simulations.*

of molecules. Fig. 3.1 shows the common form of PBC applied for particle balance in a 2D square system. The central simulation box is replicated in all directions to construct image boxes, which give rise to a periodic lattice. Consequently, to each particle leaving the central box always corresponds one of its image entering the box from the opposite side. This preserves the number of particles in box.

3.2 Integrate the equations of motion

As was explained in the previous section the core of the Molecular Dynamic is the numerical integration of equations of motions in order to calculate the trajectories of the particles. Usually the integration time step is chosen to be much less than the time a molecule takes to cover a distance equal to its own length. Typically $\delta t = 10^{-15}$ s = 1 fs for phenomena that take place at

the picoseconds or nanoseconds scale.

In the case of rigid molecules, like in many popular models for water, the motion can be separated into translational and rotational motion. One of the most used algorithm to integrate the translational motion is the so called “leap-frog” algorithm. This algorithm is a derivation of Verlet’s algorithm [9]. The latter consider the Taylor expansion for the position, the velocity and the acceleration of a molecule:

$$\mathbf{r}_i(t + \delta t) = \mathbf{r}_i(t) + \mathbf{v}_i(t)\delta t + \frac{1}{2}\mathbf{a}_i(t)\delta t^2 + o(\delta t^3) \quad (3.11)$$

$$\mathbf{v}_i(t + \delta t) = \mathbf{v}_i(t) + \mathbf{a}_i(t)\delta t + \frac{1}{2}\mathbf{b}_i\delta t^2 + o(\delta t^3) \quad (3.12)$$

$$\mathbf{a}_i(t + \delta t) = \mathbf{a}_i(t) + \mathbf{b}_i(t)\delta t + o(\delta t^2) \quad (3.13)$$

To simplify the previous equations one can consider

$$\mathbf{r}_i(t - \delta t) = \mathbf{r}_i(t) - \mathbf{v}_i(t)\delta t + \mathbf{a}_i(t)\delta t^2 + o(\delta t^3), \quad (3.14)$$

and summing it with the Eq.3.11 the result is

$$\mathbf{r}_i(t + \delta t) = 2\mathbf{r}_i(t) - \mathbf{r}_i(t - \delta t) + \mathbf{a}_i(t)\delta t^2 + o(\delta t^4). \quad (3.15)$$

In this way the velocity term from the equation for the position can be eliminated, making the algorithm faster. In the Verlet procedure the velocity can be recovered calculating

$$\mathbf{v}_i = \frac{\mathbf{r}_i(t + \delta t) - \mathbf{r}_i(t - \delta t)}{2\delta t} \quad (3.16)$$

Verlet’s algorithm is fast and robust but it does not allow an accurate computation of the velocities. This can be amended with the leap-frog algorithm.

Given the quantities $\mathbf{r}_i(t)$, $\mathbf{a}_i(t)$ and $\mathbf{v}_i(t - \frac{1}{2}\delta t)$ a two step iteration is made, in which first the velocities are updated through

$$\mathbf{v}_i\left(t + \frac{1}{2}\delta t\right) = \mathbf{v}_i\left(t - \frac{1}{2}\delta t\right) + \mathbf{a}_i(t)\delta t \quad (3.17)$$

then the positions of the particles are calculated with:

$$\mathbf{r}_i(t + \delta t) = \mathbf{r}_i(t) + \mathbf{v}_i\left(t + \frac{1}{2}\delta t\right)\delta t \quad (3.18)$$

The forces are calculated after the second step and the new accelerations can be put into Eq. (3.17) to begin a new iteration. A diagram of the leap-frog iteration algorithm is depicted in Fig. 3.2 .

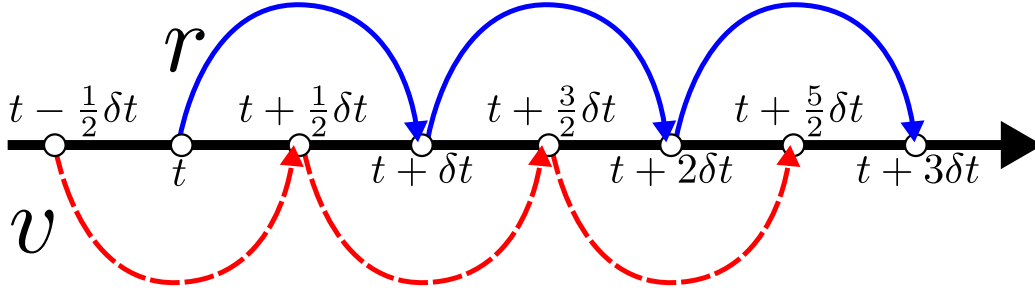


Figure 3.2: Schematic representation of the leap-frog algorithm. Dashed red lines represent the first step, Eq. (3.17), with the calculation of the velocities while solid blue lines represent the second step, Eq. (3.18), with the calculation of the positions.

Respect to the Verlet algorithm the leap-frog yields a more accurate positions. They are in fact calculated using a velocity at a time closer to $t + \delta t$. The forces are computed taking the derivative of the potential generated by the distribution of particles ensuing from Eq. (3.18). Velocities at time t can be simply obtained from the relation

$$\mathbf{v}_i = \frac{\mathbf{v}_i(t + \frac{1}{2}\delta t) + \mathbf{v}_i(t - \frac{1}{2}\delta t)}{2} \quad (3.19)$$

While the integration of the translational motion is quite straightforward, the rotational motion of molecules requires a more complex treatment. The vector τ_i , the torque with respect to the center of mass of the molecule positioned at \mathbf{r}_i , is defined by

$$\tau_i = \sum_a (\mathbf{r}_{ia} - \mathbf{r}_i) \times \mathbf{F}_{ia} \equiv \sum_a \mathbf{d}_i \times \mathbf{F}_{ia} \quad (3.20)$$

where \mathbf{d}_{ia} denotes the position of the atom a within the molecule i with respect to its center of mass. The orientation of a rigid body in the space can be defined by a rotation matrix that consents the transformation from the frame of reference of the laboratory to the one of the center of mass. This matrix is usually defined in terms of three independent angular parameters, the *Euler angles* (ϕ, θ, ψ) . A quadri-dimensional vector, with unitary norm, can be defined as a function of the Euler angles. This vector is called quaternion and it permits to have convergent equations of motion. Defined \mathbf{q} as

$$\mathbf{q} = (q_0, q_1, q_2, q_3) \quad (3.21)$$

with $q_0^2 + q_1^2 + q_2^2 + q_3^2 = 1$, the rotation matrix can be written in terms of \mathbf{q} . It reads

$$\mathcal{R} = \begin{pmatrix} q_0^2 + q_1^2 - q_2^2 - q_3^2 & 2(q_1q_2 + q_0q_3) & 2(q_1q_3 - q_0q_2) \\ 2(q_1q_2 - q_0q_3) & q_0^2 - q_1^2 + q_2^2 - q_3^2 & 2(q_2q_3 + q_0q_1) \\ 2(q_1q_3 + q_0q_2) & 2(q_2q_3 + q_0q_1) & q_0^2 - q_1^2 - q_2^2 + q_3^2 \end{pmatrix} \quad (3.22)$$

and if $\hat{\mathbf{d}}_{ia}$ is the position of the atom i in the center of mass frame, its position in the laboratory frame is obtained by $\mathbf{d}_{ia} = \mathcal{R}^T \hat{\mathbf{d}}_{ia}$. The quaternion for each molecule satisfies the equations of motion:

$$\begin{pmatrix} \dot{q}_0 \\ \dot{q}_1 \\ \dot{q}_2 \\ \dot{q}_3 \end{pmatrix} = \begin{pmatrix} q_0 & -q_1 & -q_2 & -q_3 \\ q_1 & q_0 & -q_3 & q_2 \\ q_2 & q_3 & q_0 & -q_1 \\ q_3 & -q_2 & q_1 & q_0 \end{pmatrix} \cdot \begin{pmatrix} 0 \\ \omega_x \\ \omega_y \\ \omega_z \end{pmatrix} \quad (3.23)$$

where $(0, \omega_x, \omega_y, \omega_z)$ are the components of the angular velocity vector $\boldsymbol{\omega}$ in the center of mass frame. This system does not possess singularities and it can be solved with a procedure similar to the one applied for the integration of the translational motion. To solve the rotational motion the following equation can be used:

$$\frac{d\mathbf{J}}{dt} = \frac{d}{dt} (I\boldsymbol{\omega}) = \boldsymbol{\tau} \quad (3.24)$$

where \mathbf{J} is the total angular momentum of the molecule, I the moment of inertia matrix and $\boldsymbol{\tau}$ the torque of the molecule (for convenience here the subscript i indicating each molecule is dropped). This equation is evidently coupled to Eq. (3.23). Having stored $\mathbf{J}(t - \delta t)$, $\mathbf{q}(t)$ and $\boldsymbol{\tau}(t)$ the equations for the rotational motion can be solved iteratively, first updating the angular momentum through:

$$\mathbf{J} = \mathbf{J} \left(t - \frac{1}{2}\delta t \right) + \boldsymbol{\tau}(t) \frac{1}{2}\delta t \quad (3.25)$$

Then the $\dot{\mathbf{q}}$ can be calculated from Eq. (3.23) and a guess for $\mathbf{q}(t + \frac{1}{2}\delta t)$ is given by:

$$\mathbf{q} \left(t + \frac{1}{2}\delta t \right) = \mathbf{q}(t) + \dot{\mathbf{q}}(t) \frac{1}{2}\delta t \quad (3.26)$$

The last two are auxiliary equations to estimate $\mathbf{q}(t + \frac{1}{2}\delta t)$ and calculate \mathbf{q} at the half-step time. Now the new \mathbf{J} and \mathbf{q} can be calculated through the relations:

$$\mathbf{J} \left(t + \frac{1}{2}\delta t \right) = \mathbf{J} \left(t - \frac{1}{2}\delta t \right) + \boldsymbol{\tau}(t)\delta t \quad (3.27)$$

$$\mathbf{q}(t + \delta t) = \mathbf{q}(t) + \dot{\mathbf{q}}\left(t + \frac{1}{2}\delta t\right) \delta t \quad (3.28)$$

Another way to reproduce the motion of a rigid body are the constraint algorithms. This method involves the introduction of a constraint in the distance between the positions of atoms composing the molecules. The general steps involved are the follows:

1. Let the particle move separately.
2. Introduce explicit constraint forces.
3. Minimize this forces using the technique of Lagrange multipliers or another method.

Lagrangian multipliers

The method of the Lagrangian multipliers is widely used in MD simulations to minimize the force of the constraints. We introduce a set of n linear (holonomic) constraints at the time t ,

$$\sigma_k(t) := \|\mathbf{x}_{k\alpha}(t) - \mathbf{x}_{k\beta}(t)\|^2 - d_k^2 = 0, \quad k = 1 \dots n \quad (3.29)$$

where $\mathbf{x}_{k\alpha}(t)$ and $\mathbf{x}_{k\beta}(t)$ are the positions of the two particles involved in the constraint k and d_k is the intramolecular distance fixed by the constraint. The equations of motion have to take into account the force due to these constraints. It is important to note that adding the constraint forces does not change the total energy, as the total work done by the constraint forces is zero as they act in the same way for the two particles but with opposite direction. For each one of the N particles in the system the force is given by:

$$\frac{\partial^2 \mathbf{x}_i(t)}{\partial t^2} m_i = -\frac{\partial}{\partial \mathbf{x}_i} \left[V(\mathbf{x}_i(t)) + \sum_{k=1}^n \lambda_k \sigma_k(t) \right], \quad i = 1 \dots N. \quad (3.30)$$

From integrating both sides of the equation with respect to the time, the constrained coordinates of particles at the time, $t + \delta t$, are given,

$$\mathbf{x}_i(t + \delta t) = \mathbf{x}_i^f(t + \delta t) + \sum_{k=1}^n \lambda_k \frac{\partial \sigma_k(t)}{\partial \mathbf{x}_i} (\delta t)^2 m_i^{-1}, \quad i = 1 \dots N \quad (3.31)$$

where $\mathbf{x}_i^f(t + \delta t)$ is the free position of the particle i after integrating the unconstrained equations of motion.

To satisfy the constraints $\sigma_k(t + \delta t)$ in the next time step, the Lagrange multipliers should be determined as the following equation,

$$\sigma_k(t + \delta t) := \|\mathbf{x}_{k\alpha}(t + \delta t) - \mathbf{x}_{k\beta}(t + \delta t)\|^2 - d_k^2 = 0. \quad (3.32)$$

This implies solving a system of n non-linear equations simultaneously for the n unknown Lagrange multipliers λ_k . This system of n non-linear equations in n unknowns is commonly solved using Newton-Raphson method.

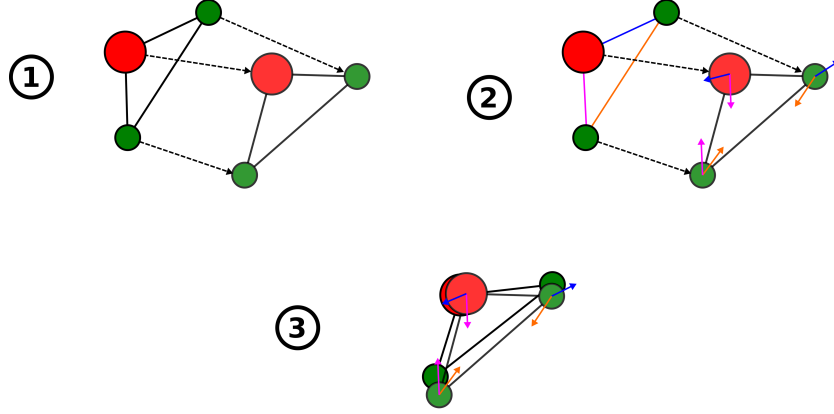


Figure 3.3: Schematic representation of the steps involved in the constraint method.

3.3 Thermostats and Barostats

As stated in Section 3.1, the NVE is the natural ensemble of basic MD. Often it is necessary to keep temperature and/or pressure fixed in a simulation, for example to mimic real thermodynamic condition of an experiment. Even in the constant NVE simulation, it is however common to regulate the temperature during the equilibration phase.

The temperature of the system is connected to the average of the kinetic energy \mathcal{K} by the equation (3.9). This gives a simple way to control the temperature of the system rescaling the velocities in order to obtain the desired temperature. In fact if the velocities are multiplied by a factor λ at time t , the variation of the temperature in the unconstrained system is given by:

$$\Delta T = \frac{1}{2} \sum_{i=0}^N \frac{2}{3} \frac{m_i (\lambda v_i)^2}{N k_B} - \frac{1}{2} \sum_{i=0}^N \frac{2}{3} \frac{m_i \lambda v_i^2}{N k_B} = (\lambda^2 - 1) T(t) \quad (3.33)$$

Thus in order to drive the current temperature of the system $T(t)$ to the desired value T_D , velocities must be multiplied at each time step by a factor λ given by:

$$\lambda = \sqrt{\frac{T_D}{T(t)}} \quad (3.34)$$

One of the most used thermostats is the one proposed by Berendsen *et al.* [76] in 1984. In that paper was proposed an alternative way to control the temperature, coupling the system whit an external heat bath at fixed temperature. In this way the external bath supplies or removes heat from the system, bringing it to the desired temperature. This method gives an exponential decay of the temperature of the system towards the desired temperature value. The change in temperature between two successive time steps is given by:

$$\frac{dT(t)}{dt} = \frac{1}{\tau} (T_B - T(t)) \rightarrow \delta T = \frac{\delta t}{\tau} (T_B - T(t)) \quad (3.35)$$

where τ is the coupling parameter between the bath and the system and T_B the temperature of the external bath. The velocities are then scaled at each time step by a quantity proportional to the difference of the temperature between the bath and the system:

$$\lambda = \left[1 + \frac{\delta t}{\tau} \left(\frac{T_B}{T(t)} - 1 \right) \right]^{\frac{1}{2}} \quad (3.36)$$

Berendsen method is relatively simple and not very demanding in term of computational power but it doesn't generate a rigorous canonical average. In fact it has been showed that quantities calculated when this method is used differ from the values of the canonical ensemble typically of $\mathcal{O}(1/N)$ [9]. In most cases this accuracy is enough and the Berendsen method is indeed common used in MD simulations, especially in the equilibration phase.

A similar procedure can be used also to control the pressure of the system. Whereas for the thermostats we act on the velocities in order to keep fixed the temperature, to maintain a constant pressure we need to change the volume of the system. The factor lambda in this case is multiplied by the volume as follows

$$\mathbf{r}'_i = \lambda^{1/3} \mathbf{r}_i \quad (3.37)$$

The Berendsen method can be applied also in this case, coupling the system to a "pressure bath" analogous to the temperature bath. The change of pressure can thus be obtained as follows:

$$\frac{dP(t)}{dt} = \frac{1}{\tau_P} (P - P_B) \quad (3.38)$$

where τ is the coupling pressure constant, P_B the pressure of the bath and $P(t)$ the instantaneous value of the pressure in the system. Volume is then rescaled by a factor:

$$\lambda = 1 - \kappa_T \frac{\delta t}{\tau_P} (P - P_B) \quad (3.39)$$

where κ_T is the isothermal compressibility describing the change of volume as response to the pressure.

$$\kappa_T = -\frac{1}{V} \left(\frac{\partial V}{\partial P} \right)_T \quad (3.40)$$

3.4 Force fields and potentials

Potential energy terms can be split in the two terms, one relative to the intramolecular interactions (bonded interactions) and the other relative to intermolecular interactions (non-bonded interactions):

$$\mathcal{U} = \mathcal{U}_{bonded} + \mathcal{U}_{non-bonded} \quad (3.41)$$

The general form of the intramolecular part is:

$$\mathcal{U}_{bonded} = \mathcal{U}_{stretch} + \mathcal{U}_{bend} + \mathcal{U}_{torsion} \quad (3.42)$$

where $\mathcal{U}_{stretch}$ describes oscillations about the equilibrium bond length, \mathcal{U}_{bend} describes oscillations of three atoms about an equilibrium bond angle, and $\mathcal{U}_{torsion}$ describes the torsional rotation of four atoms about a central bond. Rigid potential, like the SPC/E or the TIP4P constrains the internal motions of particles composing a molecule.

The intermolecular part of the potential is typically written as:

$$\mathcal{U}_{non-bonded} = \mathcal{U}_{LJ} + \mathcal{U}_{Coulomb} \quad (3.43)$$

where \mathcal{U}_{LJ} is the Lennard-Jones (LJ) potential:

$$\mathcal{U}_{LJ} = 4\epsilon \left[\left(\frac{\sigma}{r} \right)^{12} - \left(\frac{\sigma}{r} \right)^6 \right] \quad (3.44)$$

and $\mathcal{U}_{Coulomb}$ is the electrostatic potential:

$$\mathcal{U}_{Coulomb} = \frac{e^2}{4\pi\epsilon_0} \frac{q_i q_j}{r} \quad (3.45)$$

The most consuming part of the MD simulation is the calculation of non-bonded interactions, which, in most cases have a pairwise form. Typically,

non-bonded interaction are handled with a non-bonded cutoff and with the minimum image convention. According to this convention each particle in the simulation box interacts only with the closest image of the remaining particles in the system. When the non-bonded cutoff is employed, the interaction between pairs at distance major than the cutoff value are set to zero and are therefore calculated only for distance $r = |r - r| \neq r_{cut} < L/2$, where L is the linear dimension of the box and the upper limit is introduced to avoid considering the same particle twice due to the PBC. With the introduction of the cut-off scheme for non-bonded interactions, corrections must be in general introduced in the interaction potentials [9]. For short range potential, as the Lennard-Jones potential, corrections are typically performed in the real space. For long range potential, like the electrostatic interactions, corrections are often handled in the Fourier space, for example as in the Particle Mesh Ewald method (see next Section) .

3.5 Ewald summation

In order to perform simulation of large systems in a reasonable time and to avoid divergences due to PBC there is the necessity to introduce the cutoff in the interactions we dealt with in the previous paragraph. Special care is needed in dealing with potential truncation of long range contributions, like for example electrostatic interactions. It is known that the inadequate treatment of these interactions can lead to severe artifacts in the results of the simulations [77]. The Ewald summation method is one of the most used technique to deal with this problem. In the following the general ideas of this method are described. Taking into account the periodic boundary conditions, the electrostatic energy term of the interaction potential can be written as

$$\mathcal{U}_E = \frac{1}{2} \sum_{i=1}^N q_i \phi_E(\mathbf{r}_i) \quad (3.46)$$

and ϕ_E is given by

$$\phi_E = \sum_{j=1}^N \sum_{\mathbf{R}} \frac{q_j}{|\mathbf{r}_{ij} + \mathbf{R}|} \quad (3.47)$$

where $\mathbf{R} = \mathbf{n}L$, $\mathbf{n} = (n_x, n_y, n_z)$, with $n_x, n_y, n_z \in \mathbf{Z}$. The sum is performed with the convention that $i = j$ if $\mathbf{R} = 0$. By adding and subtracting screening charges, the sum can be broken into two parts, $\mathcal{U}_E = \mathcal{U}_{SR} + \mathcal{U}_{LR}$. The first part contains the original point charges screened by diffuse clouds of opposite charges; this part becomes short ranged and can

be evaluated in the real space. The second part compensates for the added screening charges and it is generated by the sum of the screening charge densities (with opposite charge); it is evaluated in the Fourier space. The screening charges are typically taken with a Gaussian distribution:

$$\rho_s(r) = q_i \left(\frac{\alpha}{\pi}\right)^{3/2} e^{-\alpha r^2} \quad (3.48)$$

First the long range part of the sum must be calculated. Having taken the screening charges as in Eq. (3.48), the compensating charge distribution can be written as

$$\rho_c(\mathbf{r}) = \sum_{j=1}^N \sum_{\mathbf{R}} q_j \left(\frac{\alpha}{\pi}\right)^{3/2} \exp[-\alpha |\mathbf{r} - (\mathbf{r}_j + \mathbf{R})|^2] \quad (3.49)$$

and its Fourier transform is given by

$$\tilde{\rho}_c(\mathbf{k}) = \int_V d\mathbf{r} e^{-i\mathbf{k}\cdot\mathbf{r}} \rho_c(\mathbf{r}) = \sum_{j=1}^N q_j e^{-i\mathbf{k}\cdot\mathbf{r}_j} e^{-k^2/4\alpha}. \quad (3.50)$$

The field generated by this charge distribution can be calculated using the Poisson's equation in the Fourier space, $k^2 \tilde{\phi}(\mathbf{k}) = 4\pi \tilde{\rho}(\mathbf{k})$. Antitransforming the field thus obtained and plugging it into the long range part of the sum, it follows:

$$\mathcal{U}_{LR} = \frac{1}{2} \sum_{i=1}^N q_i \phi_c(\mathbf{r}_i) = \frac{1}{2V} \sum_{\mathbf{k} \neq 0} \frac{4\pi}{k^2} |\tilde{\rho}(\mathbf{k})|^2 e^{-k^2/4\alpha} \quad (3.51)$$

where $\tilde{\rho}(\mathbf{k}) = \sum_{i=1}^N q_i e^{-i\mathbf{k}\cdot\mathbf{r}_i}$. This part of the potential contains spurious self-interactions terms as the point charges at \mathbf{r}_i interact with the compensating charges also at \mathbf{r}_i . The self interactions terms represent the potential at center of the Gaussian charge distributions and they are to be subtracted from the final expression to recover the correct Coulombic energy. Now the short range part of the sum is calculated. Using the Poisson's equation in the real space $-\nabla^2 \phi(\mathbf{r}) = 4\pi \rho(\mathbf{r})$ it is possible to demonstrate that the screening potential can be written as

$$\phi_s(r) = \frac{q_i f_{er}(\alpha^{1/2} r)}{r} \quad (3.52)$$

where f_{er} is the error function. It is defined by

$$f_{er}(x) = \frac{2}{\pi^{1/2}} \int_0^x e^{-t^2} dt. \quad (3.53)$$

The self-interaction terms correspond to $\varphi_{self} = \varphi_s(0) = 2 \left(\frac{\alpha}{\pi}\right)^{1/2} q_i$ and the total self-interaction energy becomes

$$\mathcal{U}_{self} = \left(\frac{\alpha}{\pi}\right)^{1/2} \sum_{i=1}^N q_i \quad (3.54)$$

which must be subtracted from the total electrostatic energy. Using the result (3.52), the short range part of the sum can be rewritten as

$$\begin{aligned} \mathcal{U}_{SR} &= \frac{1}{2} \sum_{\mathbf{R}} \sum_{i \neq j}^N q_i q_j \frac{1 - f_{er}(\alpha^{1/2} |\mathbf{r}_{ij} + \mathbf{R}|)}{|\mathbf{r}_{ij} + \mathbf{R}|} = \\ &= \frac{1}{2} \sum_{\mathbf{R}} \sum_{i \neq j}^N q_i q_j \frac{f_{er}^c(\alpha^{1/2} |\mathbf{r}_{ij} + \mathbf{R}|)}{|\mathbf{r}_{ij} + \mathbf{R}|} \end{aligned} \quad (3.55)$$

where f_{er}^c is the complementary error function defined by

$$f_{er}^c(x) = 1 - f_{er}(x) = \frac{2}{\pi^{1/2}} \int_x^{\infty} e^{-t^2} dt. \quad (3.56)$$

Putting all the terms together the final result is obtained:

$$\begin{aligned} \mathcal{U}_E = \mathcal{U}_{SR} + \mathcal{U}_{LR} - \mathcal{U}_{self} &= \frac{1}{2} \sum_{\mathbf{R}} \sum_{i \neq j}^N q_i q_j \frac{f_{er}^c(\alpha^{1/2} |\mathbf{r}_{ij} + \mathbf{R}|)}{|\mathbf{r}_{ij} + \mathbf{R}|} \\ &+ \frac{1}{2V} \sum_{\mathbf{k} \neq 0} \frac{a\pi}{k^2} |\tilde{\rho}(\mathbf{k})|^2 e^{-k^2/4\alpha} - \left(\frac{\alpha}{\pi}\right)^{1/2} \sum_{i=1}^N q_i \end{aligned} \quad (3.57)$$

The original sum has been thus separated into two parts. The short range sum is performed in the real space while the long range sum is performed in the Fourier space. The tuning of the parameter α results particularly important in determining the convergence of the integrals. In order to get fast convergence α should be large in the real space and small in the Fourier space. A balance of these needs is usually considered and typically α is set to values of the order of $5/L$ [9], taking a number of wave vectors of the order of ten for the computation of the sums over \mathbf{k} .

3.6 The SPC/E model of water

Several classic rigid model potential are usually successfully used for water. Here is described one of these popular potential that will be used for simulations in the present work: the SPC/E water. Berendsen *et al.* [78] developed

the *simple point charge extended* (SPC/E) model of water in 1987. This potential consists of an improvement of the existing SPC (*simple point charge*) model with the inclusion of a polarization correction to the energy and the consequent reparametrization of the older SPC model. This was aimed to best reproduce properties of polar liquids. The SPC/E water molecule is shown in Fig. 3.4. The three interaction sites are coplanar, the O–H distance is 1 Å and the angle is 109.5°. Point charges lie on the oxygen position with $q_O = -0.8476e$ and on the hydrogen positions with $q_H = +0.4238e$. On the oxygen position also lies the only Lennard-Jones interaction site of the molecule with $\epsilon_{OO} = 0.650$ kJ/mol and $\sigma_{OO} = 3.166$ Å. The complete interaction potential of the i -th water molecule can thus be written as:

$$u(r_{ij}) = 4 \epsilon_{ij} \left[\left(\frac{\sigma_{ij}}{r_i - r_j} \right)^{12} - \left(\frac{\sigma_{ij}}{r_i - r_j} \right)^6 \right] + \frac{e^2}{4 \pi \epsilon_0} \frac{q_i q_j}{|r_i - r_j|}.$$

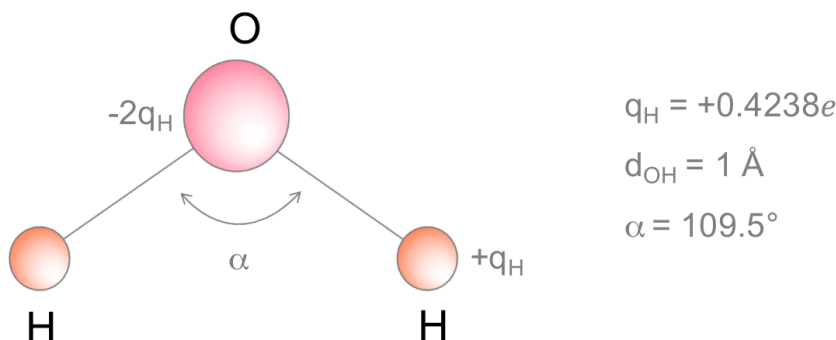


Figure 3.4: Geometry of SPC/E model of water.

3.7 The CHARMM FF for proteins, disaccharides and DMSO

This paragraph describes the potential used for the protein, the disaccharide and for dimethyl sulfoxide molecules.

CHARMM (*Chemistry at Harvard Macromolecular Mechanics*) is a set of force fields widely used for molecular dynamics simulation of saccharides, lipids, protein, nucleic acids and other biochemical compounds and ions [79–84].

Interaction potentials of CHARMM are divided in two contribution:

$$\mathcal{U} = \mathcal{U}_{bonded} + \mathcal{U}_{non-bonded}.$$

3.7. THE CHARMM FF FOR PROTEINS, DISACCHARIDES AND DMSO57

The first part accounts for the interactions between chemically bonded nearest neighbours and is composed by bonded energy terms that describe bond stretching, angle bending, dihedral and improper dihedral energy:

$$\mathcal{U}_{bonded} = \mathcal{U}_{bond} + \mathcal{U}_{angle} + \mathcal{U}_{dihedral} + \mathcal{U}_{improper} + \mathcal{U}_{UB} + \mathcal{U}_{CMAP},$$

where

$$\begin{aligned}\mathcal{U}_{bond} &= \sum_{bonds} K_b (b - b^0)^2, \\ \mathcal{U}_{angle} &= \sum_{angles} K_\theta (\theta - \theta^0)^2, \\ \mathcal{U}_{dihedral} &= \sum_{dihedrals} K_\phi (1 + \cos(n\phi - \delta)), \\ \mathcal{U}_{impropers} &= \sum_{impropers} K_\omega (\omega - \omega^0)^2, \\ \mathcal{U}_{UB} &= \sum_{Urey-Bradley} K_{UB} (b^{1-3} - b^{1-3,0})^2, \\ \mathcal{U}_{CMAP} &= \sum_{residues} u_{CMAP}(\phi, \psi).\end{aligned}$$

The first term in the energy function accounts for the bond stretches where K_b is the bond force constant and $b - b^0$ is the distance from equilibrium that the atom has moved. The second term in the equation accounts for the bond angles where K_θ is the angle force constant and $\theta - \theta^0$ is the angle from equilibrium between 3 bonded atoms. The third term is for the dihedrals (the torsion angles) where K_ϕ is the dihedral force constant, n is the multiplicity of the function, ϕ is the dihedral angle and δ is the phase shift. The fourth term accounts for the impropers, that is out of plane bending, where K_ω is the force constant and $\omega - \omega^0$ is the out of plane angle. The last two terms have been introduced in CHARMM. The Urey-Bradley term is a harmonic term in the distance between atoms 1 and 3 that forms an angle θ . This term improves in-plane deformations and vibrational spectra by separating symmetric and asymmetric bond stretching modes [79]. The CMAP term [80] is a cross-term for backbone dihedral angles ϕ and ψ realized by grid based energy correction maps. This is applied in CHARMM forcefield to improve dihedral angles of only protein backbones.

The non-bonded part of the potential, $\mathcal{U}_{non-bonded}$, consists of the usual Lennard-Jones and Coulombic interaction terms

$$\mathcal{U}_{non-bonded} = \mathcal{U}_{LJ} + \mathcal{U}_{Coulomb}.$$

3.8 MD observables

In this section the observables used in this study are defined.

3.8.1 Dynamical quantities

Dynamical state of a liquid is often characterized through the use of correlation functions [63]. Given two observable $A(t')$ and $B(t'')$ that are functions of the time-varying coordinates \mathbf{r}_i and momenta \mathbf{r}_i , their correlation function is defined as

$$C_{AB}(t', t'') = \langle A(t')B(t'') \rangle = \lim_{\tau \rightarrow \infty} \frac{1}{\tau} \int_0^\tau A(t' + t)B(t'' + t)dt \quad (3.58)$$

with the convention $t' \geq t''$. At equilibrium the correlation is invariant under time translation and defining $t = t' - t''$, one have

$$C_{AB}(t) = \langle A(t')B(t'') \rangle = \langle A(t)B(0) \rangle. \quad (3.59)$$

The two limit cases are

$$\lim_{t \rightarrow 0} C_{AB}(t) = \langle A(0)B(0) \rangle \equiv \langle AB \rangle, \quad (3.60)$$

known as static correlation function, and

$$\lim_{t \rightarrow \infty} C_{AB}(t) = \langle A \rangle \langle B \rangle, \quad (3.61)$$

because A and B become uncorrelated.

Correlation functions are often normalized by their value at initial time

$$\hat{C}_{AB}(t) = \frac{\langle A(t)B \rangle}{\langle AB \rangle}. \quad (3.62)$$

In the case in which $A(t) = B(t)$, the correlation is called *autocorrelation function*

$$C_{AA}(t) = \langle A(t)A(0) \rangle. \quad (3.63)$$

Self Intermediate Scattering Function

Density correlations are of great interest in the study of the physics of liquids. The self part of the density-density correlation function is called the van Hove function, $G_s(\mathbf{r}, t)$, and it is defined as [63]:

$$G_s(\mathbf{r}, t) = \frac{1}{N} \left\langle \sum_i^N \delta(\mathbf{r} - \mathbf{r}_i(0) - \mathbf{r}_i(t)) \right\rangle. \quad (3.64)$$

It represents the probability density of finding a particle i in the vicinity of \mathbf{r} at time t given that it was in the origin at time 0.

The Self Intermediate Scattering Function (SISF) is defined as the spatial Fourier transform of van Hove function and thus reads:

$$F_s(\mathbf{q}, t) \equiv \int G_s(\mathbf{r}, t) e^{-i\mathbf{q}\cdot\mathbf{r}} d\mathbf{r}.$$

The SISF can be rewritten in a form that permits to calculate it directly from the atomic trajectories of an MD simulation. In fact it can be shown that it is the autocorrelation function of the Fourier components of the local density in the \mathbf{q} space

$$F_S(\mathbf{q}, t) = \frac{1}{N} \langle \rho_{\mathbf{q}}(t) \rho_{-\mathbf{q}}(0) \rangle = \left\langle \frac{1}{N} \sum_{i=1}^N e^{i\mathbf{q}\cdot(\mathbf{r}_i(t) - \mathbf{r}_i(0))} \right\rangle \quad (3.65)$$

where N is the number of particles and $\mathbf{r}_i(t)$ is the position of the i -th particle at time t . The SISF probes the single-particle translational dynamics of the system and characterizes its structural relaxation phenomena. This function can be directly compared to experiments from inelastic neutron or X-ray scattering.

SISF is a fundamental quantity to study the dynamics of a system, especially in the MCT framework (see Chapter 2).

Mean Square Displacement

The Mean Square Displacement (MSD) is defined as:

$$\langle \Delta r^2(t) \rangle \equiv \left\langle \frac{1}{N} \sum_{i=1}^N (\mathbf{r}_i(t) - \mathbf{r}_i(0))^2 \right\rangle \quad (3.66)$$

where N is the number of particles and $\mathbf{r}_i(t)$ is the position of the i -th particle at time t . It can be showed that the MSD is related to the velocity autocorrelation function [63].

Experimental methods to determine MSDs include neutron scattering and photon correlation spectroscopy.

MSD gives a direct way to study the diffusive regime of the system under investigation. Writing the MSD as a power law

$$\langle \Delta r^2(t) \rangle \propto t^\alpha$$

one can have, depending on the value of the exponent α , different regimes [85]:

- $0 < \alpha < 1$ sub-diffusive regime,
- $\alpha = 1$ diffusive regime,
- $1 < \alpha < 2$ super-diffusive regime,
- $\alpha = 2$ ballistic regime.

Fig. 3.5 reports, as an example, the oxygen-oxygen Self Intermediate Scattering Function and the oxygen Mean Square Displacement of bulk SPC/E water for temperature in the 320-200 K range and at $P = 1$ bar. It is evident from both quantities how the dynamics of the system is dominated by the cage effect.

It is interesting to briefly comments on some features of the SISFs that are evident in the top panels of Fig. 3.5 . In the correlators calculated in the 210-200 K temperature range a small peak at around 1 ps, followed by some oscillations, is observed. The latter are due to finite size effects connected with the size of the simulation box and to the number of contained water molecules [86]. The first peak is the Boson Peak, a collective mode that has been observed in many supercooled glassy systems. The Boson Peak is a debated low temperature feature of supercooled water and should be a sort of signature of the disordered amorphous state of water. Recently its onset in water has been also connected to the presence of a liquid-liquid Widom Line both in bulk and confined water [86–90].

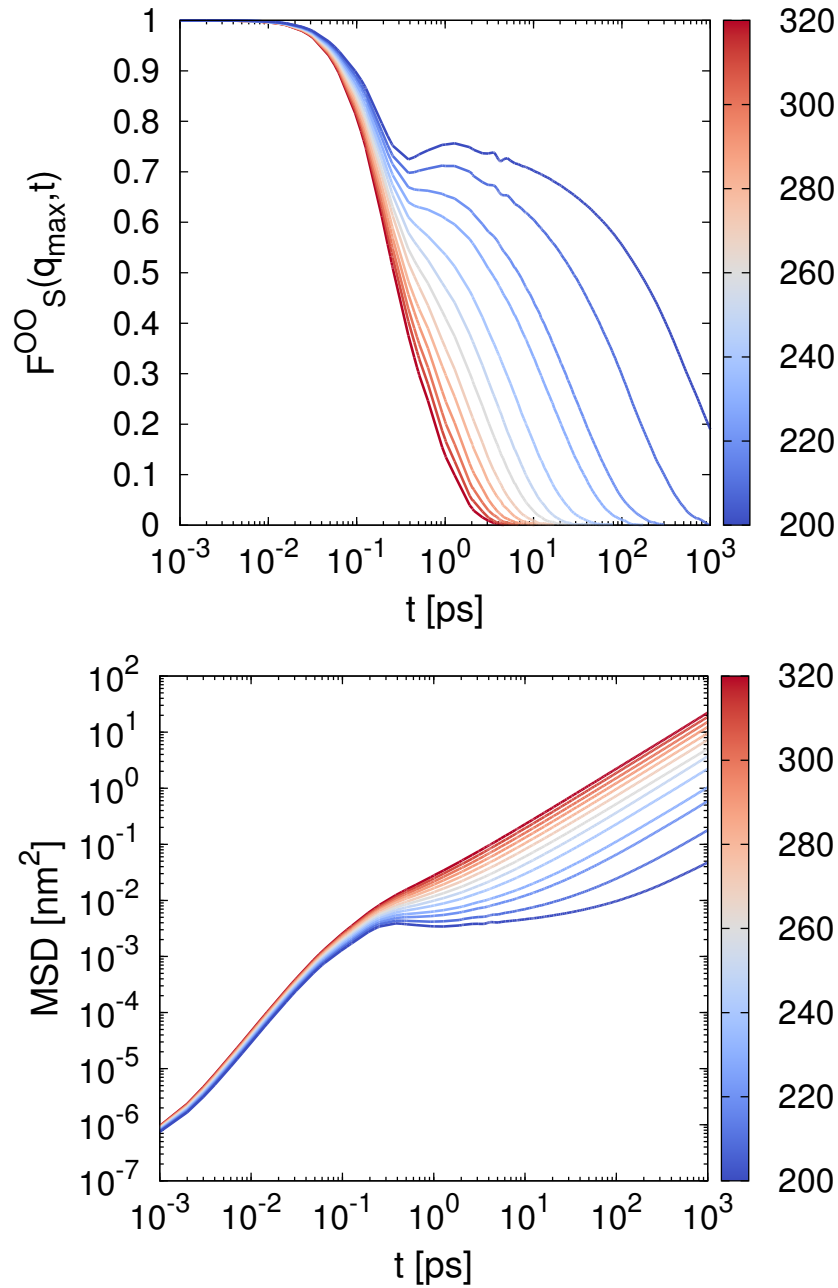


Figure 3.5: *Top panel: SISFs of the oxygen atom of SPC/E bulk water for different temperature at $P = 1$ bar. Bottom panel: MSDs of the oxygen atom of SPC/E bulk water for different temperature at $P = 1$ bar. Different diffusive regimes are easily recognizable.*

3.8.2 Structural quantities

Radial Distribution Function

The Radial Distribution Function (RDF) $g(r)$ gives the probability of finding a pair of particles at distance r , relative to the probability expected for a completely random distribution at the same density. Its definition takes an ensemble average over pairs [63]

$$g(r) = \frac{V}{N^2} \left\langle \sum_i \sum_{j \neq i} \delta(r - r_{ij}) \right\rangle$$

where N is the particle number and V the volume of the system. RDF is a very useful quantity to gain insight on the internal structure of the system under investigation in that it shows striking differences depending on the phase the system is in (see Fig. 3.6).

Fig. 3.7 reports different Radial Distribution Function for a simulation of SPC/E water at $P = 1$ bar. It can be seen that, upon lowering the temperature, the peaks become more sharp and move towards smaller distances from the tagged particle, as expected from a system whose structure is becoming more regular defined. As additional test of this hypothesis, it is interesting to note that the first peak of the oxygen-oxygen RDF (formed by nearest neighbours molecules) is around $r = 0.28$ nm. Reporting this value in the MSD plot (bottom panel of Fig. 3.5), one obtains a value of the $MSD \simeq 0.08$ nm² that perfectly match the plateau values of MSDs.

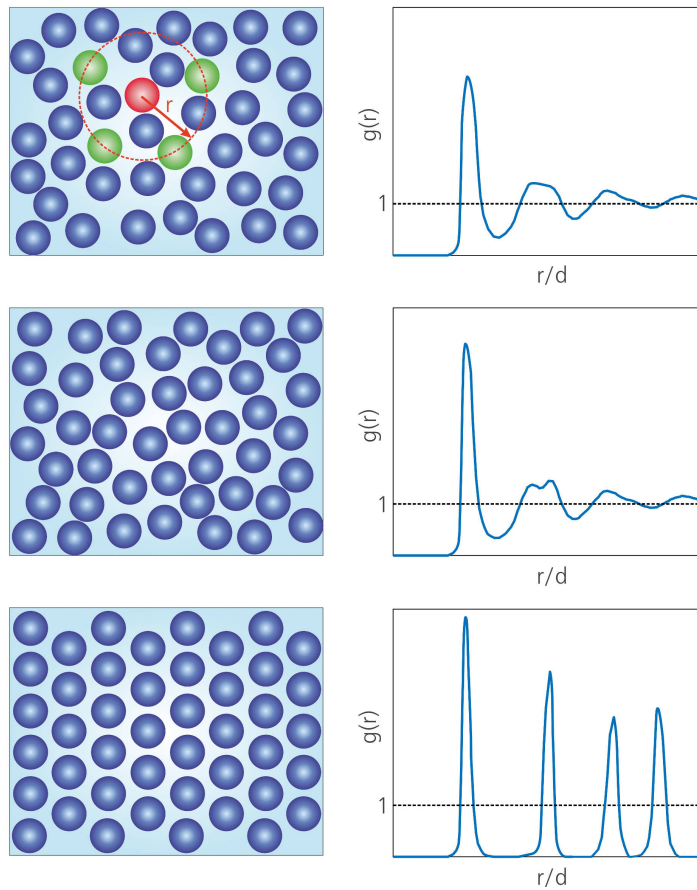


Figure 3.6: Representation of the structure of a system with the associated $g(r)$. Top panels refers to a normal liquid, middle panel to an amorphous solid, bottom panel to a crystalline solid. Dashed black lines indicate the ideal-gas result. Image adapted from Ref. [61]

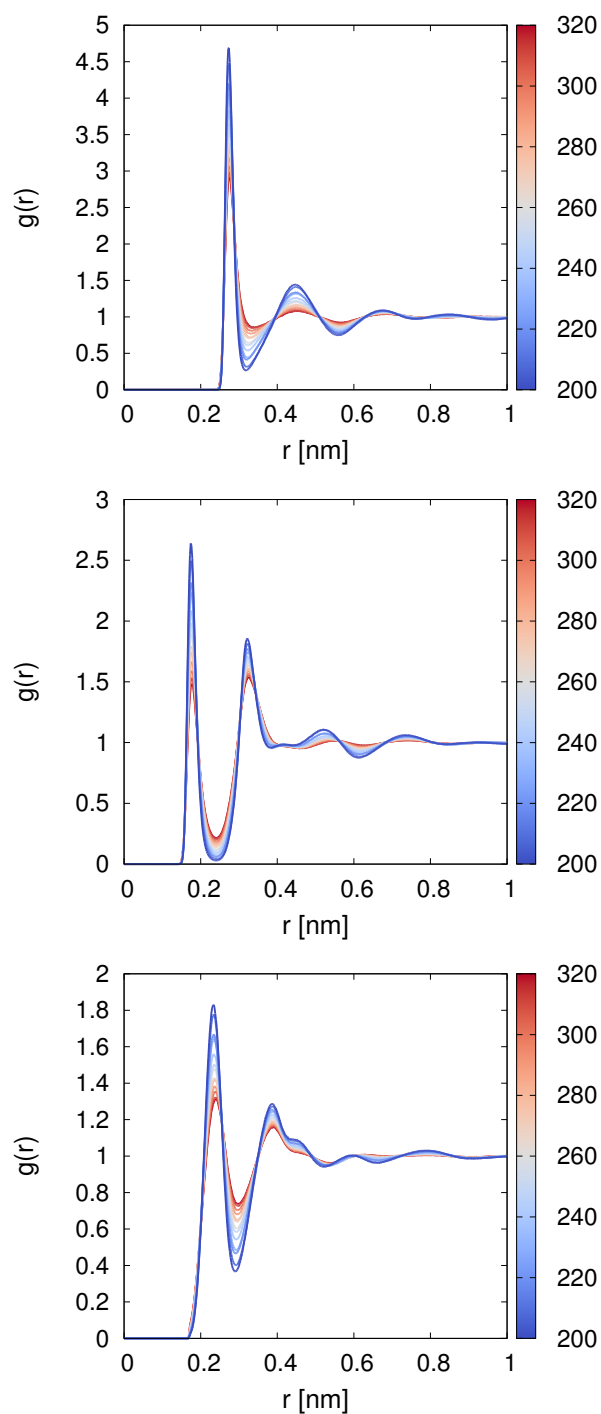


Figure 3.7: Oxygen-oxygen (top panel), oxygen-hydrogen (middle panel) and hydrogen-hydrogen (bottom panel) Radial Distribution Function for SPC/E water model at $P = 1$ bar.

Hydrogen Bond

A Hydrogen Bond between a donor and an acceptor can be defined with different criteria regarding the geometry or the energetics. In this work a geometrical criterion is used to define whether a hydrogen bond between two water molecules exists. A commonly used geometrical criterion is the following. A donor oxygen atom and an acceptor oxygen atom are hydrogen bonded if

1. the r_{OO} distance is less than a cutoff distance
2. the acceptor-donor-hydrogen angle, $\alpha = \text{H}-\hat{\text{O}}\cdots\text{O}$ is less than or equal to a cutoff angle

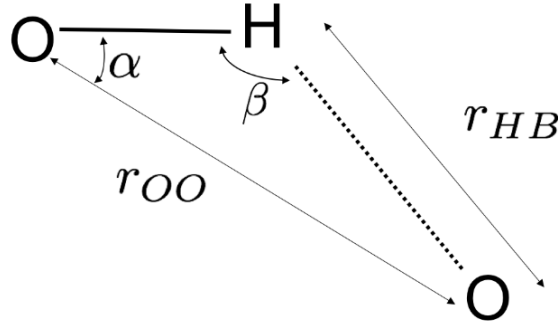


Figure 3.8: Geometry of the O–H group of the donor water molecule and the O atom of the acceptor water molecule involved in a Hydrogen Bond.

This condition is shown in Fig. 3.8. Typically the first minimum of the radial distribution function between the donor and the acceptor is used as the cutoff distance. The cutoff angle is chosen to guarantee the linearity of the HB bond inside a certain cone value.

HB between water molecules are defined in this work by the condition used in Ref. [91]

$$\begin{aligned} r_{OO} &< 3.5 \text{ \AA} \\ \alpha &< 30^\circ. \end{aligned}$$

Orientational Tetrahedral Order parameter

The orientational order parameter is defined by [92]

$$q = 1 - \frac{3}{8} \sum_{j=1}^3 \sum_{k=j+1}^4 \left(\cos(\gamma_{jk}) + \frac{1}{3} \right)^2. \quad (3.67)$$

where γ_{jk} is the angle formed by the lines joining the oxygen atom of a given molecule and those of its first four nearest neighbours j and k . This parameter is used to quantify the degree of tetrahedrality of the local structure of a system. The average value of q varies between 0 for an ideal gas and 1 for a system with perfect tetrahedral arrangement.

Fig. 3.9 reports the fraction of water molecules with a given number of Hydrogen Bonds (top panel), the distribution of $\cos(\gamma)$, with γ the angle between three nearest neighbours water molecules, and the Orientational Tetrahedral Order parameter q (bottom panel) as functions of the temperature T for an MD simulations of SPC/E water at $P = 1$ bar.

At high temperature a significant amount of water molecules is bonded with two, three, four and even five hydrogen bonds to other water molecules. As the temperature of the system decrease the number of water molecules that form four HBs with other water molecules increase sharply.

The distribution of $\cos(\gamma)$ shows two maxima. The first sharp peak around 0.6 (that corresponds to $\sim 53^\circ$) is associated to interstitial neighbours molecules and is fixed upon cooling the system. The second broad peak is around $\cos(\gamma) = -0.24$ ($\sim 103.8^\circ$) for high T. Upon cooling this peak becomes sharper and moves towards $\cos(\gamma) = -0.30$ ($\sim 107.4^\circ$) at $T = 200$ K, thus signaling an increasing tetrahedral order. To what extent the degree of tetrahedrality in the structure of the hydrogen bond network changes upon varying the temperature is clearly visible using the distribution of the Orientational Tetrahedral Order parameter. At high temperature the distribution is broad, with two small peaks at around $q = 0.5$ and $q = 0.7$. Upon lowering the temperature the first peak becomes a small shoulder, while the second one increase and moves towards higher values of q , till it becomes a sharp peak at around $q \simeq 0.85$.

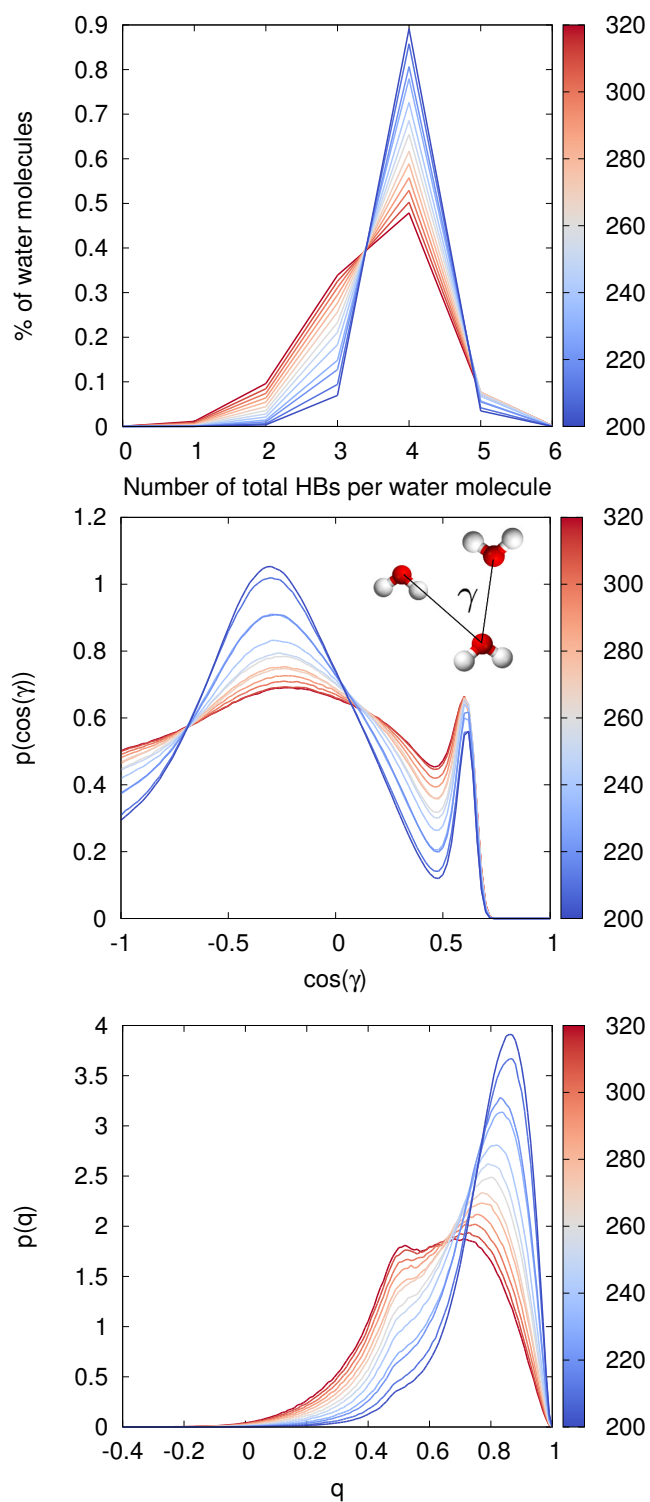


Figure 3.9: Top panel: fraction of water molecules with a given number of Hydrogen Bonds. Middle panel: distribution of $\cos(\gamma)$. Bottom panel: distribution of the Orientational Tetrahedral Order parameter. All the plots refer to SPC/E water model at $P = 1$ bar.

Chapter 4

Water-Trehalose solutions

This Chapter deals with the simulations of the water-trehalose mixtures [93]. Section 4.1 gives the details of the MD simulations. Several aspects of these two systems are analyzed, starting from the formation of clusters of trehalose in Section 4.2 and continuing with dynamical (Section 4.3 and 4.4) and structural quantities concerning water (Section 4.5).

4.1 Systems and simulation details

To study the influence of trehalose on the surrounding water, MD simulations of binary mixtures of water and trehalose have been performed on two systems with different concentration of the disaccharide:

- The first system is composed of 1498 water molecules and 54 trehalose molecules, corresponding to a concentration of 40.65 *wt%* in trehalose.
- The second system is composed of 1500 water molecules and 20 trehalose molecules, corresponding to a concentration of 20.21 *wt%* in trehalose.

The MD simulations were carried out using the GROMACS 4.5.5 package [94]. CHARMM force field was used for modeling the bonded and non-bonded interactions for sugar [83, 84] and SPC/E potential for water molecules [78], which is compatible with CHARMM [95].

To integrate the equations of motion the Verlet leapfrog algorithm with a time step of 1 fs was used. A cut-off of 1 nm was set for the non-bonded Van der Waals interactions. To handle the electrostatic interactions the Particle Mesh Ewald method was used. Boxes were cubic and Periodic Boundary conditions were used to minimize finite size effect. Systems were simulated at constant pressure $P = 1.013$ bar and at temperature spanning from

$T = 320$ K to $T = 200$ K. The Berendsen method [76] was used to control both the temperature and the pressure during the equilibration phase (NPT), whose duration ranged from 30 ns to 150 ns. For production runs the control of pressure and temperature with Berendsen was removed, using instead a mild coupling with temperature with Nosé-Hoover thermostat to avoid energy drift on the longest simulations. The length of the production runs ranged from 30 ns for high temperatures to 95 ns for low temperatures.

Details on the simulations length and total energy E_{tot} and total density ρ of the system after equilibration are reported in Table 4.1.

T [K]	t_{eq} [ns]	t_{prod} [ns]	Trehalose 40 wt%		Trehalose 20 wt%	
			E_{tot} [kJ/mol]	ρ [kg/m ³]	E_{tot} [kJ/mol]	ρ [kg/m ³]
320	30	30	-6482.7	1157.6	-37803.8	1065.9
310	30	30	-8330.7	1165.2	-39291.9	1072.5
300	30	35	-10196.5	1171.7	-40788.3	1078.5
290	30	35	-12035.4	1177.6	-42286.5	1084.2
280	30	35	-13900.5	1183.4	-43797.3	1089.3
270	30	40	-15703.7	1189.2	-45359.0	1093.2
260	40	40	-17646.1	1194.5	-46923.2	1096.1
250	40	45	-19497.3	1196.4	-48517.3	1098.7
240	40	45	-21380.5	1199.2	-50100.2	1100.1
230	50	55	-23253.7	1201.8	-51689.0	1100.3
220	50	65	-25177.8	1200.6	-53259.8	1100.1
210	60	65	-27011.9	1202.7	-54896.2	1097.1
205	80	75	-27899.7	1203.8	-55776.5	1094.5
200	150	95	-28831.9	1202.7	-56551.2	1091.2

Table 4.1: Summary of the simulated state points for the two water-trehalose mixtures. Details shown are the temperature T , the length of the equilibration runs t_{eq} , the length of the production runs t_{prod} , the total energy E_{tot} and total density ρ after equilibration.

Fig. 4.1 reports for selected temperatures the total energy as a function of the time for the system with a 40 wt% in trehalose. All the reported quantities reach a stable value with no drift, indicating a correct equilibration of the solution.

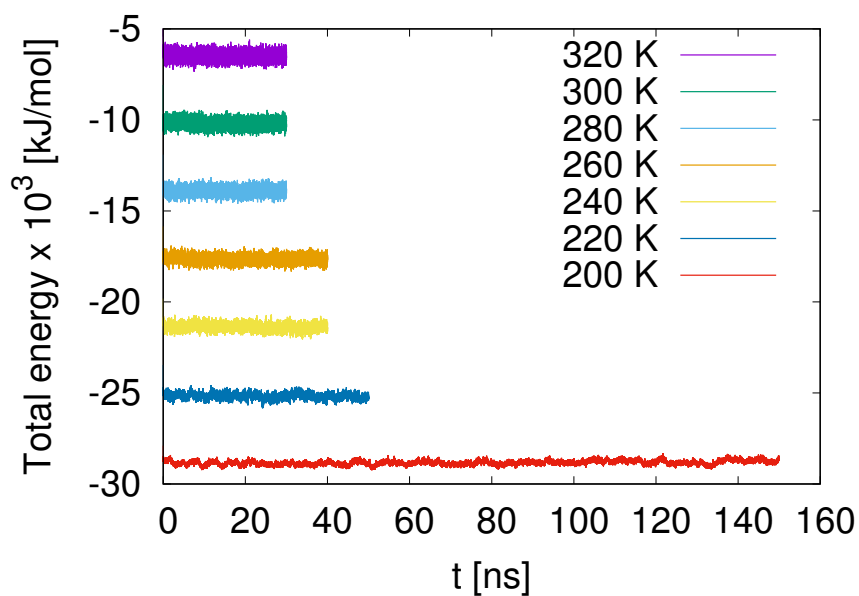


Figure 4.1: Total energy of the system with concentration of 40 *wt%* in trehalose as a function of the time during the equilibration phase for selected temperatures.

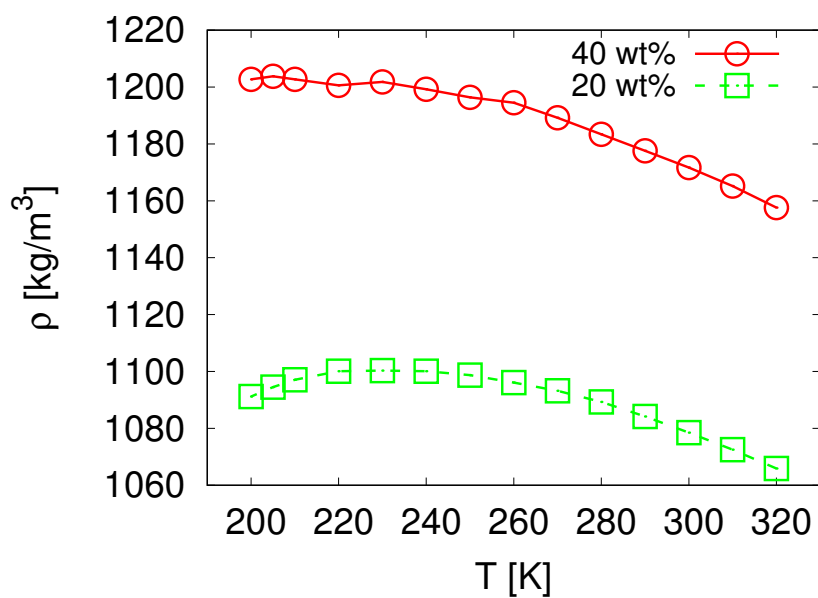


Figure 4.2: Total density of the two simulated systems after equilibration as function of temperature.

Fig. 4.2 reports the average total density of the two systems as a function of temperature. We observe in the 20.21 *wt%* a temperature of maximum density at around 230 K. This value is very close to the bulk water TMD value for $p = 1$ bar which is $T = 235$ K [96], therefore also in the solution the existence of the TMD as to be ascribed only to water. We observe a shift of the TMD towards lower temperature as the concentration of trehalose increases to 40.65 *wt%*. For this concentration the maximum is still not clearly detectable down to the lowest temperature investigated. As already found in literature the presence of a solute, trehalose in this case, produces a shift and sometimes also a shrink or enlargement of the water phase diagram, and typically this shift is toward lower temperatures [97,98], as also found here.

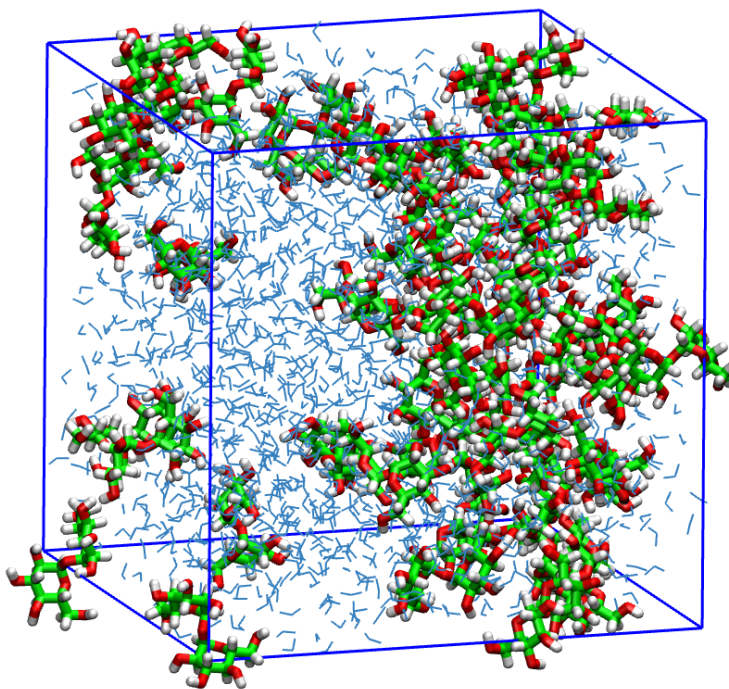


Figure 4.3: Snapshot of the configuration at $T = 230$ K after equilibration for the system with higher concentration. Carbon atoms of trehalose molecules are represented in green, oxygen atoms in red, hydrogen atoms in white. Water molecules are depicted as blue sticks.

As visual example of the state of one of the simulated systems, Fig. 4.3 reports a snapshot of the more concentrated solution after the equilibration run at $T = 230$ K. Trehalose molecules appear at this temperature already aggregated as they form an open cluster with a large surface exposed to water interaction. An analysis of the status of aggregation of trehalose molecules inside the two boxes investigated, as a function of temperature, is reported in the following Section.

Analysis of dynamical and statical properties of trehalose and water has been performed using the trajectories of the production runs. In analogy to what is done on proteins [99,100], a focus has been posed on hydration water, that is only water molecules inside a 0.6 nm thick layer around trehalose were taken into account. A water molecule is considered being in the hydration layer if the distance of its oxygen atom from the closest trehalose atom is less than 0.6 nm. As can be seen from Fig. 4.4 within this distance there are roughly two layer of water molecules, thus having a statistically significant population of water molecules with a strong interaction with the nearby trehalose molecules. The radial distribution functions calculated from the simulations approach the value of 1 at around $r = 2$ nm. Fig. 4.5 reports the average value of water molecules in the hydration layer (top panel) and the average water molecules in the hydration layer per trehalose molecule (bottom panel). In the more concentrated solution most of the water is also hydration water, with the highest fraction of water molecules in the hydration layer at the highest temperature investigated. As the solution is cooled the fraction of water molecules in the hydration layer decreases slightly. A similar trend is found in the more diluted solution, with an overall smaller value of the fraction of water molecules with respect to the other solution at all the temperatures. At $T = 200$ K only about 55% of the water molecules are in the hydration shell of trehalose in the solution with a 20 wt% concentration in trehalose. The average number of water molecules in the hydration shell divided by the number of the trehalose molecules in the solutions also depends on the temperature and on the specific concentration of the disaccharide. In particular the number of water molecules per trehalose molecules diminish with decreasing temperatures. This tendency is more marked in the less concentrated solution and this is consistent with the idea that with higher concentration of the solute the space available to water molecules decreases. The behaviour of these two quantities is connected both to the properties of water around the disaccharide molecules (formation of a more structured network) and to the properties of trehaloses to form aggregates. It is interesting to identify the role of the aggregation properties of different solutes in the change of the average number of hydration water molecules per solute

molecule. Some interesting results have been found comparing the expected trend predicted with a random close-to-contact condition (where the overlapping of hydration shell reduces the available space for water molecules) with simulations and experiments [101–103]. It should be noted that different values of the hydration number may be found depending on the definition of such a quantity and on the particular quantity under investigation [103]. Thus the effects of the trehalose-water interactions may extend further away from the limit distance chosen in this work and the recover of typical behaviour of bulk water may depends on which effect one is interested in (for example structural quantities or dynamical quantities).

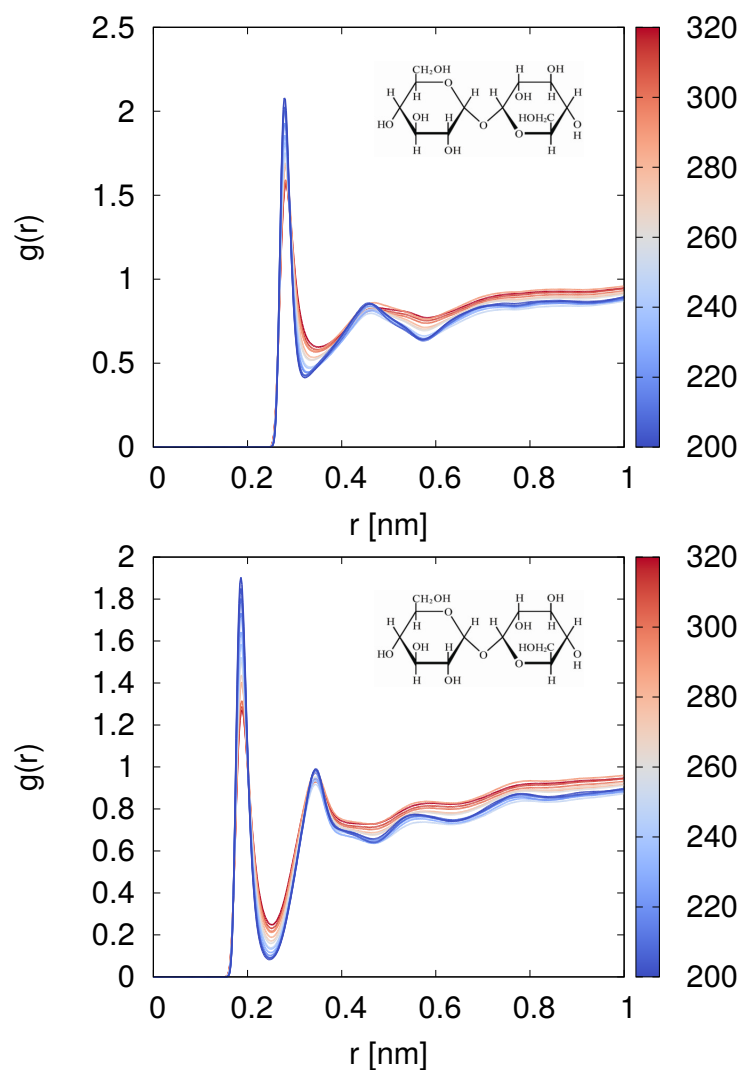


Figure 4.4: Radial distribution function $g(r)$ of oxygen (top panel) and hydrogen (bottom panel) atoms of the H-O group of the trehalose molecule and the oxygen atom of water. Within a distance of 0.6 nm from the reference atom, there are two peaks and two valleys in both the radial distribution function, indicating the presence of roughly two shell of water molecules. Depicted RDFs show a trend towards 1 and oscillations under this value. This is due to the fact that close to the surface of trehalose is not bulk.

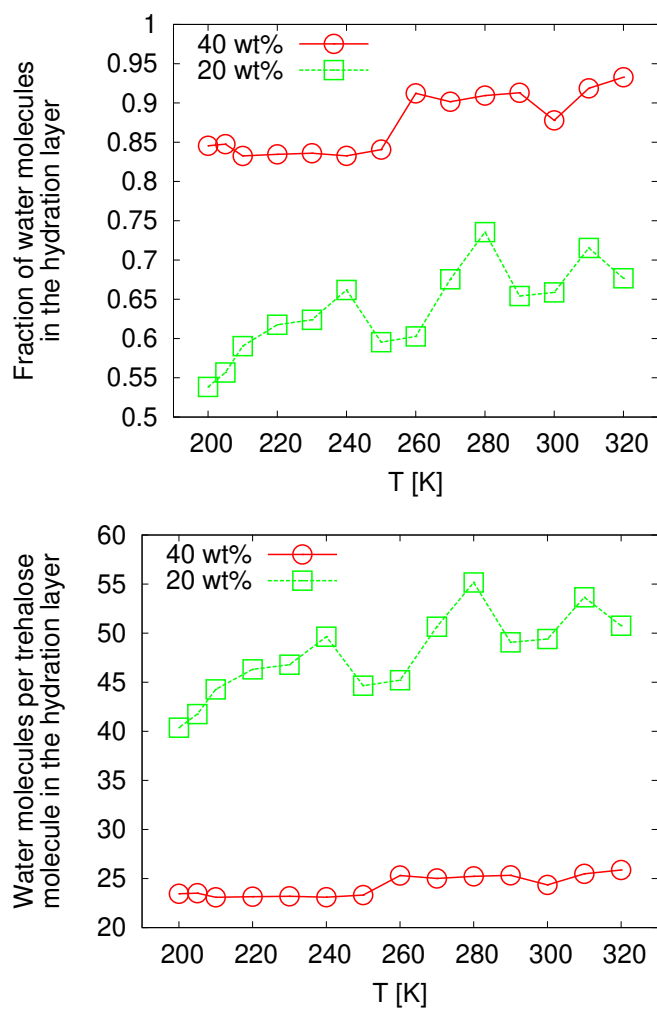


Figure 4.5: Top panel: average fraction of water molecules in the hydration layer as a function of the temperature for the two investigated solutions. Bottom panel: average value of water molecules in the hydration shell per trehalose molecule as a function of the temperature for the two investigated solutions.

4.2 Trehalose clusters

Simulations and experiments showed a tendency for trehalose molecules to cluster together. In this section an analysis of the aggregation state of trehalose molecules is carried out.

A trehalose molecule is considered in a cluster of molecules if it has at least one atom closer than 0.2 nm from any atom of another trehalose molecule in the cluster.

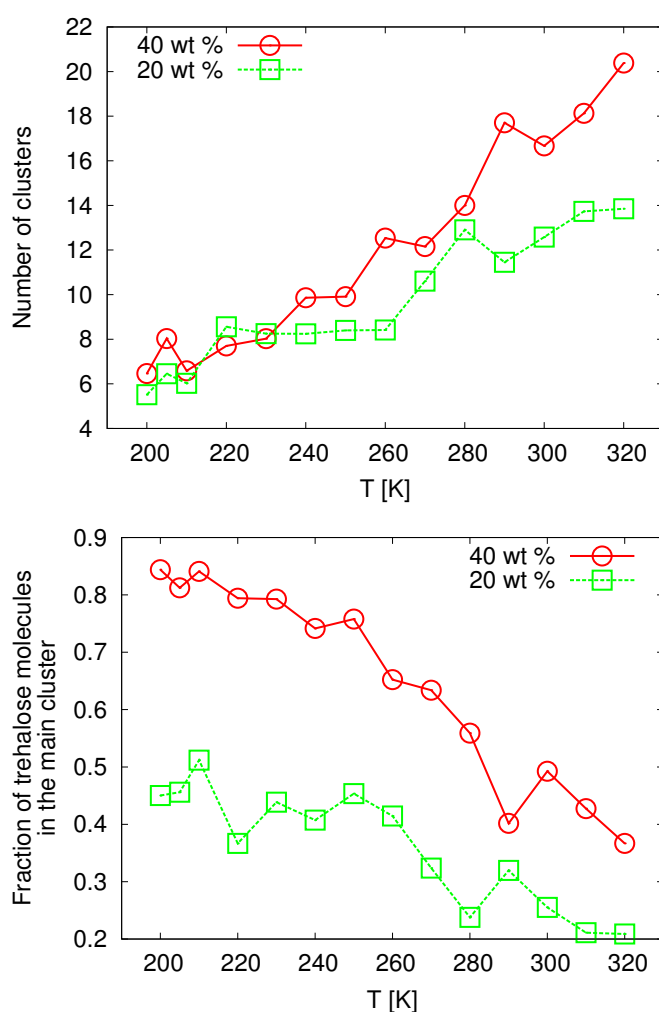


Figure 4.6: Top panel: average values of the number of clusters in the simulation boxes as function of the temperature. Bottom panel: average values of the fraction of trehalose molecules composing the largest cluster in the box as function of the temperature.

Fig. 4.6 reports the average values of the number of clusters and average values of the fraction of trehalose molecules composing the largest cluster as functions of the temperatures, respectively. At high temperature both the solutions are composed by a large number of relatively small clusters (less than half of trehalose molecules in the boxes). As the temperature was decreased, trehalose molecules tend to aggregate together and form less clusters. At low temperatures the number of clusters is of the same order in both systems but the fraction of molecules forming the biggest one differs, being smaller in the less concentrated system at all temperatures. In the more concentrated box, the largest cluster below 280 K is composed by more than half the number of trehalose molecules thus forming a macroaggregate. At the lowest temperatures simulated more than 80% of the trehalose molecules compose the largest cluster in the 40 *wt%* solution. On the contrary, the largest cluster in the more dilute solution is composed by less than half the trehalose molecules at all temperatures.

Fig. 4.7 shows the distribution of the clusters size as a function of temperature. It can be seen that aggregates of trehalose molecules form below 280 K in both systems. This is consistent with what experimentally observed in literature, being the disaccharide not soluble below that temperature [104]. At low temperatures in the more concentrated system a large, stable cluster can be observed with additional smaller clusters composed of few trehalose molecules (bimodal shape of the histogram). In the less concentrated system the histogram shape below 280 K is broader and trimodal, indicating the presence of many clusters of intermediate size.

Further analysis of the properties of the clusters, such as gelation, percolation threshold or fractal dimensions and extension of the biggest cluster will be useful to clarify the role played by the disaccharide in the binary water-trehalose solution and as a cryoprotectant in a multicomponent mixture.

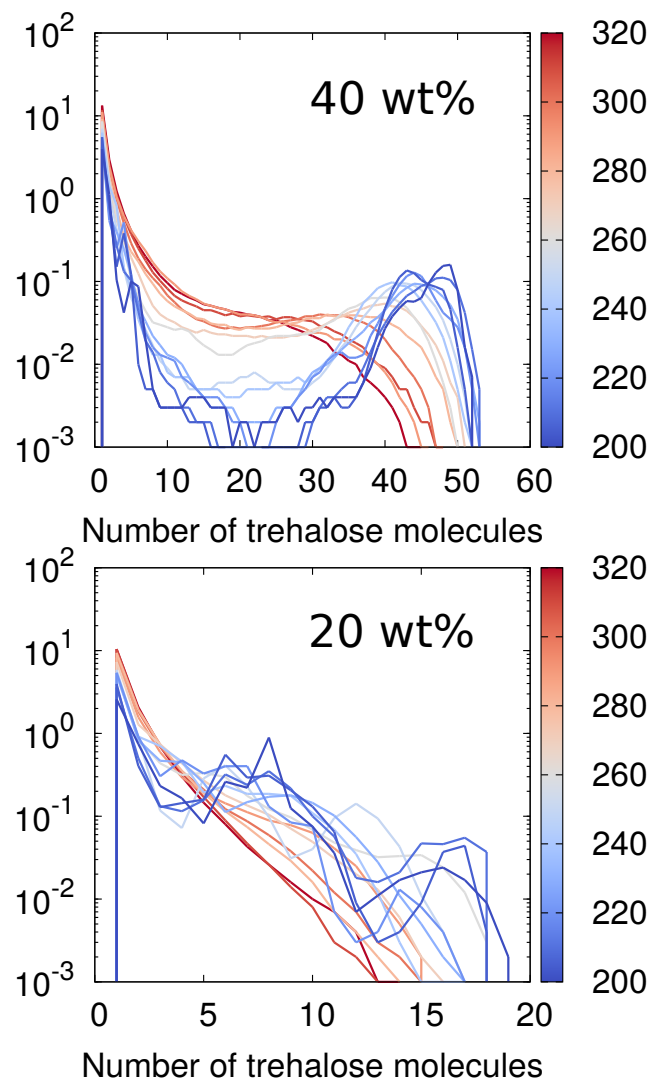


Figure 4.7: Distribution of the size of clusters in the simulated systems. Top panel for the solution with 40.65 wt% concentration in trehalose, containing 54 molecules of trehalose. Bottom panel for the solution with 20.21 wt% concentration in trehalose, containing 20 molecules of trehalose.

4.3 Translational dynamics

The translational dynamics of hydration water has been characterized upon cooling by calculating the oxygen Self Intermediate Scattering Function (SISF). This correlation function can provide valuable information to understand the relaxation mechanism in supercooled liquids. SISF, as already stated in Chapter 3, can be computed via the formula

$$F_S(\mathbf{q}, t) = \left\langle \frac{1}{N} \sum_{i=1}^N e^{i\mathbf{q} \cdot (\mathbf{r}_i(t) - \mathbf{r}_i(0))} \right\rangle$$

All the SISFs reported in this work are calculated at transferred wave-vector $q = |\mathbf{q}| = 2.25 \text{ \AA}^{-1}$, i.e. the first peak of the oxygen-oxygen structure factor of water, where the features of the slow dynamics of supercooled water are best evident. This value of the wave-vector corresponds to the length scale of the cage formed by the first shell of nearest neighbours molecules [6]. In order to characterize the properties of hydration water, SISFs are calculated only for the time interval in which a water molecule (in particular its oxygen atom) resides in a 0.6 nm shell around trehalose molecules.

Fig. 4.8 reports the oxygen-oxygen SISFs of hydration water for the system with a 40.65 wt% concentration in trehalose for all the temperatures simulated. The two steps relaxation typical of glass former liquids are evident and this feature is greatly enhanced upon cooling, with the correlators stretching over a time scale of many order of magnitude. The initial, short time, Gaussian relaxation is common to all the correlators, with small changes upon cooling. Starting from circa 0.3 ps the second relaxation takes place, with a characteristic time that is strongly influenced by the cooling of the solution. From approximately 220 K a plateau region starts to appear and is clearly visible for lower temperatures, with height increasing upon lowering the temperature.

Correlators for hydration water in the 320 K - 260 K temperature range decay to zero within 1 ns, while for lowest temperatures, $T < 250$ K, correlators don't decay to zero even on time scale of many nanoseconds.

Differences in the time scale of the decay of hydration water correlators are best evident if compared with the ones of bulk water. In the inset of Fig. 4.8 comparison between the SISF of bulk water (dashed lines) and hydration water (continuous lines) is reported for temperature of 300 K and 250 K. SISFs calculated starting from trajectories of oxygen atoms of hydration water present a much slower dynamics, with stretched correlators and

long tails, while the first relaxation is similar in correlators for bulk water and hydration water that are calculated at the same temperature.

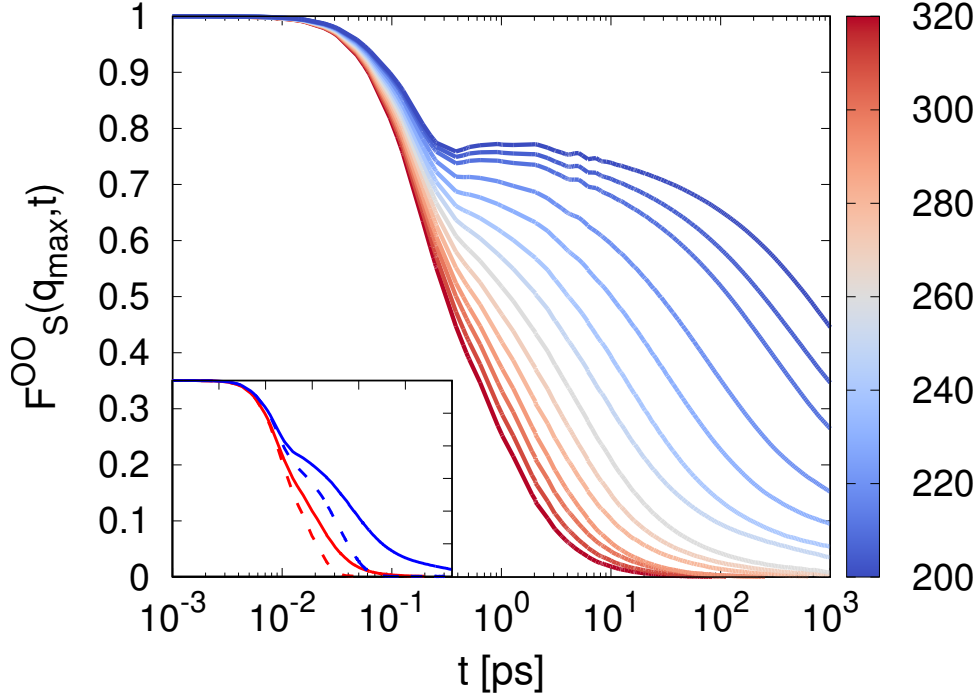


Figure 4.8: Oxygen-oxygen SISF $F_S^{OO}(q_{max}, t)$ for water molecules in the hydration layer 0.6 nm thick from trehalose molecules in the solution with 40.65 wt% concentration. Curves for all simulated temperatures are displayed. The inset reports the SISFs for hydration water (continuous lines) and bulk water (dashed lines) for $T = 300$ K (red) and $T = 250$ K (blue). Correlators are calculated at $q_{max} = 2.25 \text{ \AA}^{-1}$.

To further investigate to which extent the nearby presence of trehalose molecules change the dynamics of surrounding water, Fig. 4.9 reports the Self Intermediate Scattering Functions for bulk water (black lines), hydration water of the 20.21 wt% concentration in trehalose solution (green lines) and hydration water of the 40.65 wt% concentration in trehalose solution (red lines). The highest and the lowest simulated temperature are reported, respectively $T = 320$ K and $T = 200$ K. Correlators of bulk water are faster than hydration water ones. Correlators for the more concentrated solution are slower than the ones for the more diluted simulation. It is interesting to note that, as already seen in the inset of Fig. 4.8, the characteristic

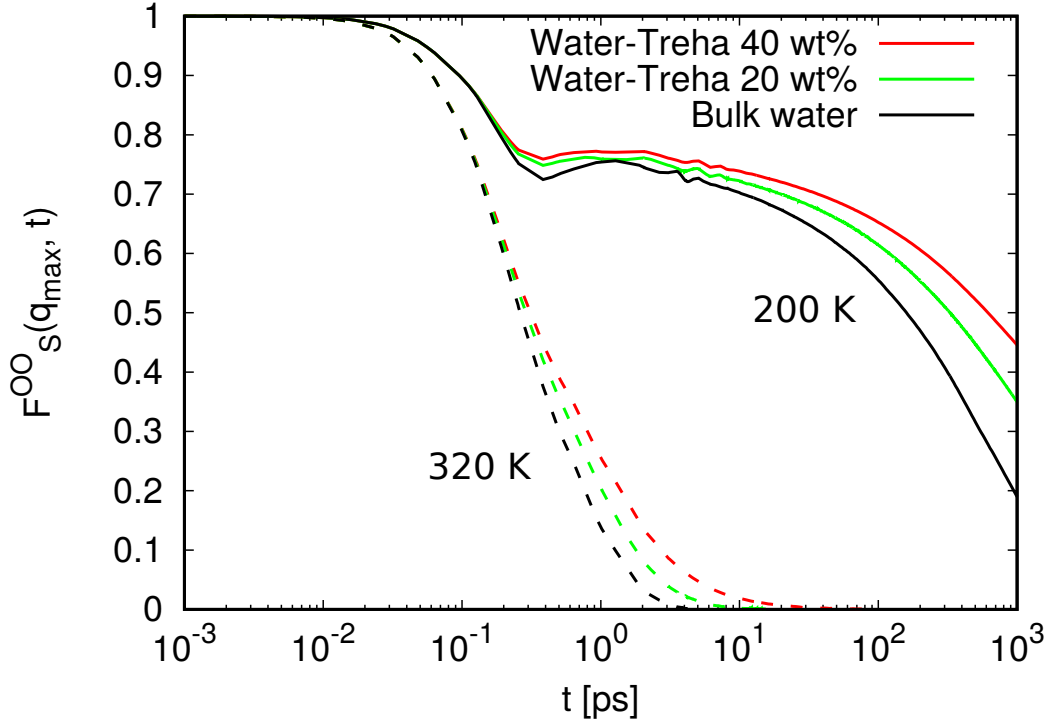


Figure 4.9: Oxygen-oxygen SISF $F_S^{OO}(q_{max}, t)$ for water molecules in the hydration layer 0.6 nm thick from trehalose molecules in the solution with 40.65 wt% concentration (red lines) and with 20.21 wt% concentration (green lines). Curves the highest and the lowest simulated temperature are displayed (320 K and 200 K respectively). SISFs for bulk water are reported as black lines for reference. Correlators are calculated at $q_{max} = 2.25 \text{ \AA}^{-1}$.

relaxation time of the Gaussian decay, τ_{short} , doesn't seem to be affected by the presence of the trehalose, independently of the concentration of the latter. In fact curves almost perfectly overlap till $t \sim 0.2$ ps. Moreover the plateau height is roughly the same for both the solutions with trehalose. The boson peak, discussed in 3.8 for bulk water, is visible also in the correlators of hydration water and starts to appear between 230 K and 220 K. The first minimum is at the same position where it is in bulk water whereas the first maximum is shifted to shorter time and it is less pronounced with respect to what seen in bulk water. Boson peak in hydration water has been observed in experiments and numerical simulations and changes in its features can be connected with the different rigidity of the soluted molecule [105–107]. Oscillations due to finite size effects are shifted to longer time and are reduced in amplitude, consistently with the larger size of the simulation boxes of the

two water-trehalose solutions. Deviations from the bulk water behaviour are clear in the long time tails and increase with increasing concentration of the disaccharide.

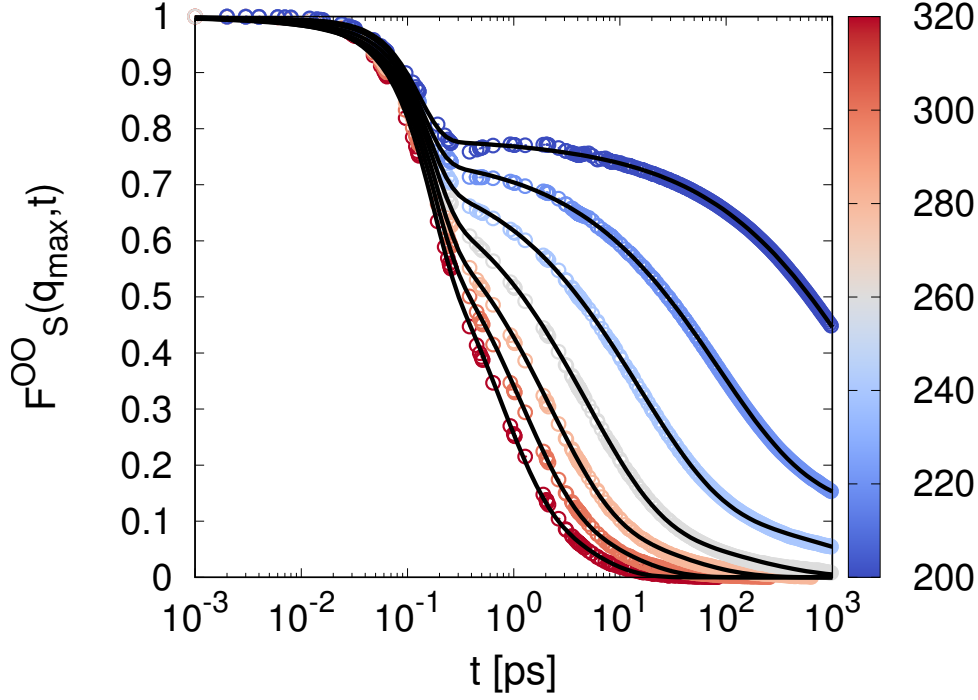


Figure 4.10: Oxygen-oxygen SISF $F_S^{OO}(q_{max}, t)$ for water molecules in the hydration layer 0.6 nm thick from trehalose molecules in the solution with 40.65 wt% concentration. Curves shown are for selected temperatures. Superimposed black lines are best fit with Eq. 4.2.

Following MCT description of glassy dynamics, Gallo *et al.* [7] and Sciortino *et al.* [8] modelled the relaxation of the SISFs for bulk water with the functional form:

$$F(q, t) = (1 - f_\alpha)e^{-(t/\tau_{short})^2} + f_\alpha e^{-(t/\tau_\alpha)^{\beta\alpha}} \quad (4.1)$$

that is able to account for both the initial short time decay with the Gaussian term, and the subsequent α -relaxation with the stretched exponential. Unfortunately it fails to describe the density auto-correlators of hydration water down to their complete decay to zero, due to the new long time, slow decaying tails.

Studying solutions of water and disaccharides with MD simulations, Magno and Gallo [11] proposed to modify Eq. 4.1 by adding a new stretched exponential with a characteristic relaxation time, τ_{long} , and stretching exponent, β_{long} , to account for the long relaxation:

$$F(q, t) = (1 - f_\alpha - f_{long})e^{-(t/\tau_{short})^2} + f_\alpha e^{-(t/\tau_\alpha)^{\beta_\alpha}} + f_{long} e^{-(t/\tau_{long})^{\beta_{long}}}. \quad (4.2)$$

Results of the fitting procedure of the oxygen-oxygen SISFs of hydration water for the more concentrated solution are reported in Fig. 4.10 as continuous black lines. Results are remarkably good, being the new functional form able to follow the correlators through their whole decay.

Parameters resulting from the fitting procedure for SISFs of hydration water of both the water-trehalose solutions with Eq. 4.2 are plotted in Fig. 4.11 and listed in Table 4.2.

In previous experimental [108, 109] and simulations [11, 12] works, analysis of the translational dynamics of water in biological mixtures were performed without being able to distinguish between hydration water and water molecules outside the hydration layer. With the separation of these two water populations it is possible to clearly attribute to hydration water the found feature of the long tails in the correlators. Dynamics of hydration water is fundamentally different from dynamics of bulk water. It presents two distinct slow relaxations, the α -relaxation and the *long*-relaxation and not a single structural α -relaxation with a longer characteristic time τ_α .

The structural relaxation time τ_α shows no significative difference between the two solutions with different concentration of the disaccharide, being of the same order of magnitude at all the simulated temperature. By contrast values of τ_{long} strongly differ between the two systems with the value of the more concentrated solution at $T = 200$ K two order of magnitude greater than the one of the other solution. Their temperature behaviour start to depart one from the other at around $T = 280$ K, with a steep increase of the long relaxation time of the 40.65 wt% concentrated solution.

The stretching exponents of both the relaxation processes decrease upon cooling in both the systems, with the values of the 20.21 wt% solution being always greater than the ones of the other solution, $\beta^{20\text{wt}\%} > \beta^{40\text{wt}\%}$. β_α starts around 1.0 - 0.95 at 320 K and goes down to a plateau value of about 0.6 at 200 K for both the solutions. β_{long} starts around 0.95 for the 20.21 wt% solution and 0.8 for the 40.65 wt% solution and reaches a final value of about 0.25 at the lowest temperature independently of the concentration of the solute. The result is that the dynamics in the solution with more trehalose is

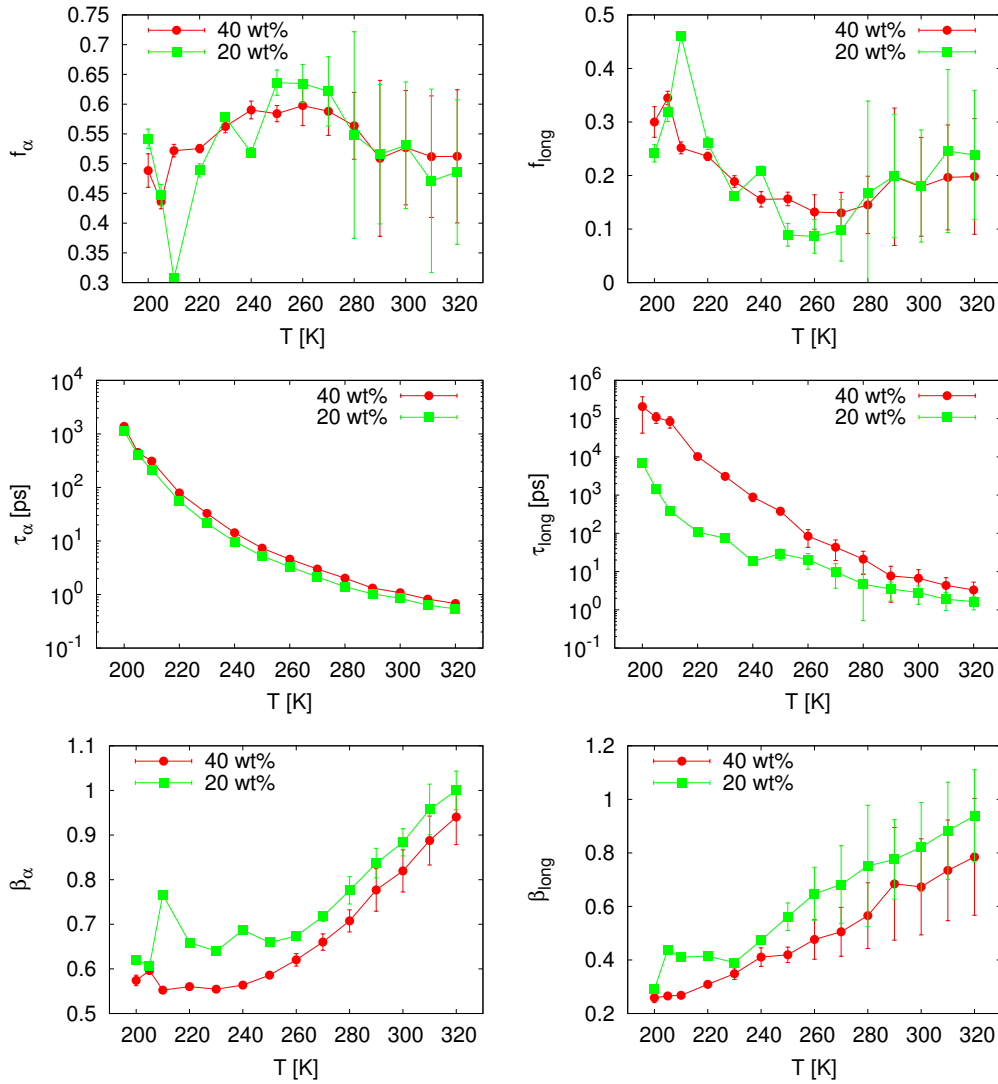


Figure 4.11: Results of the fitting procedures via Eq. 4.2 of the oxygen-oxygen SISFs of hydration water for both systems with 40.65 wt% (in red) and 20.21 wt% (in green) concentration in trehalose. Left panels refer to α -relaxation, right panels to long-relaxation.

slower and more stretched over the analyzed time scale.

Errors on the estimated parameters are larger at high temperature and generally decrease upon cooling, this is due to the fact that at higher temperatures, where the α -relaxation and the *long*-relaxation times are comparable in magnitude, it is difficult to fully disentangle contributions coming from

T [K]	System	t_{short} [ps]	f_{α}	τ_{α} [ps]	β_{alpha}	f_{long}	τ_{long} [ps]	β_{long}
320	40 wt%	0.16	0.51	0.68	0.94	0.20	3.30	0.78
	20 wt%	0.17	0.49	0.54	1.00	0.24	1.64	0.94
310	40 wt%	0.17	0.51	0.82	0.89	0.20	4.35	0.73
	20 wt%	0.17	0.47	0.63	0.96	0.25	1.89	0.88
300	40 wt%	0.17	0.53	1.08	0.82	0.18	6.70	0.67
	20 wt%	0.18	0.53	0.85	0.88	0.18	2.83	0.82
290	40 wt%	0.17	0.51	1.32	0.78	0.20	7.70	0.68
	20 wt%	0.18	0.52	1.03	0.84	0.20	3.50	0.78
280	40 wt%	0.18	0.56	2.02	0.71	0.15	21.20	0.57
	20 wt%	0.18	0.55	1.40	0.78	0.17	4.67	0.75
270	40 wt%	0.18	0.59	2.99	0.66	0.13	43.31	0.51
	20 wt%	0.18	0.62	2.13	0.72	0.10	9.87	0.68
260	40 wt%	0.17	0.60	4.57	0.62	0.13	84.12	0.48
	20 wt%	0.18	0.63	3.31	0.67	0.09	20.58	0.65
250	40 wt%	0.16	0.58	7.35	0.59	0.16	379.90	0.42
	20 wt%	0.17	0.64	5.23	0.66	0.09	29.34	0.56
240	40 wt%	0.16	0.59	14.27	0.56	0.16	888.70	0.41
	20 wt%	0.17	0.52	9.76	0.69	0.21	18.46	0.47
230	40 wt%	0.15	0.56	37.72	0.55	0.19	3081.00	0.35
	20 wt%	0.16	0.58	21.22	0.64	0.16	74.38	0.39
220	40 wt%	0.14	0.53	78.84	0.56	0.24	10160	0.31
	20 wt%	0.15	0.49	55.44	0.66	0.26	108.40	0.41
210	40 wt%	0.14	0.52	310.30	0.55	0.25	83910	0.27
	20 wt%	0.14	0.31	213.10	0.77	0.46	391.40	0.41
205	40 wt%	0.13	0.44	450.00	0.60	0.34	108700	0.27
	20 wt%	0.14	0.45	407.50	0.61	0.32	1445.00	0.44
200	40 wt%	0.13	0.49	1384.00	0.57	0.30	206700	0.26
	20 wt%	0.13	0.54	1123.00	0.62	0.24	6949.00	0.29

Table 4.2: List of the fitting parameters via Eq. 4.2 of the oxygen-oxygen SISOs of hydration water for both systems with 40.65 wt% and 20.21 wt% concentration in trehalose.

the two processes. It should be also noted that the correlators for the lowest temperatures simulated don't decay to zero in the time spanned by the simulations and that the values of τ_{long} resulting from the fitting procedure exceed the length of the production runs. Moreover the long tails of the slow correlators suffer from low statistics due to the fact that it is difficult to find an adequate amount of water molecules that reside in the hydration shell for

very long time. It is thus quite difficult to estimate the *long*-relaxation time very accurately.

A test of the range of validity of the MCT predictions is provided by the time-temperature superposition principle (see Chapter 2). According to MCT, the final part of the β -relaxation of a correlator is described by the von Schweidler law

$$\Phi_q(t/\tau) = f_q - h_q \cdot (t/\tau)^b \quad (4.3)$$

where f_q is the ergodicity factor, h_q is the amplitude and b is the von Schweidler exponent. The time-temperature superposition principle predicts that correlators plotted against the rescaled time t/τ , with τ the structural relaxation time, collapse into a master curve Φ . Fig. 4.12 reports the SISFs of the hydration water plotted against the time rescaled by τ_α .

SISFs calculated at intermediate temperature ($220 \text{ K} < T < 280 \text{ K}$) collapse pretty well on a master curve between approximately 0.003 and 0.3 in unit of the rescaled time. Fits with a von Schweidler law Eq. (4.3) yield values of the parameters (listed in Table 4.3) that are similar to what is found for bulk water [8, 68]. For time greater than 0.4 in rescaled time unit, SISFs start to depart from the master curve. This is due to the presence of the new *long* time relaxation process not predicted by MCT. This deviation is more pronounced in the 40.65 *wt%* concentrated solution (left panel of Fig. 4.12) where the presence of more trehalose enhances the slowing down of the dynamics upon cooling as already seen from the parameters of the fits with Eq. (4.2) (see Table 4.2). Correlators calculated at high temperatures ($T > 280 \text{ K}$) collapse into the master curve in a narrower time window. These temperatures are at the limit of the range of applicability of MCT. Correlators calculated at low temperature ($220 \text{ K} < T$) fail to collapse into the master curve, because of the *long* slow relaxation at longer time, and because of the onset of activated processes that drive the dynamics on a shorter time scale.

System	f_q	h_q	b
40 <i>wt%</i>	0.740 ± 0.008	0.455 ± 0.009	0.51 ± 0.04
20 <i>wt%</i>	0.747 ± 0.005	0.488 ± 0.002	0.48 ± 0.01

Table 4.3: List of the fitting parameters via Eq. (4.3) of the rescaled oxygen-oxygen SISFs of hydration water reported in Fig. 4.12 .

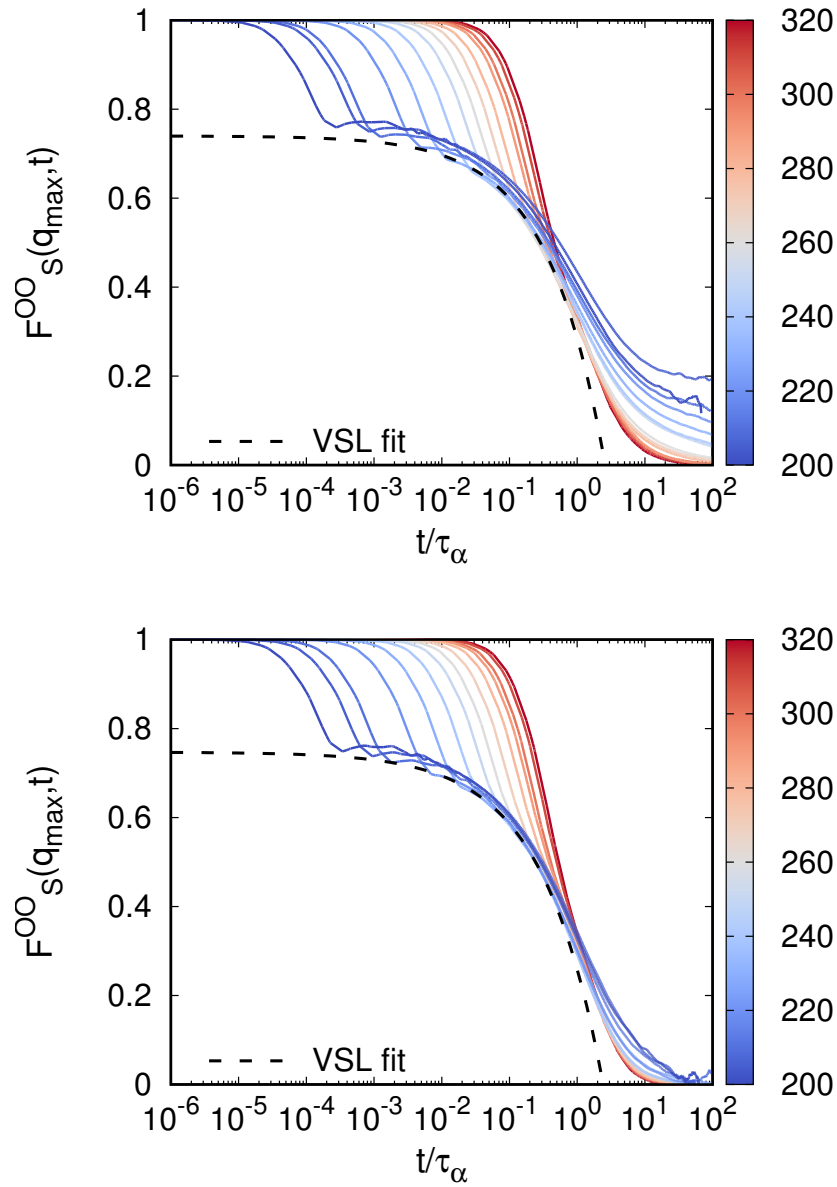


Figure 4.12: Oxygen-oxygen SISFs vs scaled time t/τ_{α} for both systems with 40.65 wt% (left panel) and 20.21 wt% (right panel) concentration in trehalose. Superimposed dashed black lines are best fits with von Schweidler law, see Eq. (4.3)

4.3.1 Relaxation times

α -relaxation time

Fig. 4.13 reports the α -relaxation times extracted from the fit of the SISFs to Eq. (4.2). Top panel of Fig. 4.13 shows the fit of the α -relaxation time for both hydration water of the solution with 40.65 *wt%* concentration in trehalose and bulk water, bottom panel shows the fit of the α -relaxation time for the hydration water of the solution with 20.21 *wt%* concentration in trehalose. The fragile region is characterized by a power law

$$\tau \propto (T - T_{MCT})^{-\gamma} \quad (4.4)$$

where T_{MCT} is the MCT temperature where all the cages are frozen and diffusion happens below that temperature only through activated processes, and the strong region is characterized by an Arrhenius law

$$\tau \propto e^{-E_A/(k_B T)} \quad (4.5)$$

where E_A is the activation energy.

Results from fitting procedure are reported in Table 4.4.

System	T_{MCT} [K]	γ	E_A [kJ/mol]	T_{FSC} [K]
Water-Treha 40 <i>wt%</i>	202.9	2.7	42.3	230
Water-Treha 20 <i>wt%</i>	200.8	2.7	47.8	225
Bulk water	193.8	2.74	63.4	210

Table 4.4: MCT temperature T_{MCT} , γ exponent, activation energy E_A and FSC temperature T_{FSC} for the α -relaxation of hydration water of the water-disaccharides solutions and of bulk water.

The critical temperature at which MCT predicts a transition to an arrested non-ergodic phase, T_{MCT} , is slightly shifted towards higher values by the addition to the solution of trehalose molecules, whereas the exponent γ is unaltered by the composition of the water-disaccharide mixture under investigation.

Similar to what found for protein hydration water [99, 110], also the α -relaxation of trehalose hydration water presents a Fragile to Strong Crossover (FSC). From the top panel of Fig. 4.13 and from the values reported in Table 4.4, it appears clear that along the same isobar bulk water and trehalose hydration water have very similar values for the fitting parameters and the FSC temperature. The FSC happens at $T = 230$ K in the

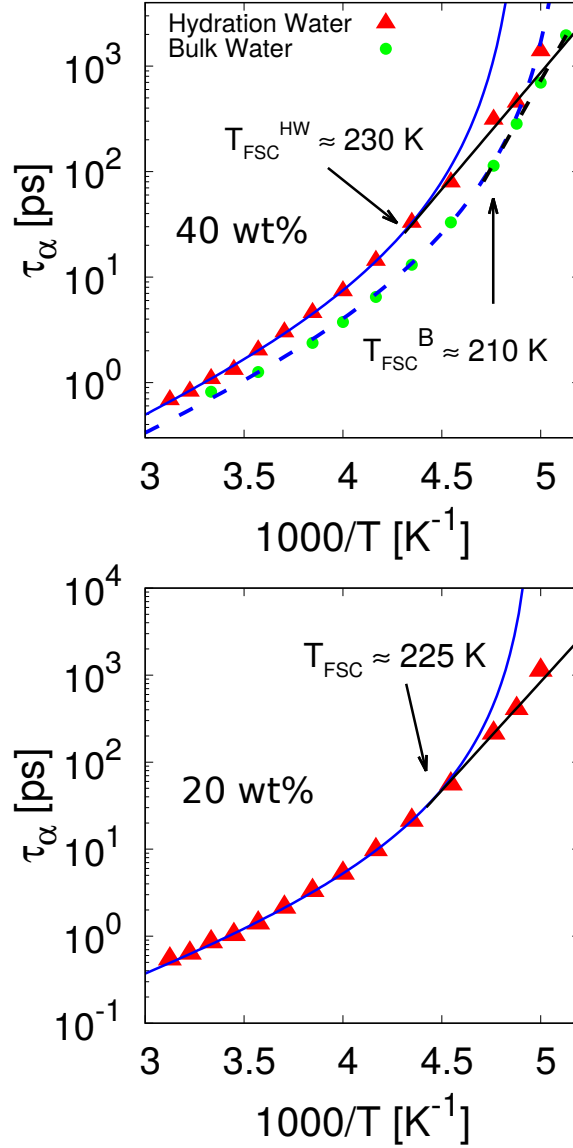


Figure 4.13: Arrhenius plot of α -relaxation time extracted by the fit procedure via Eq. (4.2) of the SISFs of the system with 40.65 wt% concentration in trehalose (top panel) and 20.21 wt% concentration in trehalose (bottom panel). Top panel also reports the α -relaxation time for Bulk Water as a reference. Blue lines are the best fit to the fragile region characterized by a power law behaviour, as predicted by MCT, $\tau \propto (T - T_{\text{MCT}})^{-\gamma}$. Black lines are the best fit of the strong region with the Arrhenius law.

40.65 wt% solutions and at $T = 225$ K in the 20.21 wt% solution. A temperature close to the ones where it was found the same crossover in bulk wa-

ter [68, 70, 71, 111–113], confined water [72, 73, 114], aqueous solutions [115] and hydration water [49, 54, 99, 110], thus confirming that the glassy behaviour of water is very ubiquitous and it is present also on a thin layer of water molecules such hydration water. Similarly to what found for protein hydration water [99], the slow down induced by trehalose on hydration water for the α relaxation process is not very substantial and there is an increase of the FSC temperature of circa 15–20 K for the water-trehalose solutions with respect to the bulk water. The shift of the FSC temperature is consistent with the shift of MCT temperature towards higher value.

Below the crossover temperature activated processes start to drive the dynamics and the behaviour of τ_α deviates from the power law predicted by MCT. Activation energy resulting from the fits decreases with increasing concentration of trehalose with a major jump between pure water and hydration water: in bulk water it is 63.4 kJ/mol, in the more diluted solution it is 47.8 kJ/mol and in the more concentrated one it is 42.3 kJ/mol. It has been shown [113] that in pure water hopping phenomena are more pronounced when water is more structured and less mobile. Moreover it has been shown that oligosaccharides induce a structuring effect on water molecules [116]. This may suggest that the structure of water and the activation energy are connected and hopping is favoured because of the smaller energy barrier.

Long-relaxation time

Fig. 4.14 reports an Arrhenius plot with values of the *long*-relaxation characteristic time τ_{long} (top panel for the more concentrated solution, bottom panel for the other one). It shows a strong behaviour with two crossovers upon cooling and its evolution with temperature can be modeled with an Arrhenius law (see Eq. (4.5)). In the solution with 40.65 wt% concentration in trehalose, the activation energies are, starting from the fit at higher temperatures: $E_A = 23.2$ KJ/mol, $E_A = 41.5$ KJ/mol, $E_A = 53.3$ KJ/mol. The two crossover temperatures from strong to strong are $T_{SS1} \approx 280$ K and $T_{SS2} \approx 255$ K. At higher temperatures it shows a first change of slope between 280 K and 290 K. This crossover appears to be connected to the fact that at around 280 K trehalose forms a large cluster in the solution. For temperatures lower than 280 K trehalose therefore behaves like a flexible macromolecule with respect to the interaction that it has with hydration water. At lower temperatures we observe another crossover with a change of slope around 250 K and 260 K. This crossover is remarkably similar to what has been found recently by molecular dynamics simulation in the long relaxation time of hydration water around a protein [99] and to what found in water close to colloidal microgels [117]. Therefore this feature appears

due to the interaction of water with flexible macromolecules, not necessarily having a biological function. The long time rearrangements of water molecules dragged by cluster of trehalose molecules cause the onset of the long-relaxation of hydration water. It is interesting to note that α -relaxation and *long*-relaxation happen at two different time scale, well separated especially at lower temperature. Thus the dynamics of bulk water is retained in hydration water, albeit with a shift of temperatures at higher values, because water network can structurally relax on a time scale given by τ_α , that is short compared to the typical time scale of the fluctuations of the macroaggregate composed by trehalose molecules. Only on longer time the fluctuations of the clusters drag in its motion the nearby water molecules.

Bottom panel of Fig. 4.14 reports the values of τ_{long} for the less concentrated solution. Here the activation energies are, starting from the fit at higher temperatures: $E_A = 20.2$ KJ/mol, $E_A = 19.2$ KJ/mol, $E_A = 95.9$ KJ/mol. The two crossover temperatures from strong to strong are $T_{SS1} \approx 275$ K and $T_{SS2} \approx 215$ K.

The first transition at $T_{SS1} \approx 275$ K consists in a jump of the value of the long relaxation time τ_{long} , while the value of the activation energy is slightly lower. This transition is near the clustering temperature of trehalose molecules observed in the solution and thus can be connected to this phenomenon. The second strong-to-strong crossover happens at much lower temperature, at around 215 K, and the increase in the activation energy is much more steep. The temperature of this crossover is lower than the one observed in the more concentrated solution and the change in the slope is much more pronounced. Due to this fact the argument that connect this crossover with the fluctuations of the aggregate of trehaloses is more weak. In general in this second, more diluted solution, analysis of the *long*-relaxation process is more difficult and the results less clear. Moreover the fact that, as seen in the section regarding the clusters of trehalose, multiple clusters of different size are observed in the solution leads to a more noisy signal and poor statistics. A more accurate analysis is ongoing in order to gain better statistics and clarify the phenomenology.

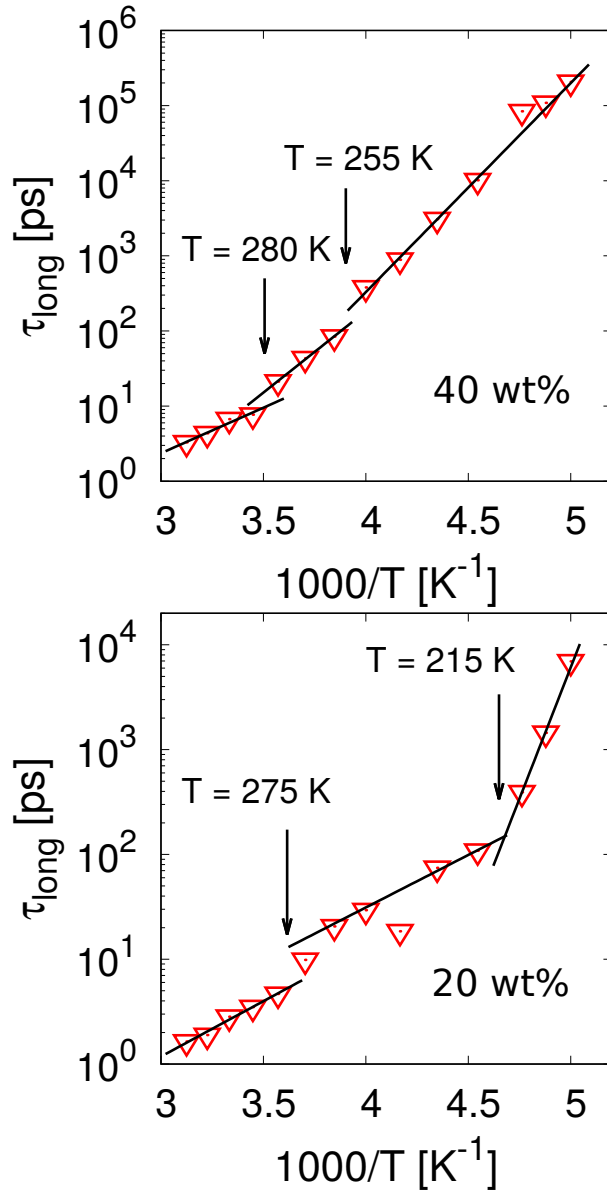


Figure 4.14: Arrhenius plot of the long-relaxation time extracted by the fit procedure via Eq. (4.2) of the SISFs of the system with 40.65 wt% concentration in trehalose (top panel) and 20.21 wt% concentration in trehalose (bottom panel). Black lines are best fits via Arrhenius laws.

4.4 The Dynamical Transition

To further analyze the dynamical features of hydration water and trehalose molecules the Mean Square Displacement (MSD) of selected atoms has been calculated for both systems (see Eq. (3.66)). Fig. 4.15 reports the MSD for the oxygen atoms of hydration water of the solution with 40.65 *wt%* concentration in trehalose for all temperatures. Similar to the SISF also the MSD shows an initial ballistic regime, followed by a plateau corresponding to the rattling of the particle in the cage. For longer times the MSD shows a sub-

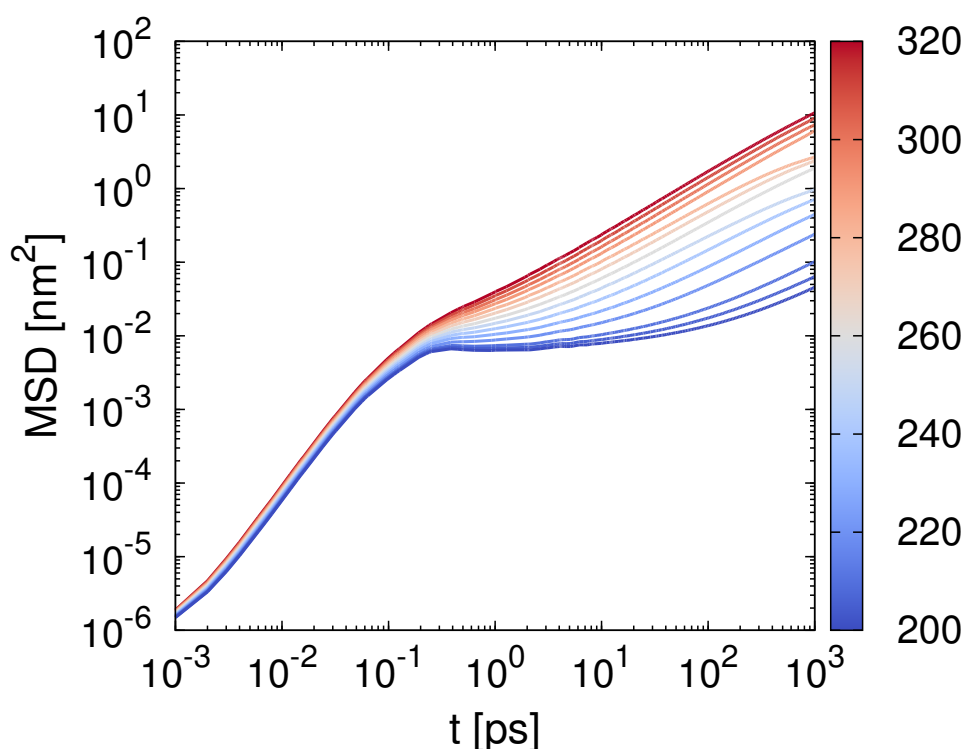


Figure 4.15: Mean Square Displacement for oxygen atoms of hydration water of the solution with 40.65 *wt%* concentration in trehalose for all temperatures.

diffusive behaviour even for the longest simulation times. This is due to the fact that the water molecules in the hydration layer don't recover the Brownian regime at least in the time scale of the simulations analyzed and this is related to the presence of the third relaxation process, that is extremely long, and to the presence of the nearby trehalose molecules that hinder the motion of water molecules in the hydration layer.

Fig. 4.16 reports the MSDs of the oxygen atoms of hydration water for

both the water-trehalose solutions at the highest and lowest temperature simulated, $T = 320$ K and $T = 200$ K respectively.

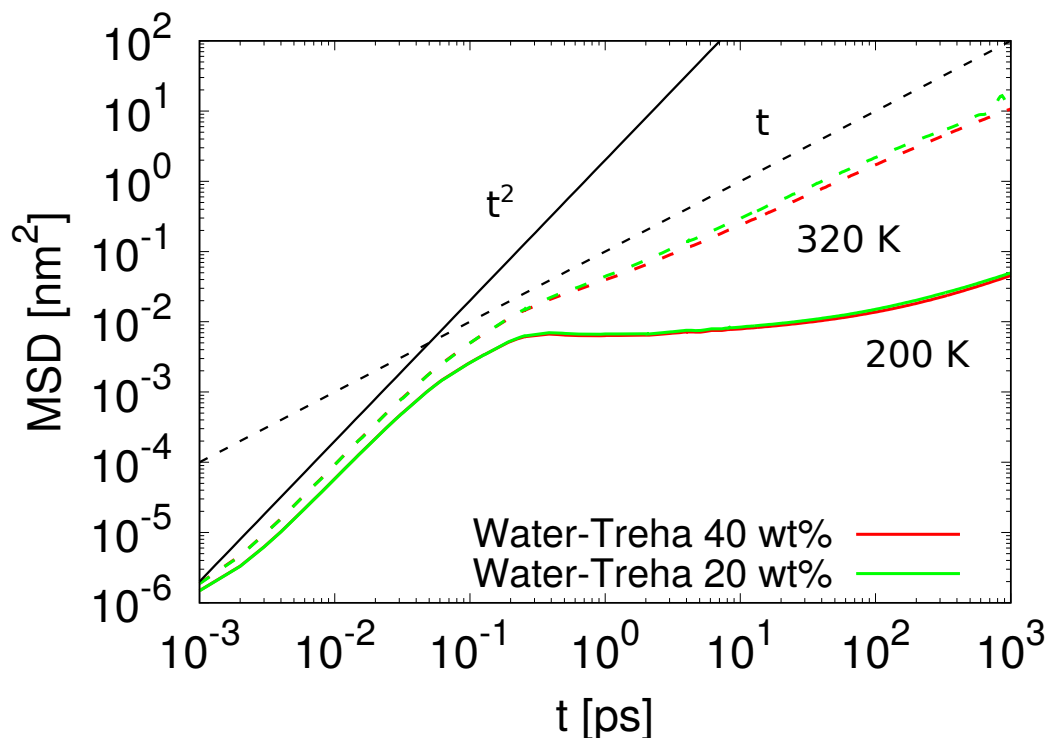


Figure 4.16: Mean Square Displacement for oxygen atoms of hydration water of the solution with 40.65 *wt%* concentration in trehalose and 20.21 *wt%* concentration in trehalose for the highest and lowest temperature simulated. Continuous and dashed black lines are guides for eyes which evidence the short time ballistic and long time diffusive behavior of the MSD.

Differences are small in log-log scale and more accentuated at long time, with the MSDs of the hydration water slightly higher in the more diluted solution. The plateau region due to the cage effect starts at around 0.3 ps in perfect agreement to what seen in the SISFs (see Fig. 4.9). Black continuous and dashed lines report the expected behaviour of the MSD for short and long times, that is ballistic diffusion and Brownian diffusion. At short time (before the plateau region) both the MSDs behave ballistically, while at long time the Mean Square Displacement is sub-diffusive up to the simulated time length. Anomalous diffusion as been observed in the motion of water molecules at the interface with different biomolecules and several models have been proposed to explain it [118, 119]. In this case subdiffusivity can probably be due to the interactions of water molecules with trehaloses through

hydrogen bonds (as for example bridging water molecules between trehalose molecules) or steric hindrance that prevents the water molecules from moving freely. It should be stressed that the quantities presented here are averaged over all the molecules in the hydration shell. Such molecules come from different populations, as for example water molecules that are near or distant from hydrophilic sites or water molecules that reside at different distances from the inhomogeneous and changing with time surface of the aggregates of trehalose molecules. A more in deep analysis is needed to better understand the different contributions coming from these populations to the presented averaged behaviour.

Fig. 4.17 reports the MSD of hydrogen atoms of the hydroxyl groups of trehalose and of the oxygen atom of the glycosidic linkage of trehalose of the solutions with 40.65 *wt%* concentration in trehalose for all temperatures. The plots show only the middle e long time window, due to the frequency with which the configurations have been saved during the production runs.

Compared to the MSDs of hydration water, the MSDs of the selected atoms of the disaccharide show a slower dynamics with a plateau region that extend on a time scale of three order of magnitude at the lowest temperature.

To characterize quantitatively how the temperature influences particle movements in the two systems, the values of the MSD of hydration water oxygen at $t = 100$ ps (that is outside the plateau region), the values of the MSD of the hydrogen atoms of the hydroxyl groups of the trehalose (the atoms that interact the most with water) and the values of the oxygen atom between the two rings of glucose, the glycosidic linkage of the trehalose, both at $t = 500$ ps, have been collected and plotted against the temperature. The results are reported in Fig. 4.18 as a function of temperature for both investigated systems. It can be observed that all the MSDs show three changes of slope upon cooling. The first one, at $T = 280$ K in both systems, happens concurrently with the formation of the extended cluster of trehalose molecules as already detected in the analysis of cluster formation and in the long relaxation time. The high value of derivative of the high temperature MSD linear behaviours shows that when trehaloses are not aggregated fluctuations are more extended and this behaviour reflects to hydration water too.

The second change of slope happens approximately at 250 K in the box with higher concentration in trehalose and around 260 K in the box with lower concentration in trehalose. This crossover is also present in the long relaxation time and it is also found in proteins where it has been related to the PDT [99]. This change of slope has been observed also in an experimen-

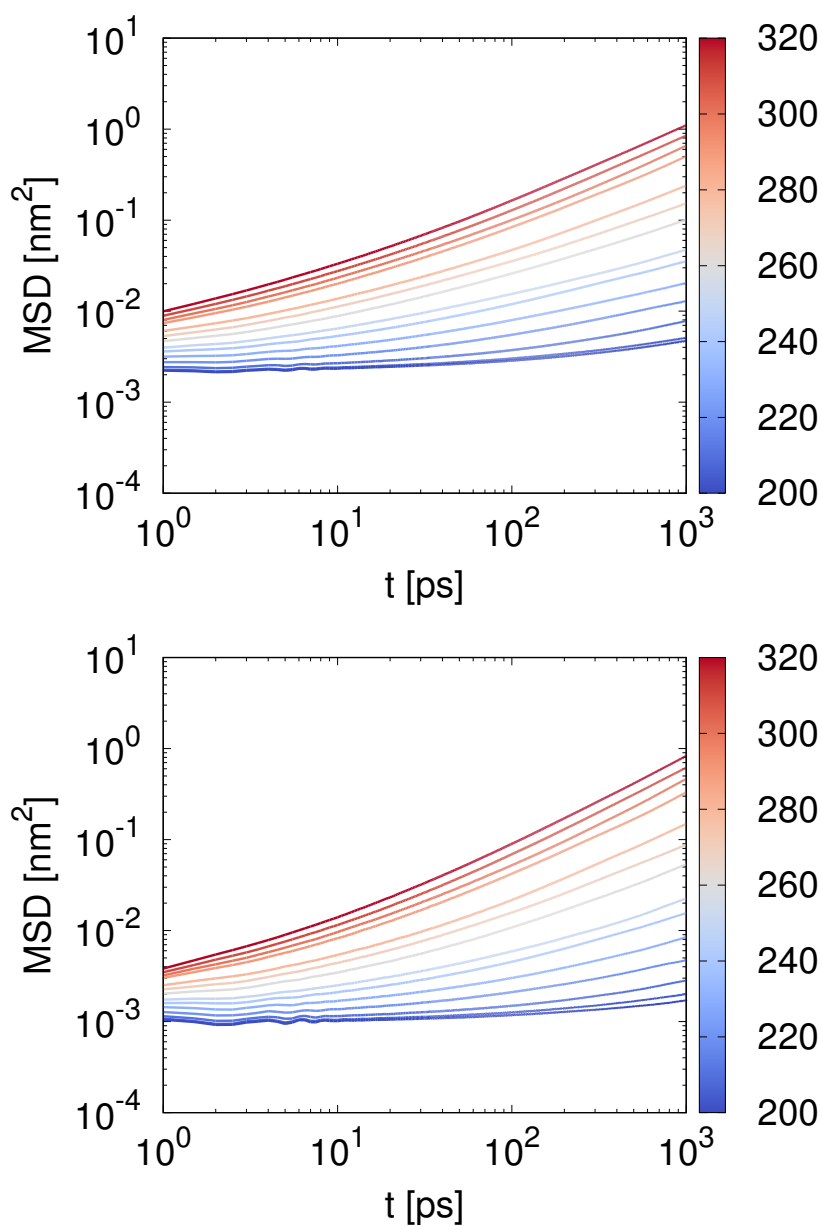


Figure 4.17: Top panel: Mean Square Displacement of the hydrogen atoms of the hydroxyl groups of trehalose for the solutions with 40.65 wt% concentration in trehalose for all temperatures. Bottom panel: Mean Square Displacement of the oxygen atom of the glycosidic linkage of trehalose for the solutions with 40.65 wt% concentration in trehalose for all temperatures.

tal work by Magazù *et al.* in a solution of water and trehalose [120, 121]. Since below 280 K the macroaggregate of trehalose has formed, this second

crossover can be considered the equivalent of the PDT. It is interesting to also note that it happens at a temperature in the range of the typical temperatures of the PDT 260-220 K.

The third crossover, best evident in the insets, happens at $T \approx 225$ K for both concentrations, and corresponds to the FSC that has been observed in the α relaxation time of hydration water (see Fig. 4.13).

It can therefore be said that these MSDs show a complete dynamical coupling between trehalose molecules movement and hydration water movements as the crossovers in the dynamics of trehalose atoms upon changing temperature perfectly match those found for the hydration water oxygens. The entity of displacements of the glycosidic linkage oxygen is circa half of that of the hydrogen of the hydroxyl group who directly hydrogen bonds to water. Moreover comparing the displacement of equivalent atoms in the two different systems, one can note that the values for all the investigated quantities are greater for the less concentrated solutions, as expected for a system in which the glassy matrix composed of trehalose clusters is less extended.

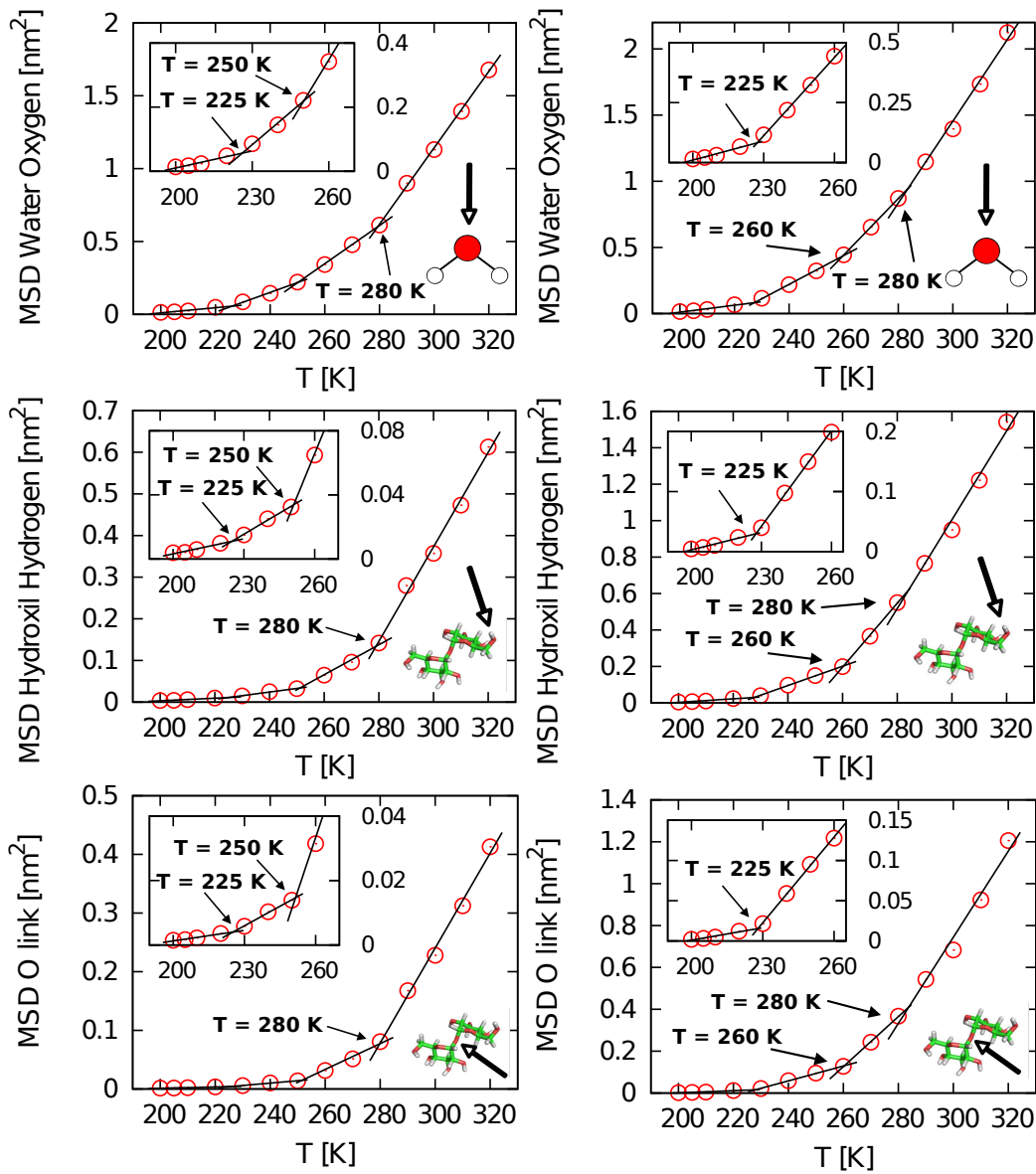


Figure 4.18: Values of MSD for different atoms for all the simulated temperatures. Black lines are linear fit. Top panels: value at 100 ps of the MSD of the oxygen atom of water molecules inside the hydration layer. Middle panels: value at 500 ps of the MSD of the hydrogen atom of the hydroxyl groups, OH, of trehalose molecule. Bottom panels: value at 500 ps of the MSD of the oxygen atom of the glycosidic linkage. In each panel the kind of atom of the molecule considered for the calculation of the MSD is indicated by an arrow pointing to the molecule. The three crossover temperatures are indicated by arrows in each panel. Left column refers to MSDs for system with 40.65 wt% concentration in trehalose. Right column refers MSDs for system with 20.21 wt% concentration in trehalose.

4.5 Hydrogen Bonds

In this Section Hydrogen Bonds properties of hydration water are analyzed. Fig. 4.19 reports the distributions of water-water HBs per water molecule (top panels), the angular distribution function of the angle γ (middle panels) and the distribution of the Orientational Tetrahedral Order parameter q (bottom panels). Left column refers to quantities calculated in the more concentrated solution, right column refers to quantities calculated in the more diluted one. For details on these quantities and on the definition of hydrogen bond used, see Section 3.8.2.

From top panels it can be seen that most of the water molecules surrounding trehaloses form three HBs with other water molecules. These peaks are stable upon cooling, with a minor increase at lower temperatures. As the solutions are cooled, the fraction of water molecules that form four HBs increase becoming the second most numerous population in hydration water. At the same time the fraction of water molecules with one and two HBs decrease upon cooling. No water molecule forms more than five HBs.

It is interesting to note that, while the main peak at three HBs per water molecule has approximately the same height in the two water-trehalose solutions, the more concentrated one shows a slightly higher peak around 4 HBs per water molecule.

The distributions of the angle γ between three oxygen atoms show a peak at around 0.6 due to interstitial water, while the main peak is around -0.20 at high temperature and becomes more sharp and moves towards lower values as the temperature is decreased. A shoulder at around 0.25 is also present and is more pronounced at high temperature. Both solutions presents these features but the main peak seems to be sharper in the less diluted solution. The distribution of the parameter q shows a change in the tetrahedral geometry of the water HBs network. At high temperature the main peak is around 0.5 in both solutions, with a small shoulder near 0.7. As the temperature is lowered, the main peak decreases and the shoulder raises and moves towards higher values of q , signaling an increase in the tetrahedrality, although tetrahedrality is very weak for this hydration water if compared with bulk. In the 40.65 wt% concentration in trehalose solution the peak at 0.5 and at 0.82 are of the same height at 200 K, while in the more diluted solution the peak at 0.5 remains the highest at all the investigated temperatures.

To make a direct comparison with the properties of the HBs network of bulk water, Fig. 4.20 reports the three analyzed quantities at the lowest and highest temperature studied, $T = 320$ K and $T = 200$ K respectively, for bulk water and the water-disaccharide mixtures.

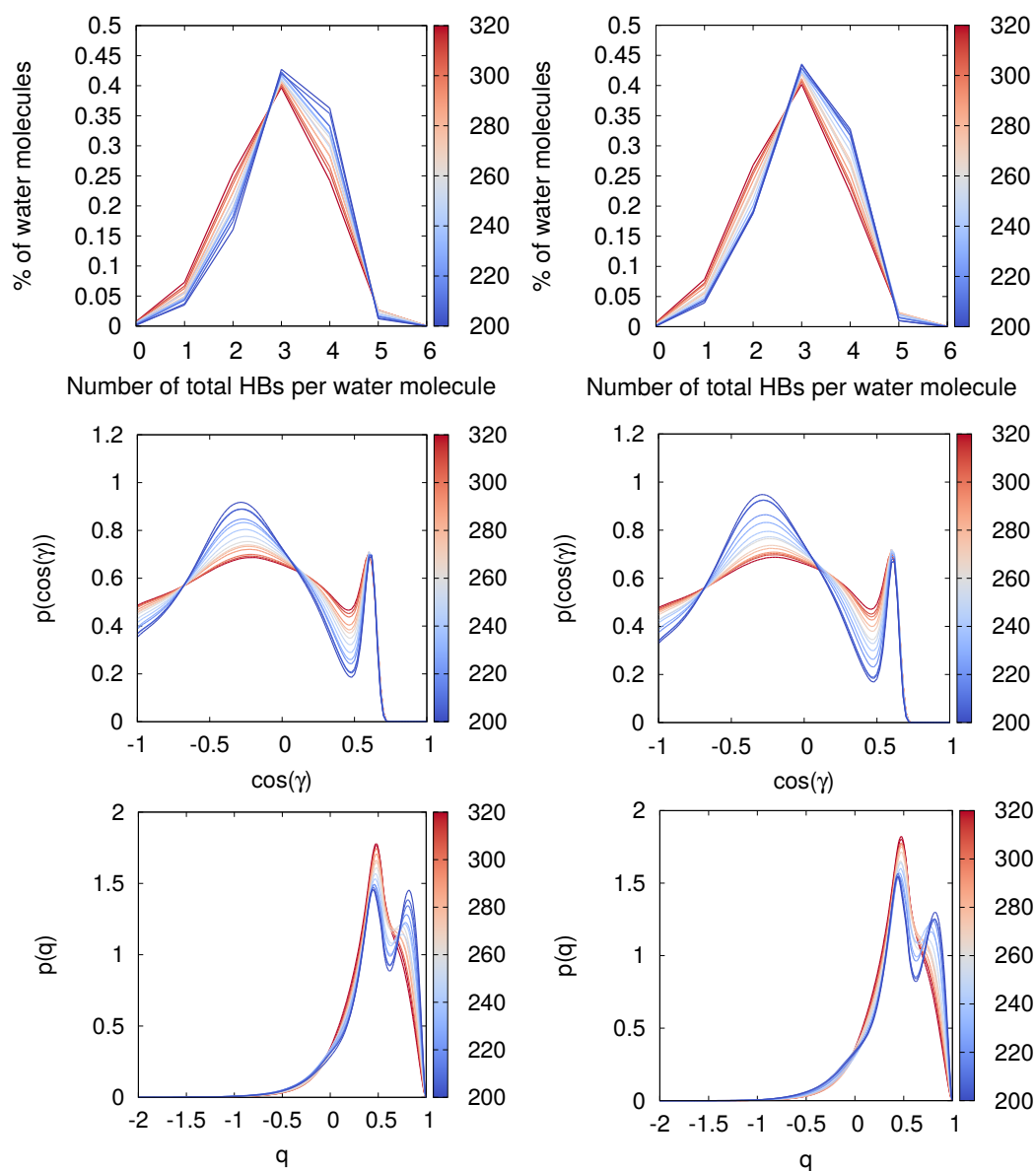


Figure 4.19: Top panels: distributions of the number of Hydrogen Bonds formed per water molecule. Middle panels: normalized angular distribution functions $p(\cos(\gamma))$ of the angle between the oxygens of three nearest neighbour water molecules. Bottom panel: normalized distribution of the Orientational Tetrahedral Order parameter q . Left panels refer to the solution with 40.65 wt% concentration in trehalose, right panels to the solution with 20.21 wt% concentration in trehalose.

In the left column all plotted quantities refer to system at $T = 320$ K. Small differences are visible between hydration water of the two binary mixtures, while the deviation from the typical behaviour of bulk water is evident, with a marked change in the fraction of water molecules with a given number of HBs and in the arrangement of hydrogen bonded water molecules. In particular in bulk water the population with four HBs is the most abundant at all temperatures with a distribution that in general is located at higher values of the number of hydrogen bonds. Differences are even more accentuated at low temperature ($T = 200$ K in the right column), where the strong influences of nearby trehalose molecule is clear. The distribution of the population of water molecules with a given number of HBs is much more broad and centered around three in hydration water, whereas in bulk water the vast majority of water molecules has 4 HBs formed with other water molecules and none of them has two or less hydrogen bonds. Also the disposition of water molecules is greatly affected by the presence of the disaccharide, with an evident change in the tetrahedral configuration of the HBs network, best evident in the distribution of the parameter q : where bulk water presents an high peak around 0.85, thus signaling a preferential tetrahedral geometry, and a small shoulder around 0.5, hydration water presents two peak of roughly the same height at around 0.45 and 0.83. At low temperature the differences between the HBs properties of the two populations of hydration water are enhanced. In the more concentrated solution the fraction of molecules with four HBs is higher. The distribution of the angle γ is narrower in the 20.21 *wt%* mixture with a peak centered at a slightly lower value of γ . From distribution of the parameter q results that in the more concentrated solution, the two peaks at 0.45 and 0.83 are equal, whereas the one at 0.45 is higher in the more diluted solution. The distribution of γ and of q seems to give different description of the geometric structure of the HBs network, but it is important to note that in the computation of the Orientational Tetrahedral Order parameter, only the first three nearest neighbours molecules are taken into account (see Eq. (3.67)).

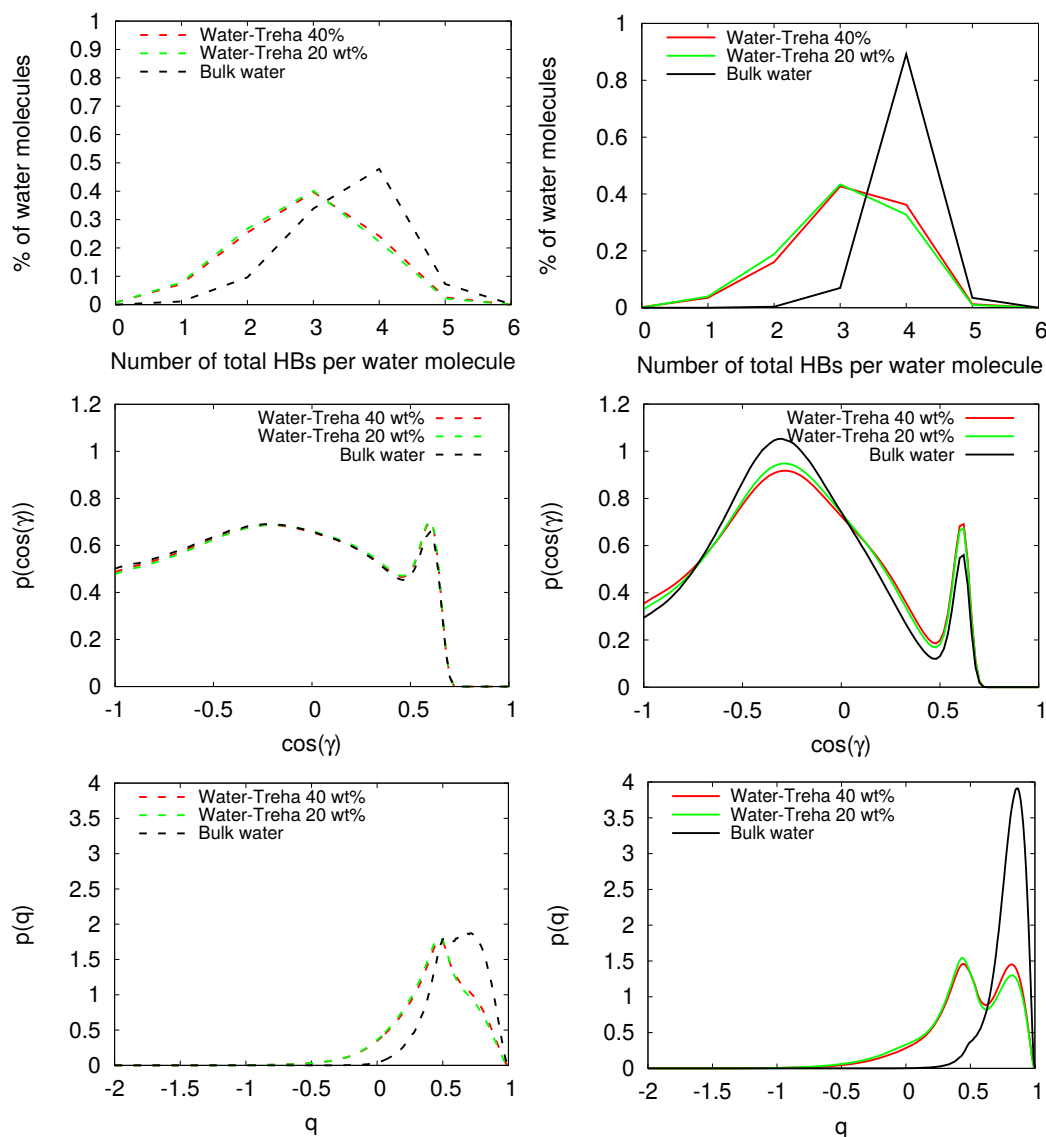


Figure 4.20: Comparison of the number of Hydrogen Bonds per water molecule (top panels), angular distribution function $p(\cos(\gamma))$ (middle panels) and distribution of the Orientational Tetrahedral Order parameter q (bottom panels) between hydration water of the 40.65 wt% solution (red lines), hydration water of the 20.21 wt% solution (green lines) and bulk water (black lines). Left panels refer to 320 K, right panels to 200 K.

4.6 Conclusions

Trehalose has a strong effect on both dynamics and statical features of surrounding water molecules.

From MD simulations on two systems with different concentration in trehalose it is found that the interactions between molecules of the disaccharide and of water in the hydration layer modify how the water behaves. Translational dynamics of water has been investigated through Self Intermediate Scattering Functions in a Mode Coupling Theory framework. These correlators show the usual two-steps relaxation typical of glass former liquids such as bulk water. In addition a long time, slow relaxation process has been found. These new feature can be modeled with a functional form with a Gaussian term and two stretched exponentials that describes very well the decay of the correlators. From the fitting procedure characteristic times of the α -relaxation process and of the *long*-relaxation process have been extracted.

The middle time α -relaxation retains the characteristic features and phenomenology of bulk water relaxation with a slight slow down probably due to interactions with trehalose molecules. The Fragile to Strong Crossover is present in both solutions and may be connected to the crossing of the Widom line, as observed in bulk water [122]. The general shift of the dynamics of hydration water to higher temperatures has been observed in many other systems, like for example confined water [73, 123, 124], electrolyte solutions [97, 97, 115] and water-sugar mixtures [11, 12].

The *long*-relaxation process is a new slow decay of the correlators to zero that is absent in bulk water but it has been observed in MD simulations studies of translational dynamics of hydration water of protein [12, 99, 100], of water molecules in a disaccharides-water mixture [11], mixtures of water and microgels [117] and in experimental works on biological mixtures [108, 109]. In this work, focusing on translational dynamics of water molecules in the hydration layer, it has been possible to ascribe the long time relaxation to water nearby trehalose molecules. The characteristic time τ_{long} shows two changes of trend as a function of temperature. The first one at around 280 K is connected with the formation of macroaggregate of trehalose molecules, as seen from a study of the clustering properties of the disaccharide. The second one happens around 250-260 K. In general the slowing down of the dynamics of hydration water is due to the interaction with trehalose clusters that hinder the natural motion of water molecules.

Using the Mean Square Displacement of oxygen atoms of water and of selected atoms of trehalose, a complete dynamical coupling between the motion of water and of clusters of trehalose has been observed. Three changes of

slope characterize the MSD as a function of the temperature. The first one, at 280 K, is connected with the formation of trehalose clusters, as already seen in the behaviours of τ_{long} . A second change is observed around 250 K. Finally the third one happens at 225 K, near the FSC transition observed in the study of τ_{α} .

The dynamical transition observed around 250-260 K in both the long characteristic time τ_{long} and in the MSDs resembles the Protein Dynamical Transition observed in hydrated protein. This enhancement of the flexibility of the protein upon heating has been observed both experimentally and in simulations and happens in the 200-260 K temperature range. A previous study connected this transition in a protein to a change in the trend of τ_{long} [99]. This is the first evidence of a dynamical transition in a self assembled structure composed of small biological molecules, whose motion reflects on dynamical properties of surrounding water and vice versa.

The presence of trehalose molecules in a water mixture has a great impact also on the formation and resulting structural properties of the network formed by hydrogen bonded water molecules. Water molecules in the hydration layer of trehalose show a reduced number of hydrogen bonds with other water molecules, probably due to the interaction with the disaccharide. Moreover a change in the configuration of bonded molecules has been observed, with an overall reduction of the tetrahedral configuration typical of bulk water.

Due to all the observed properties of water in a water-trehalose mixture, this disaccharide results to be a very good candidate as a cryoprotectant for biological solutions. The slow dynamics and the disruption of water HBs network are connected to the hampering of the formation of water crystal ice that can damage biological molecules and alter their functionality.

Chapter 5

The lysozyme - trehalose - DMSO aqueous solutions

In this Chapter simulations of the multicomponent mixture of water-trehalose-DMSO-lysozyme are presented, together with results from the study of the produced trajectories [125]. In Section 5.1 a short introduction on DMSO is reported along with details on the simulations. Section from 5.2 to 5.5 deal with dynamical properties of water and lysozyme. In Section 5.6 results from water-water HBs analysis are presented. In Section 5.7 conclusions are drawn.

5.1 Systems and simulation details

Dimethyl sulfoxide (DMSO) is a chemical compound composed of one sulfur atom, one oxygen atom, two carbon atoms and six hydrogen atoms. A pictorial representation of a DMSO molecule is depicted in Fig. 5.1 .

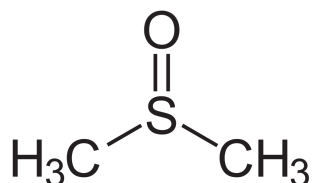


Figure 5.1: Diagrammatic representation of a dimethyl sulfoxide molecule.

DMSO molecule has two hydrophobic groups (CH_3) and one hydrophilic group (SO) that, due to the partial negative charge on the oxygen atom, favors the formation of hydrogen bonds with water molecules. It is interesting to note that, while water molecule acts both as donor and as accep-

tor in the formation of hydrogen bonds, DMSO molecule can act only as a donor [126, 127]. Many computational and experimental works showed the nonideal behaviour of aqueous binary mixture of DMSO, with a strong dependence on the concentration, with a maximum of the anomalies for a concentration of DMSO around 30 % molar fraction. This is thought to be connected with the formation of large spanning cluster of DMSO molecules starting at a concentration of 10-15 % molar fraction [127, 128].

The strong interaction with water molecules causes a more structured first hydration shell around a DMSO molecule, with a sharper first peak of the radial distribution function, while the positions of the peaks are weakly affected. This is due to both excluded volume effect and to the formation of a local tetrahedral structure. This feature is enhanced upon increasing the concentration of the DMSO, until its massive presence in the solution has the opposite effect of disrupting the HBs water network [129].

Moreover it has been seen from molecular dynamics simulations that in a binary mixture water-DMSO hydrogen bonds last longer than water-water HBs, that in turn last longer than water HBs in bulk water [129].

Dimethyl sulfoxide is a solvent that is also widely used in cryopreserving solution, often in combination with other compounds like, for example, trehalose [130, 131]. It is particularly useful in that it can penetrate biomembrane and increase the permeability of the biomembrane itself to other small molecules like, for example, water. As a cryoprotector it is used as vitrification agent [132] and for its ability to diminish the osmotic pressure imbalance present during cryopreservation protocols [133].

Cryoprotecting agents can be divided in two classes, intracellular agents (e.g. DMSO) and extracellular agents (e.g. trehalose). Both improve the osmotic imbalance that occurs during freezing and are useful in the vitrification of the biosolution. Molecules that are able to penetrate biomembrane can act also inside the cells, whereas bigger molecules like trehalose complete their cryoprotecting in the serum around cells.

To enquire the possible combined effect a mixture of DMSO and trehalose has on the properties of a supercooled biological solution containing a lysozyme protein, three systems with different composition have been simulated and structural and dynamical quantities calculated from the resulting trajectories. Also for these systems, particular attention has been posed on the properties of water molecules in the hydration layer 0.6 nm thick around the lysozyme protein.

The lysozyme is an antimicrobial enzyme consisting of 129 amino acid residues having a molecular weight of 14.4 kDa. It folds into a compact globular struc-

ture with an ellipsoidal shape and dimensions $a \times c \times c = 2.25 \times 1.3 \times 1.3$ nm. It is widely used in experiment and MD simulations as paradigmatic model of a protein.

For the multicomponent lysozyme-trehalose-DMSO-water solution, three boxes corresponding to the three different solutions have been made:

- 52.36 *wt %* in water, 34.93 *wt %* in trehalose, 9.74 *wt %* in DMSO, 2.97 *wt %* in lysozyme (1 lysozyme molecule, 13982 water molecules, 491 trehalose molecules, 600 DMSO molecules, 8 Cl⁻ ions).
- 55.18 *wt %* in water, 26.81 *wt %* in trehalose, 4.88 *wt %* in DMSO, 3.13 *wt %* in lysozyme (1 lysozyme molecule, 13982 water molecules, 491 trehalose molecules, 285 DMSO molecules, 8 Cl⁻ ions).
- 85.13 *wt %* in water, 10.03 *wt %* in DMSO, 4.84 *wt %* in lysozyme (1 lysozyme molecule, 13982 water molecules, 380 DMSO molecules, 8 Cl⁻ ions).

The Cl⁻ ions were added to ensure the electrical neutrality of the systems. The first two systems differ only by the number of DMSO molecules and are intended to search for differences produced by various concentrations of this compound in the hydration water. It is interesting to note that a concentration of 10 *wt %* in DMSO is the most common quantity used in the preparation of cryopreserving solutions. This concentration corresponds, in the system without trehalose, to a 0.026 molar fraction.

The MD simulations were carried out using the GROMACS 5.1.4 package [134]. CHARMM force field was used for modeling the bonded and non-bonded interactions for sugar [83, 84] and SPC/E potential for water molecules [78], which is compatible with CHARMM [95].

To integrate the equations of motion the Verlet leapfrog algorithm with a time step of 1 fs was used. A cut-off of 1 nm was set for the non-bonded Van der Waals interactions. To handle the electrostatic interactions the Particle Mesh Ewald method was used. Boxes were cubic and Periodic Boundary conditions were used to minimize finite size effect. Systems were simulated at constant pressure $P = 1.013$ bar and at temperature spanning from $T = 300$ K to $T = 200$ K. The Berendsen method [76] was used to control both the temperature and the pressure during the equilibration phase (NPT), whose duration ranged from 15 ns to 100 ns. The time evolution of the total energy has been monitored to control the correct equilibration of the systems during this stage. Fig. 5.2 report for selected temperatures the total energy

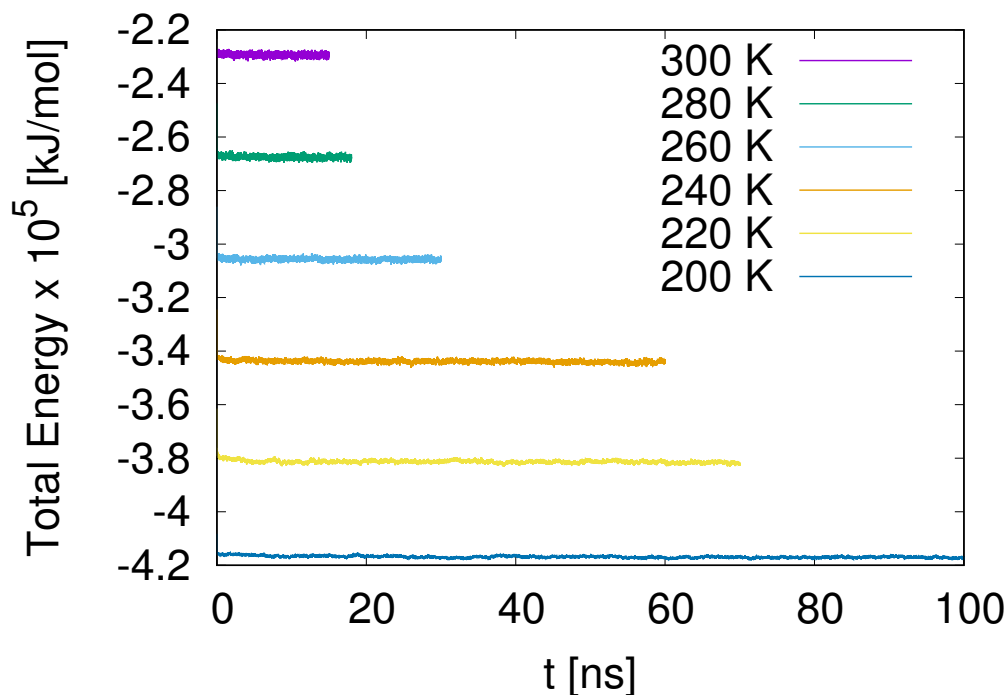


Figure 5.2: Total energy of the system with lysozyme, trehalose and DMSO with a concentration of 10 *wt* % as a function of the time during the equilibration phase for selected temperatures.

as a function of the time for the system with lysozyme, trehalose and 10 *wt*% concentration in DMSO. All the reported energies reach a stable value with no drift, signaling a correct equilibration of the solution.

For production runs the control of pressure and temperature with Berendsen was removed, using instead a mild coupling with temperature with Nosé-Hoover thermostat to avoid energy drift on the longest simulations. The length of the production runs ranged from 25 ns for high temperatures to 75 ns for low temperatures.

In between the equilibration phase and the production run, a 0.5 ns longer preproduction stage permits the system to adapt to the change of the algorithm used to control the temperature.

Details on the simulations length are reported in Table 5.1. Total energy E_{tot} and total density ρ of the three systems after equilibration are reported in Table 5.2.

After the simulation part, dynamical (in particular SISFs and MSDs) and

T [K]	t_{eq} [ns]	t_{pp} [ns]	t_{prod} [ns]
300	15	0.5	25
290	15	0.5	25
280	18	0.5	35
270	30	0.5	35
260	30	0.5	35
250	60	0.5	45
240	60	0.5	45
230	70	0.5	55
220	70	0.5	55
210	90	0.5	65
205	90	0.5	65
200	100	0.5	75

Table 5.1: Length of the stages of the MD simulations for all the temperatures.

structural (water-water hydrogen bonds) quantities were used to characterize the impact that the solutes have on hydration water surrounding the lysozyme protein. In such multicomponent complex mixture, many direct and indirect effects given by the interplay between solutes and solvent are possible. For example water molecules in the hydration layer may be subject to the effect played by the protein, trehalose and DMSO molecules separately on them, but they can also show indirect effects due to the impact that the different solvent molecules have on lysozyme. Obviously also the opposite is true, that is the effect water has on the other components of the solution. In this work the study of water in the hydration shell of lysozyme will produce an average behaviour resulting from all these combined direct and indirect interactions.

Already at visual inspection it can be seen that the different components of the mixture behave differently. Fig. 5.3 reports a snapshot of a slice of the system with lysozyme, trehalose and DMSO at $T = 230$ K after equilibration. Trehalose molecules appear to aggregate in cluster that surround the protein whereas DMSO molecules appear to be uniformly distributed in all the system. To quantify to which extent the solutes reside in the hydration shell, the average fractions of molecules of the chemical compounds that are inside the hydration layer of the protein have been computed. Results are reported in Fig. 5.4 for all the systems as a function of the temperature. The fraction of DMSO molecules in the hydration shell slightly increase upon cooling in the solutions with also trehalose added in the mixture (see Fig.

T [K]	Lyso-DMSO 10 wt%		Lyso-Treha-DMSO 5 wt%		Lyso-Treha-DMSO 10 wt%	
	E_{tot} [kJ/mol]	ρ [kg/m ³]	E_{tot} [kJ/mol]	ρ [kg/m ³]	E_{tot} [kJ/mol]	ρ [kg/m ³]
300	-633032	1023.92	-174394	1171.73	-228848	1169.13
290	-646486	1029.5	-192557	1178.03	-248200	1175.94
280	-660085	1034.4	-211129	1184.43	-267709	1182.24
270	-673823	1038.7	-229415	1190.41	-286524	1188.18
260	-687590	1042.45	-247939	1194.88	-305951	1193.63
250	-701569	1044.92	-266323	1199.59	-324846	1199.2
240	-715492	1046.56	-284861	1204.63	-343697	1203.46
230	-729807	1047.28	-303136	1207.13	-362373	1208.4
220	-743578	1048.1	-320841	1209.48	-381810	1211.04
210	-757469	1047.04	-338819	1211.14	-399382	1215.33
205	-764415	1046.92	-347638	1214.58	-408543	1217.31
200	-771559	1045.77	-356539	1214.26	-417258	1217.71

Table 5.2: Average total energy and average total density of the simulated systems after equilibration along the $P = 1.013$ bar isobar.

5.4 , panel a). The fractions concerning the systems with different DMSO concentration show only small differences despite the molecules of DMSO are almost doubled in the more concentrated solution. In the system without trehalose, the fraction of molecules of dimethyl sulfoxide remains roughly constant, with large fluctuations, upon changing the temperature and is however always greater than the fraction present in the other two systems (the ones with trehalose). This is easily explained by the fact that without the disaccharide, DMSO has more space to occupy around the protein and can move freely without the hindering effect of the disaccharide. For what concerns trehalose (panel b), the fraction of molecules presents around the lysozyme, at high temperatures, it is slightly greater in the more concentrated DMSO solution. At low temperature, from 230 K and below, the fraction is approximately the same for both the mixture with the disaccharide. Finally, the fraction of water molecules inside the hydration shell increase with decreasing content of the DMSO and trehalose solutes, the maximum values being in the system without trehalose (panel c). This is compatible with the fact that there is less excluded volume in that mixture. In all cases the fraction of molecules in the hydration shell is equal to or less than 10% of the total number of molecules of each species.

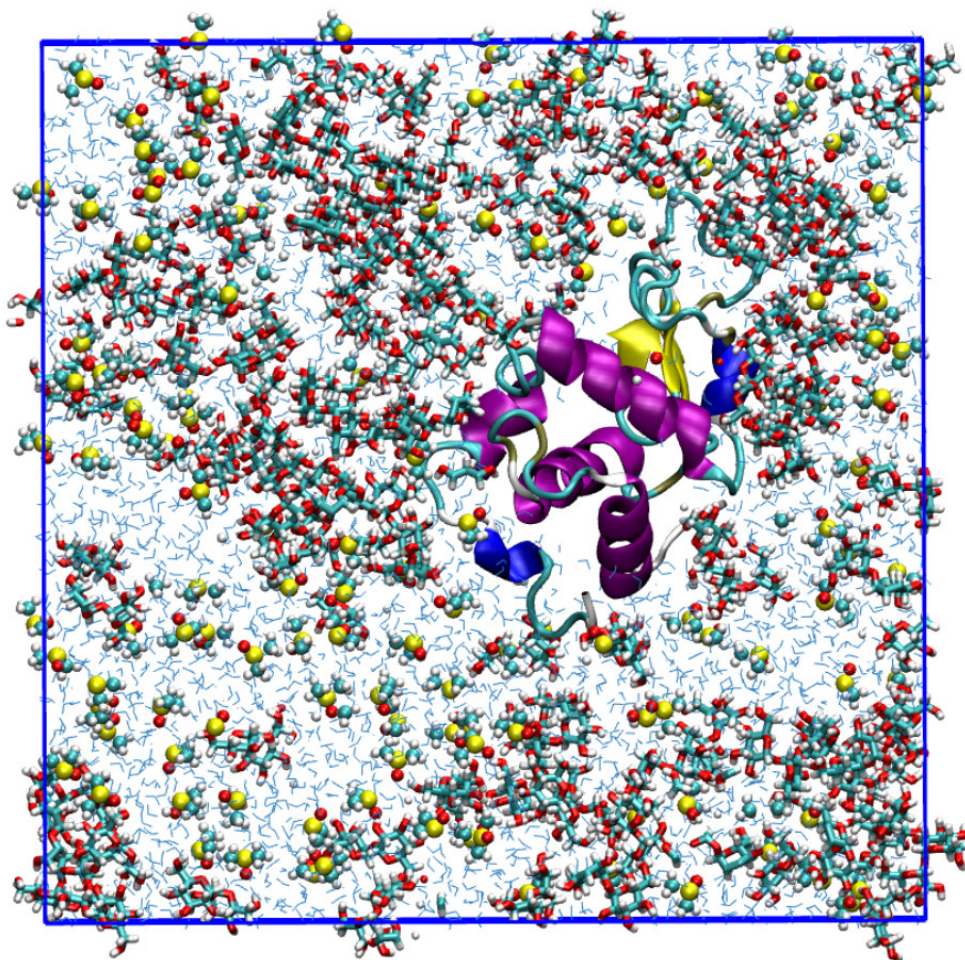


Figure 5.3: Snapshot of a configuration of the solution with lysozyme, water, trehalose and DMSO with a 10 *wt%* concentration at $T = 230$ K.

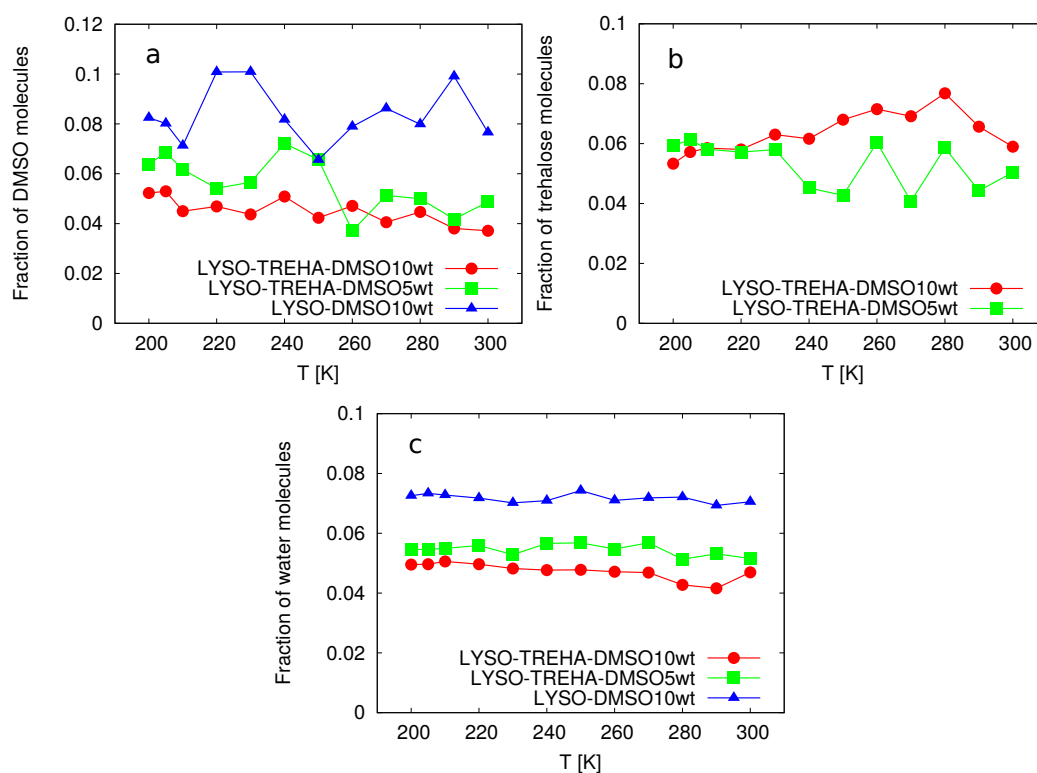


Figure 5.4: Average fraction of molecules in the hydration layer 0.6 nm thick around lysozyme protein. Panel a : average fraction of DMSO molecules. Panel b : average fraction of trehalose molecules. Panel c : average fraction of water molecules.

5.2 Translational dynamics of hydration water

Oxygen-oxygen Self Intermediate Scattering Function of water molecules inside the 0.6 nm thick hydration layer around lysozyme has been used to characterize the translational dynamics of hydration water upon lowering the temperature. All the correlators presented in the following are calculated at $q_{max} = 2.25 \text{ \AA}^{-1}$, where the characteristic features of glassy dynamics of the systems under investigation are best visible.

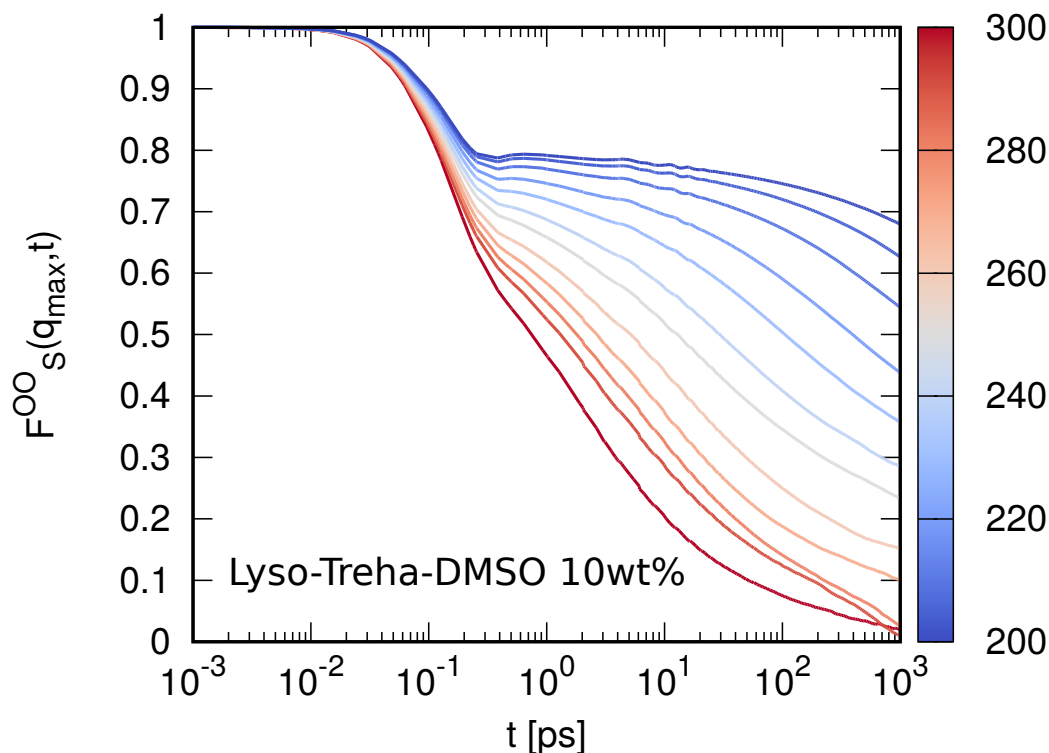


Figure 5.5: Oxygen-oxygen SISFs for hydration water of the system with lysozyme, trehalose and DMSO with a concentration of 10 *wt%* for all the simulated temperatures. SISFs are calculated at $q_{max} = 2.25 \text{ \AA}^{-1}$.

Fig. 5.5 reports SISFs for hydration water of the solution with lysozyme, trehalose and the highest concentration of DMSO for all the simulated temperatures. As already seen in the binary water-trehalose mixture, also in this case a slow multi-steps relaxation of the correlators is evident. In particular the first Gaussian decay that ends at around 0.2 ps shows only a weak dependency on temperature. The successive relaxation spans several order of magnitude in time, starting at around 0.3 ps and ending past several nanosecond. The slowing down of the dynamics of the system, signaled

by the change in the times the correlators take to decay to zero is very remarkable: at $T = 300$ K SISF almost reach a zero value already after 1 ns, with a complete relaxation, whereas the correlator for the lowest temperature investigated, that is $T = 200$ K, in that time only reaches a value that is slightly below 0.7. The multi steps decorrelation and the appearance of a plateau region is a mark of the onset of transient trapping inside a cage of nearest neighbours. The time a cage takes to break increase with decreasing temperature as is clear by the fact that the plateau region is more extended in time for lower temperatures.

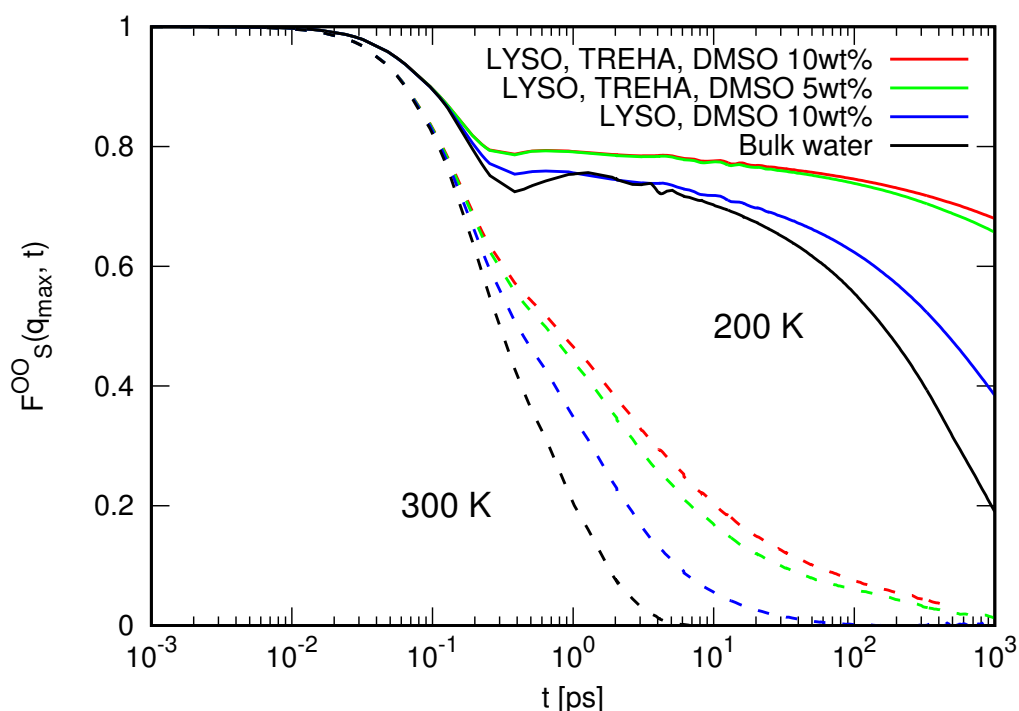


Figure 5.6: Oxygen-oxygen SISFs for hydration water in all the three biological solutions at two selected temperatures, 300 K and 200 K respectively. SISFs for bulk water are reported with black curves as reference.

The comparison of oxygen-oxygen SISFs calculated in the three different solutions for the highest and the lowest temperature investigated (300 K and 200 K) is reported in Fig. 5.6 along with the oxygen autocorrelator for bulk water depicted as black lines for reference. All the correlators coming from the biological solutions are slower than the one corresponding to bulk water. This is due either to the fact that those are correlator for hydration water, that thus are affected by the nearby presence of the protein, and to

the presence of other solutes in the mixtures, i.e. DMSO and trehalose. The great impact that the combined action the multicomponent systems has on the dynamics of water upon cooling is evident in the correlators calculated at $T = 200$ K. In particular trehalose has an important role in the modification of the dynamics of the solvent, by increasing the relaxation times and stretching the decay of the correlators over many decades. Comparing SISFs at 200 K from the two solutions with trehalose and DMSO, it results that also the addition of more DMSO, from 5wt% to 10wt%, in the solution has an impact on the solvent dynamics, with the correlators that show a relaxation time that increase with increasing concentration of DMSO. Also the SISFs for water at the interface with lysozyme in the solution with DMSO but without trehalose are slower compared to the ones of bulk water, this is due to the combined interaction with DMSO and with the protein surface.

At the highest temperature simulated, $T = 300$ K, all the correlators fully decay within 1 ns, with the SISFs of hydration water that also in this case are slower than bulk water and keep the same ordering seen at lower temperature. The comparison with the decay of the correlator of bulk water is particularly useful and some comments are in order at this point. The first short time relaxation is common to all correlator and shows the same temperature behaviour. A marked change in dynamics is present upon lowering the temperature, with the systems with lysozyme, trehalose and DMSO being much slower than bulk water. The onset of the α -relaxation at high temperatures and of the plateau region at low temperatures happens around 0.3 ps. Given the proved fact that bulk water shows a Gaussian relaxation and a slower structural α -relaxation, it is evident that correlators of hydration water present a different shape that cannot be ascribed to only a longer structural relaxation time or a more stretched in time dynamics. The Boson peak is much less evident in the hydration water with respect of bulk water and the ripples due to finite size effects are slightly shifted towards longer times since the boxes are larger and they are, however, less pronounced.

Previous works on water surrounding biomolecules [11, 12, 99, 100] showed that the shape of the correlators can be described by a new functional form that extends the one predicted by MCT with an additional stretched exponential that follows long tails of the SISFs along their decay. This functional form was the one used also for the water-trehalose solutions (see Eq. (4.2)).

Fig. 5.7 shows selected correlator for the system with lysozyme, trehalose and the highest concentration of DMSO, that is the one that presents the slowest dynamics among all the systems investigated. Superimposed black lines are best fit via Eq. (4.2). As can be seen the functional form with two stretched exponential is able to reproduce very well the shape of the SISFs through all its time evolution.

Fits are equally good also for the other two systems investigated (not shown).

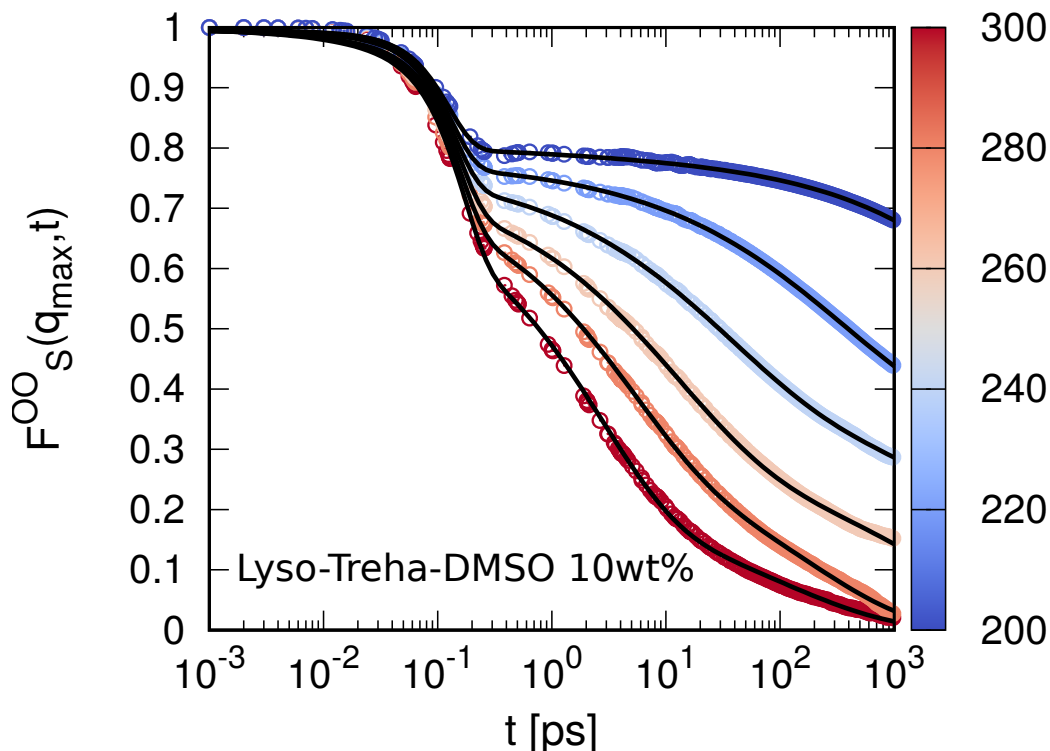


Figure 5.7: Selected SISFs of hydration water for the aqueous solution with lysozyme, trehalose and DMSO with a concentration of 10 *wt%*. Superimposed black lines are best fits with Eq. 4.2

Parameters resulting from the fit procedure are reported in Fig. 5.8 for all the temperatures and systems simulated. Left column reports parameters pertaining to the structural α -relaxation, right column reports parameter that describe the long relaxation.

Prefactors f_α and f_{long} account for the weight each relaxation process has on the whole decay of the correlator. They show different behaviour depending on the presence of trehalose in the solution. In particular in the system without trehalose the α -relaxation is the most relevant one ($f_\alpha > f_{long}$) with only a weak dependence on temperature. In fact f_α remains around 0.5 and f_{long} moves from 0.2 at high temperatures to 0.3 at low temperatures. On the contrary the relative importance of the two relaxation processes changes upon changing the temperature in the solutions with trehalose. f_α start from a value around 0.5 for both the systems at 300 K (where also the value for the system without trehalose is) and decreases upon changing the temperature.

The variation with temperature is at first mild in the 300 - 230 K temperature range and becomes more steep under 230 K. Final values are between 0.1 and 0.2. f_{long} behaves in the opposite way, it starts around 0.2 in both the solutions with trehalose and reaches a final value that is between 0.6 and 0.7. There is thus a crossing of the two prefactors between 240 K and 220 K.

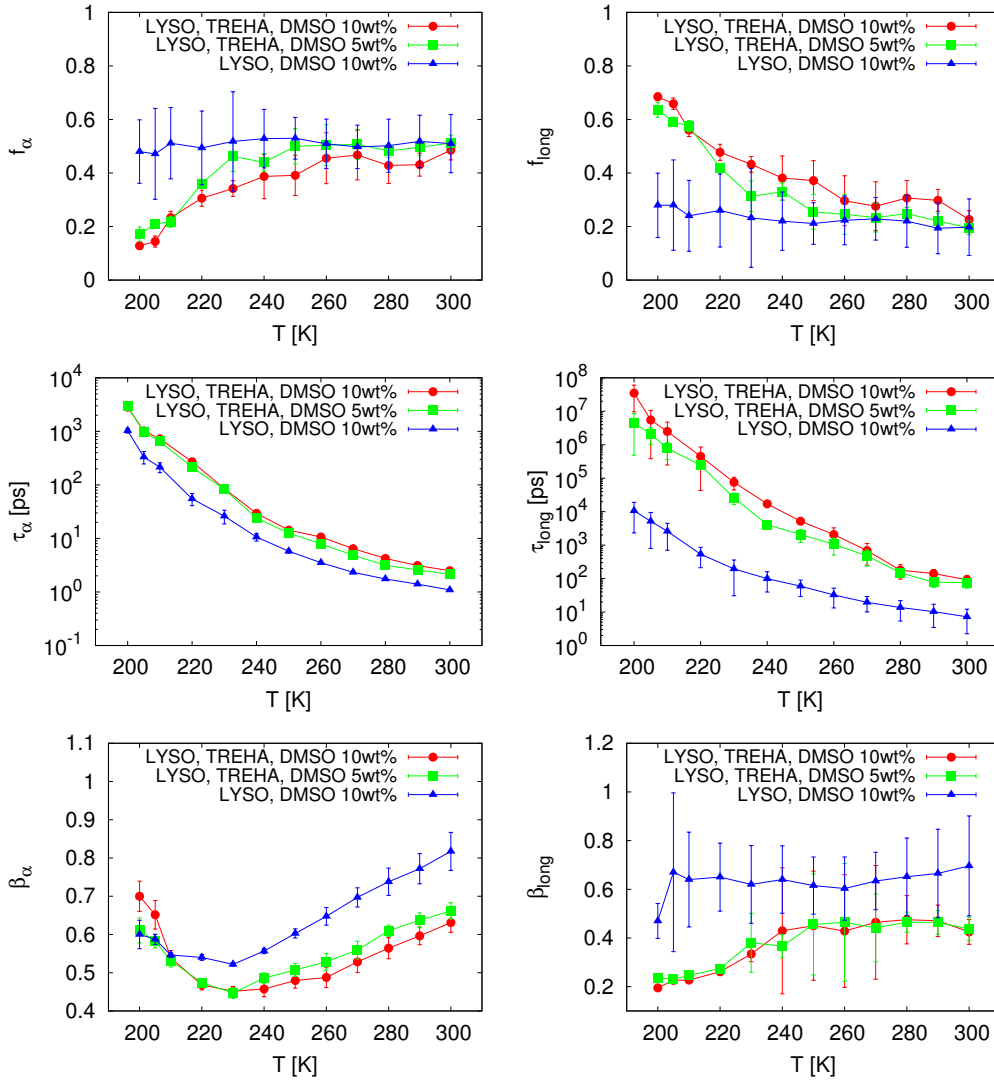


Figure 5.8: Results of the fitting procedures via Eq. 4.2 of the oxygen-oxygen SISFs of hydration water for the three simulated systems. Left panels refer to α -relaxation, right panels refer to long-relaxation.

The two characteristic relaxation times are reported in the middle panels. On the left column all the α -relaxation times show similar features, increasing by about three order of magnitude upon lowering the temperature in the 300-200 K range analyzed. α -relaxation times are similar in the two mixture with trehalose and greater than the one of the system with only lysozyme and DMSO by a factor 2-3. Differences in the change of τ_{long} with the temperature are more marked. The long relaxation time for the solution without trehalose increase by three order of magnitude, starting around 8 ps and with a maximum value around 10^4 ps at 200 K. On the other hand, solutions with the disaccharide show a much more pronounced increase of τ_{long} , with a change of about 6-7 order of magnitude from the highest to the lowest temperature simulated. The two τ_{long} pertaining to the systems with trehalose slightly deviate from each other with decreasing temperature, with the solution with more DMSO being always slower. Both are however slower than the mixture without trehalose. It should be noted that at low temperatures the *long*-relaxation times resulting from the fits fairly exceed the duration of the longest production run, that is of 75 ns. Finally, the stretching exponents for the two processes show quite different behaviour. β_α decrease upon lowering the temperature, as expected by the fact that the dynamics is more and more stretched in time. The relaxation times starts at around 0.8 for the mixture without trehalose and around 0.6-0.7 for the other two solutions, signaling the fact that even at high temperature the presence of the disaccharide alters the dynamics. The solution with more DMSO shows a slightly more stretched relaxation, as can be seen from the fact that the exponent β for the 10 *wt%* mixture is lower than the one for the solution with a concentration of 5 *wt%* in DMSO. All the stretching exponent show a minimum at around 230 K and than increase for decreasing temperature with the exponent for the mixture with trehalose and more DMSO reaching a final value of about 0.7, higher than its high temperature value, and the other two ending at around 0.6. MCT predicts that the α -relaxation time should reach a low temperature plateau value, similar to what observed in the water-trehalose mixture (see Fig. 4.11). This non monotonic behaviour of β_α is present in all the three systems and thus can be connected to the interaction of hydration water with the protein or a combined effect of the different constituents on the water molecules. Moreover below the fragile-to-strong crossover temperature, activation processes deviate the dynamics from the one predicted by MCT and some of its predictions could result incorrect (see the next Section for a further analysis of the α -relaxation time). The stretching exponent for the slow, long time relaxation shows two different behaviour for the three systems. In the solution without trehalose β_{long} remains roughly constant and in the 0.6-0.7 range value at all the tempera-

ture, albeit with large uncertainty, with a sudden jump to 0.5 at the lowest temperature of 200 K. The solutions with the trehalose molecules show a more stretched dynamics, in fact their stretching exponents have always a lower value with respect to β_{long} of the other solution. β_{long} for the mixture with the disaccharide start at around 0.4 at 300 K, has a plateau region until 250 K and then slowly decreases with temperature, arriving around 0.2 at 200 K.

5.2.1 Relaxation times

α -relaxation

Fig. 5.9 shows Arrhenius plots of the structural α -relaxation time of hydration water of all the investigated biosolutions. Continuous black lines are best fits via power law, as predicted by MCT in the fragile region. Dashed black lines are best fits via Arrhenius law in the strong region, where activated processes play a predominant role in the dynamics of glassy systems. Results from fitting procedure are reported in Table 5.3.

System	T_{MCT} [K]	γ	E_A [kJ/mol]	T_{FSC} [K]
LYSO-TREHA-DMSO 10 wt%	206.0	2.50	41.4	225
LYSO-TREHA-DMSO 5 wt%	206.6	2.42	40.6	220
LYSO-DMSO 10 wt%	205.3	2.17	54.5	220
Bulk water	193.8	2.74	63.4	210

Table 5.3: MCT temperature T_{MCT} , γ exponent, activation energy E_A and FSC temperature T_{FSC} for the α -relaxation of hydration water of the three simulated biological solutions and for bulk water.

The relaxation time shows similar features among all the systems, with small changes in the global phenomenology of this relaxation process. The MCT crossover temperature shifts towards higher values if more solutes are added to the mixtures, in fact for the systems without trehalose it is $T_{MCT} = 205.3$ K whereas the other two solutions have a crossover temperature slightly higher, around 206 K. Differences in the T_{MCT} of these two solutions are probably due to fitting procedure and they are practically the same within the parameter uncertainty. The exponent γ shows an increasing trend with increasing concentration of solutes, passing from 2.17 for the mixture with less solutes to 2.50 with the more concentrated solution, with a major jump in the value due to the presence of trehalose. From these two

parameters that characterize the α -process in the strong region, it can be said that overall the interaction with solutes and the nearby protein surface has a weak effect on the α glassy dynamics of water upon cooling, with moderate changes if compared to bulk water (also shown in Table 5.3).

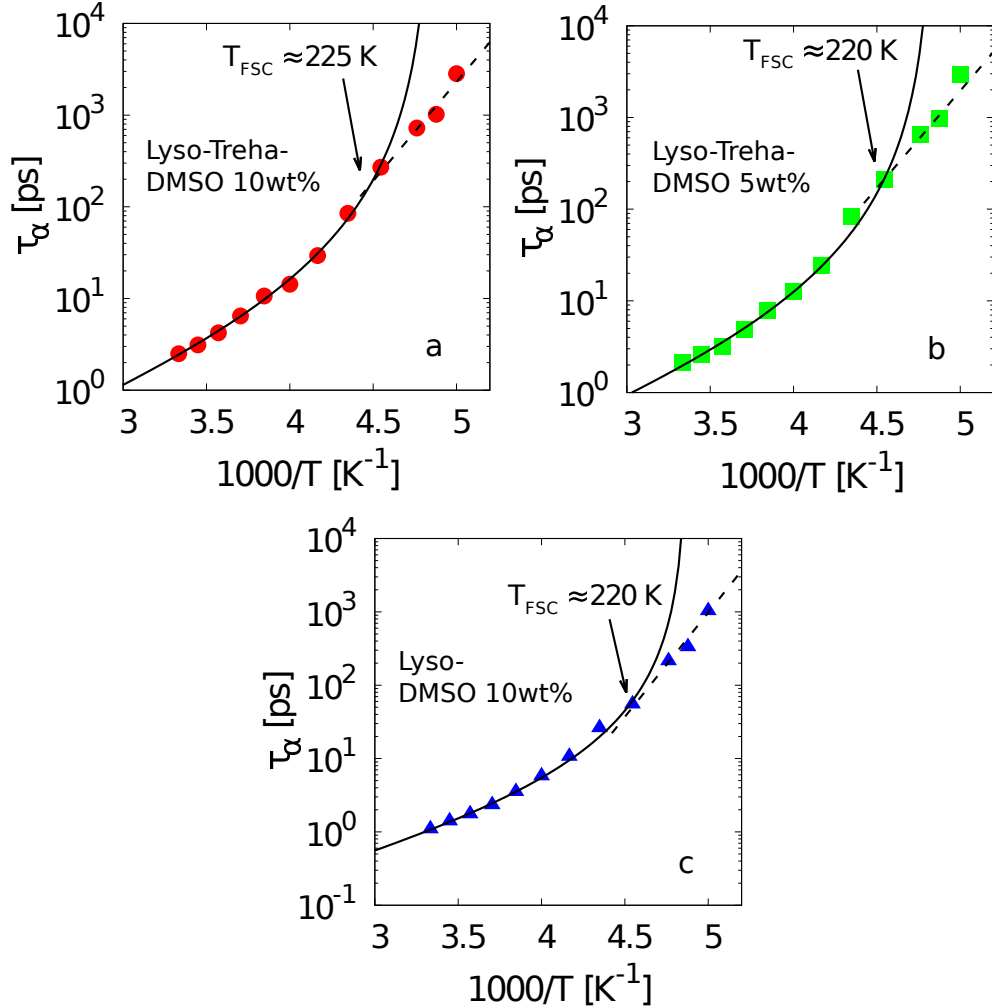


Figure 5.9: Arrhenius plot of α -relaxation time extracted by the fit procedure via Eq. 4.2 of the oxygen-oxygen SISFs of hydration water for all the three simulated solutions. Continuous black lines are best fit via a power law, as predicted by MCT in the fragile region. Dashed black lines are best fit via Arrhenius law. Panel a : system with lysozyme, trehalose and DMSO with a 10 *wt%* concentration. Panel b : system with lysozyme, trehalose and DMSO with a 5 *wt%* concentration. Panel c : system with lysozyme and DMSO with a concentration of 10 *wt%*.

The transition to a fragile phenomenology happens at the Strong-to-Fragile Crossover temperature, T_{FSC} , that is about 225 K for the solution with lysozyme, trehalose and DMSO in a concentration of 10 *wt%* and of about 220 K for the other two mixtures. It seems thus that the presence of different concentrations of solutes analyzed here have only moderate effects on the transition to an activated type of diffusion and the predominant role is played by the interaction with the surface of the protein, that is the common element to all the three solutions. It is interesting however to note that Camisasca *et al.* [99] reported a T_{SFC} for hydration water in a solution with only lysozyme of 215 K, 5 K higher than the transition in bulk water and 5-10 K lower than the transitions reported here, with solutes in the mixtures. The shift of the FSC temperature is consistent with the shift of MCT temperature towards higher value. The change to a strong phenomenology is characterized by an Energy of Activation through the Arrhenius law. From fitting procedure results that a major decrease in E_A happens passing from solutions without and with trehalose dissolved in the solvent. In fact the activation energy is $E_A = 54.5$ kJ/mol in the solution without trehalose and around 40 kJ/mol for both the systems with the disaccharide. This value is similar to what is found in the study of hydration water in a water-trehalose mixture (see Table 4.4), suggesting that a key role in this process is played by the disaccharide.

long-relaxation

Fig. 5.10 reports Arrhenius plots of the *long*-relaxation times τ_{long} along with the best fits with Arrhenius law as black continuous lines. Parameters resulting from the fitting procedure are listed in Table 5.4.

System	E_A^{HT} [kJ/mol]	E_A^{LT} [kJ/mol]	T_{SSC} [K]
LYSO-TREHA-DMSO 10 <i>wt%</i>	57.3	70.4	240
LYSO-TREHA-DMSO 5 <i>wt%</i>	45.0	73.6	240
LYSO-DMSO 10 <i>wt%</i>	29.1	55.1	225

Table 5.4: Activation energy for the High Temperature and Low Temperature regions, E_A^{HT} and E_A^{LT} respectively, and Strong-to-Strong Crossover temperature T_{SSC} for the *long*-relaxation of hydration water of the three simulated biological solutions.

The long relaxation characteristic time increases greatly upon cooling the systems, especially in presence of dissolved trehalose. Comparing the order of magnitude of τ_α and τ_{long} it is clear that at low temperature there is a neat separation in the characteristic time scale of the two processes that

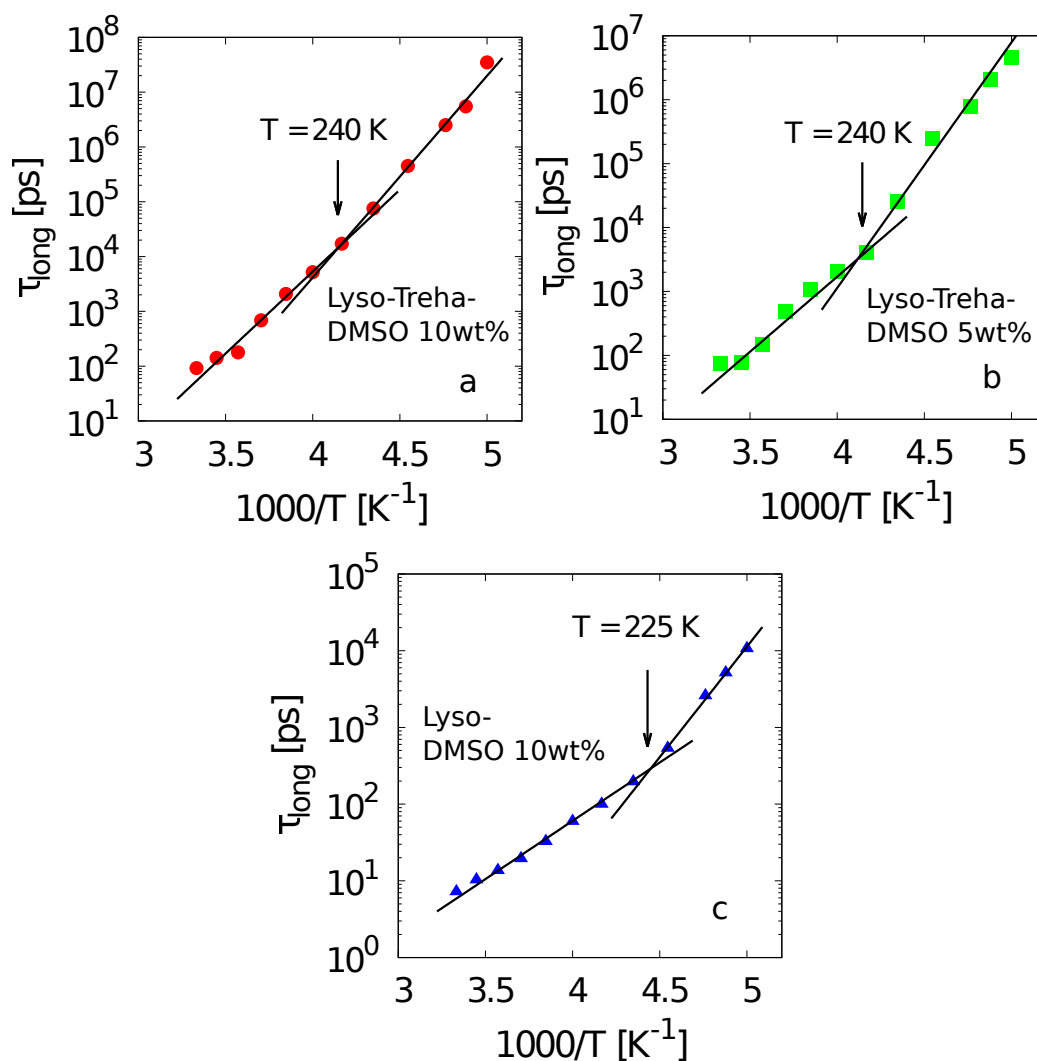


Figure 5.10: Arrhenius plot of the *long*-relaxation time extracted by the fit procedure via Eq. 4.2 of the oxygen-oxygen SISFs of hydration water for all the three simulated solutions. Continuous black lines are best fit via Arrhenius law. Panel a : system with lysozyme, trehalose and DMSO with a 10 *wt%* concentration. Panel b : system with lysozyme, trehalose and DMSO with a 5 *wt%* concentration. Panel c : system with lysozyme and DMSO with a concentration of 10 *wt%*.

drive the low temperature dynamics of water in the hydration shell. It can be said thus that they are two different processes involving different microscopic mechanisms: transient cage trapping for the α part and coupling with the surrounding chemical components, with dragging and hindering of the

motion on distinct temporal and spatial scale, for the long time part. τ_{long} reported in the plots show piecewise linear behaviour upon changing the temperature, revealing that a fit with an exponential function such as the Arrhenius law is well suited to describe them. A change in the trend with temperature is observed among all the data. This change is less marked in the more dense solution as can be seen calculating the difference between the activation energy in the high temperature and low temperature regime. In particular in both systems with the disaccharide the change of slope happens at 240 K, whereas in the systems with only lysozyme and DMSO it happens at a lower temperature, around 225 K.

The connection with the dynamics of protein, as already found in the water-trehalose systems of the previous Chapter and in water and protein [99], will be investigated in Section 5.5.

5.3 Mean Square displacement

Complementary to the Self Intermediate Scattering Function for the study of the translational dynamics of a molecule is the Mean Square Displacement. Fig. 5.11 reports the MSD for the oxygen atom of water molecules surrounding the lysozyme protein in the solution with also trehalose and 10 *wt%* of DMSO, that came out to be the system with the slowest dynamics among the three investigated in this work. It shows the expected short time ballistic regime, counterpart of the Gaussian decay in the SISF, followed by a plateau region that at low temperature extends over many decades in time. The long time regime is subdiffusive, unlike what is expected for a long time Brownian diffusion. Subdiffusivity has already been observed and briefly discussed during the study of the binary water-trehalose solutions in Chapter 4. In these multicomponent solutions other contributions can come from the different solutes present in the hydration shell. The comparison with MSDs of bulk water (see bottom panel of Fig. 3.5) shows that the plateau region starts at around 0.2 ps in both systems but last longer in the water at the interface with the protein and mixed with other solutes. Due to slower dynamics the value of MSDs reached at 1 ns is lower in the biological solutions. The small inflection observed at around 300 ps for MSD at 300 K is probably due to low statistics. MSDs for oxygen atoms of hydration water in the other two systems investigated show similar features (not shown).

To search for differences in the dynamics among the three biological mixtures, one can select the values of MSDs at a certain time and plot them as a function of temperature. Panels of Fig. 5.12 report the values of MSDs at

$t = 200$ ps, that is outside the plateau region also for the lowest temperature simulated. The values of MSD coming from the system without trehalose result to be the highest among all the systems, as can be expected given the fact that that solution is the one with faster dynamics and where water molecules are able to move to farther distances due to the lack of trehalose that hinders their motion. The other two systems show comparable values of the distances explored in that amount of time, with the MSDs of the solution with more DMSO being slightly smaller. The enhancement in the diffusive properties upon heating the systems is hampered by trehalose and to a lesser extent also by DMSO.

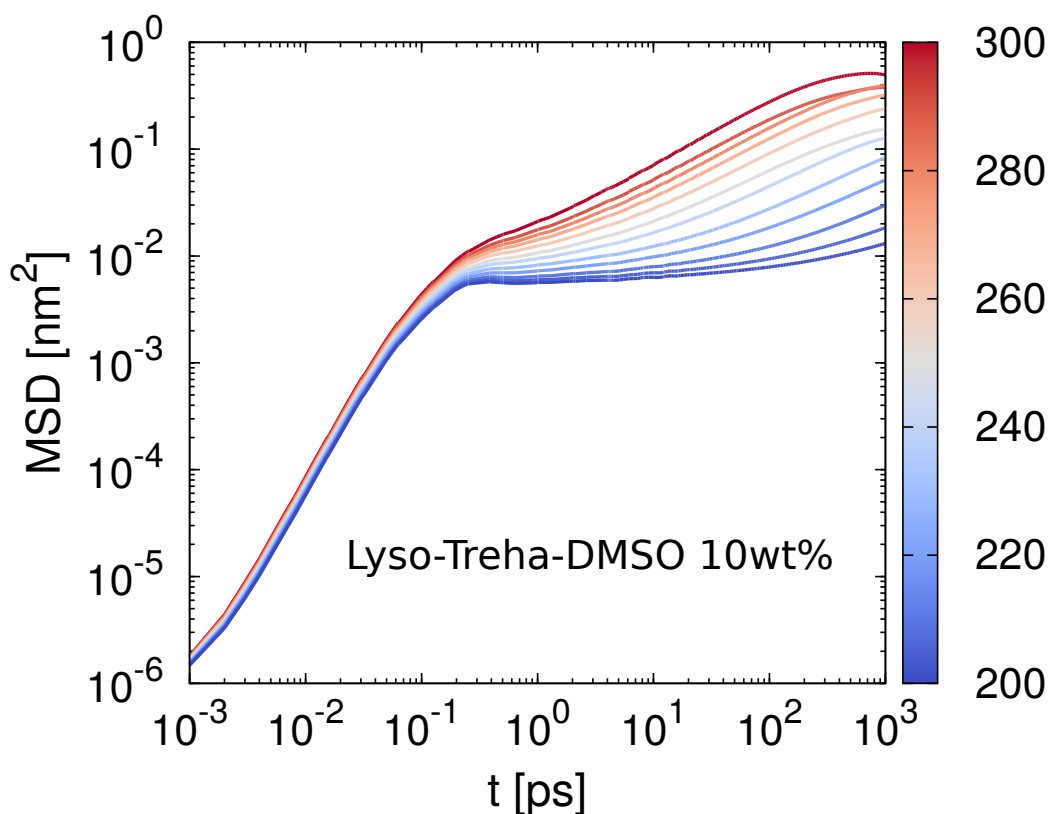


Figure 5.11: Mean Square Displacement for the oxygen atom of the hydration water as a function of the temperature for the system with lysozyme, trehalose and DMSO with a concentration of 10 *wt%*.

A change in the trend with temperature of reported quantities is visible in all the plots. Black lines as guide to the eye help to recognize the temperature at which the transition happens. When the trehalose is present, the change

of slope is near 230 K, independently of the concentration of DMSO. In the solution without the disaccharide the transition happens at temperature slightly below 230 K.

Although here the statistics is less good and a precise location of the crossover is not possible, here too this crossover seems to be connected to the crossover of the long relaxation time τ_{long} .

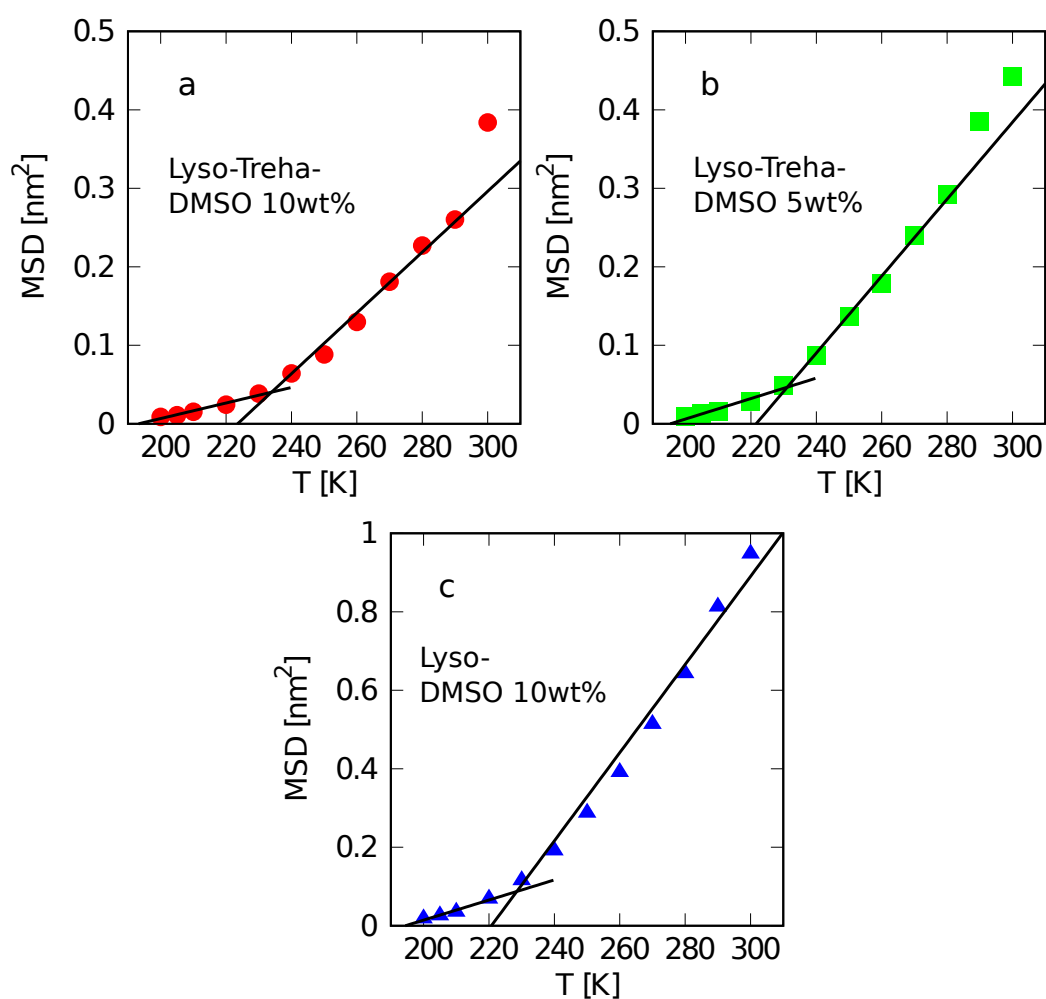


Figure 5.12: Value of the Mean Square Displacement at $t = 200$ ps for the oxygen atom of the hydration water as a function of the temperature. Panel a : system with lysozyme, trehalose and DMSO with a concentration of 10 *wt%*. Panel b : system with lysozyme, trehalose and DMSO with a concentration of 5 *wt%*. Panel c : system with lysozyme and DMSO with a concentration of 10 *wt%*.

5.4 Lysozyme-Water solution

A comparison with the work of Camisasca *et al.* [99] on MD simulations of a mixture of SPC/E water and lysozyme protein is very useful to isolate the contribution to the dynamics of water molecules in the hydration layer of the protein coming from the presence of DMSO alone in the solution.

Fig. 5.13 report the oxygen-oxygen SISFs of hydration water of lysozyme for selected temperature in both the systems with and without DMSO.

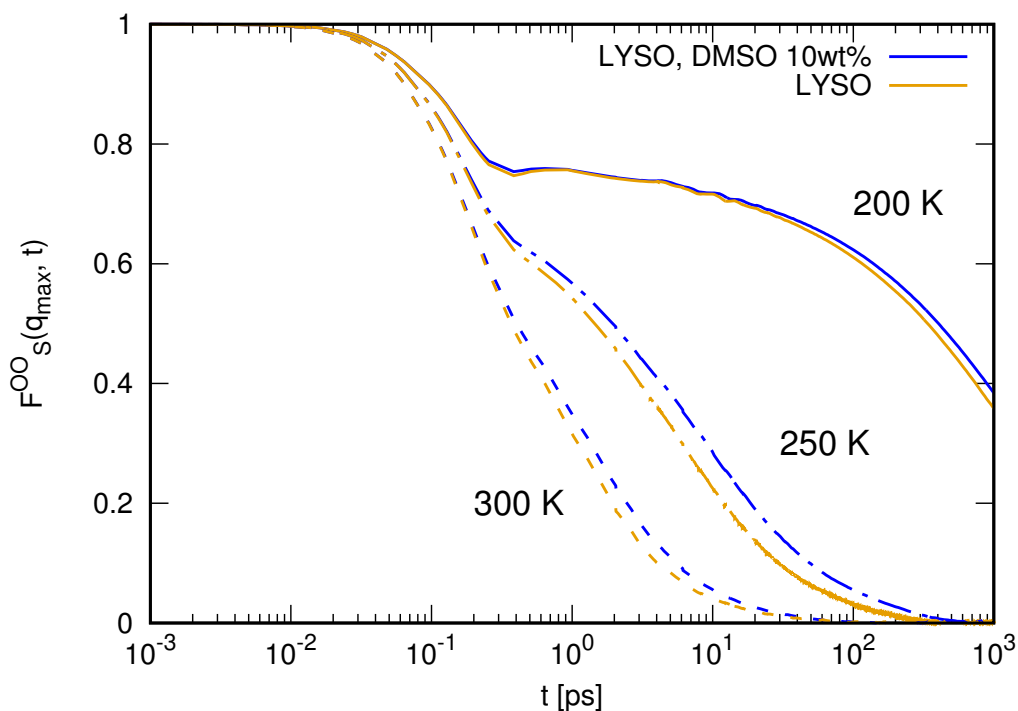


Figure 5.13: Oxygen-oxygen SISFs for selected temperatures of lysozyme hydration water in the system with lysozyme and DMSO in a 10 *wt%* concentration and in a system with protein and water studied by Camisasca *et al.* in Ref. [99].

Correlators show similar shapes for corresponding temperature. At short time curves perfectly match and then differentiate starting from 0.3 ps. The height of the plateau at 200 K is equal in the two systems and deviations arise at longer times.

Globally speaking the dynamics of hydration water in presence of dimethyl sulfoxide result slower and more stretched in time in comparison with the

case with no DMSO.

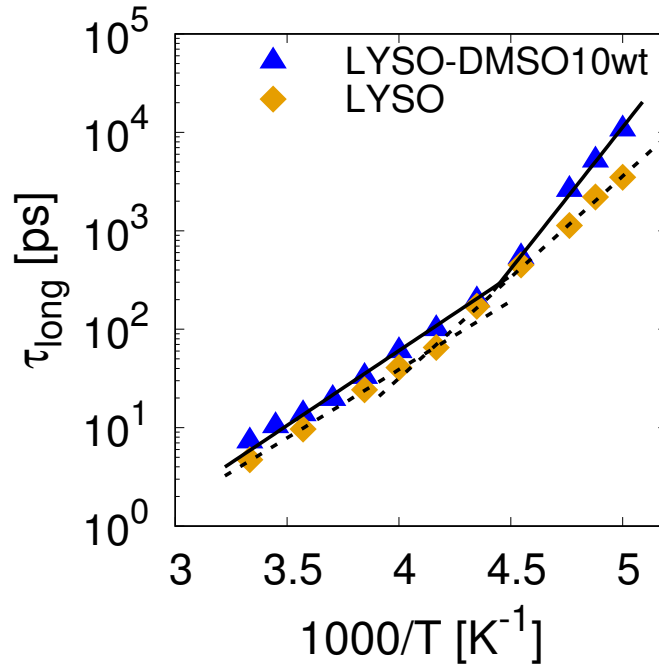


Figure 5.14: Arrhenius plot of the long-relaxation time extracted by the fit procedure via Eq. (4.2) of the oxygen-oxygen SISFs of hydration water for the system with lysozyme and a 10 wt% concentration in DMSO and for the system with lysozyme studied by Camisasca *et al.* in Ref. [99]. Continuous and dotted black lines are best fit via an Arrhenius law.

An interesting difference in the long time behaviour of the two systems arise in the study of the *long*-relaxation time. In Fig. 5.14 τ_{long} coming from fitting procedure of the SISFs via Eq. (4.2) is reported as a function of the temperature in an Arrhenius plot. The relaxation times pertaining to the two mixture are comparable in the order of magnitude but the solution with DMSO is always slower, as seen also with a comparison of the SISFs at visual level. Also in the system with no DMSO a change in the trend of τ_{long} is observed but in that case the Strong-Strong Crossover happens at around 240 K, that is 15 K above the one observed with DMSO and exactly where the same transition is in the two systems with DMSO and trehalose. It seems thus that DMSO shifts the transition to lower temperature with respect to the case with the protein alone but the presence of trehalose has the opposite effect to restore the original location of the crossover also if DMSO is present

in the same concentration.

Using the value of the MSD of the hydrogen atoms of the lysozyme protein, Camisasca *et al.* found a perfect agreement between the PDT and the SSC transition observed in the long relaxation time: both are located at $T = 240$ K.

5.5 Protein Dynamical Transition

To investigate the coupling between the motion of water molecules at the interface with lysozyme and the motion of the protein itself, the Root Mean Square Displacement of hydrogen atoms of the side chains of lysozyme has been calculated.

Root Mean Square Displacement (RMSD) is defined as

$$RMSD = \sqrt{\frac{1}{N} \sum_{i=1}^N \delta_i^2} \quad (5.1)$$

where δ_i is the displacement of the atom i from a reference position. The RMSD quantifies the fluctuations of selected atoms with respect to a reference position.

Prior to the calculation of the RMSD it is necessary to remove the global translational and rotational motion of the macromolecule using a least-squares fitting procedure to align the protein to a reference structure in order to minimize the distance of selected groups (see Fig. 5.15 for a pictorial representation of this procedure). After this alignment the displacement δ_i can be calculated.

In this work at each time step the structure of lysozyme is compared to the structure it had at the beginning of the production run. Least-square fitting is performed on the atoms of the backbone, that is the core structure that reside in the internal part of the protein and is the less mobile if compared to more external structure, and only the translational component of the motion has been removed. Hydrogen atoms of side chains have been chosen because of their mobility and because they interact the most with surrounding water molecules and are thus well suited to study how the internal motion of protein couples to the motion of surrounding molecules. RMSD calculated at each time step has been averaged over all the configurations in the last 10 ns of the production run. Results are reported in Fig. 5.16

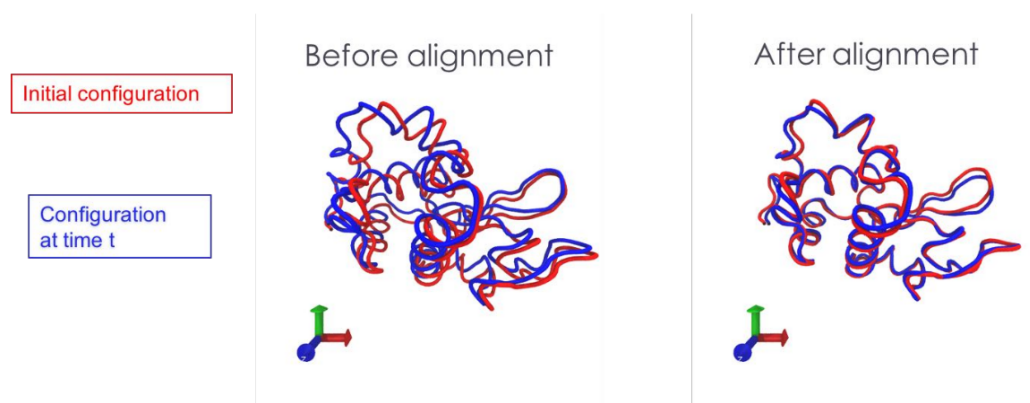


Figure 5.15: Alignment of protein structures.

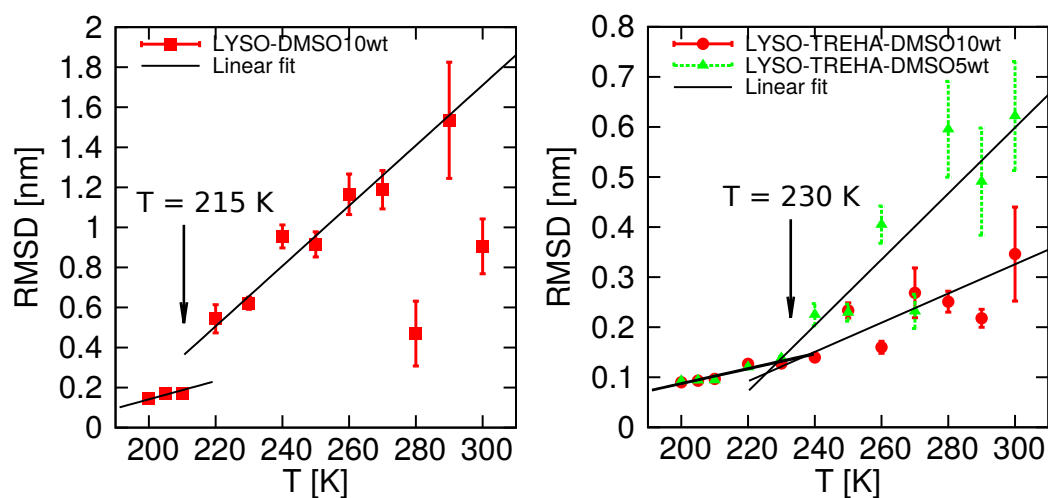


Figure 5.16: Root Mean Square Displacement of the hydrogen atoms of the side chains of the lysozyme protein. Left panel refers to the solution without trehalose, right panel refers to the two solution with trehalose molecules. Superimposed black lines are linear fits intended as guide for the eye.

RMSD of the hydrogen atoms of lysozyme in the presence of DMSO are reported in the left panel. The signal is noisy especially at higher temperatures, with clear outliers points at 280 K and 300 K, but an enhancement in the amplitude of the fluctuations is evident at around 215 K. This is usually recognized as a signal for a Protein Dynamical Transition.

In an experimental work on dynamic transition of proteins in different protein solutions, Réat *et al.* [135] studied also the properties of a xylanase protein immersed in mixture with high concentrations of DMSO (40% and 80%).

They found a PDT at around 220 K, that is compatible to what is found in the present work. Moreover the position of the PDT seems to be unaffected by difference in the concentration of the soluted DMSO.

If the trehalose is present in the mixture, the PDT results shifted towards higher temperatures. In particular the change of slope is at around 230 K in both the systems with the disaccharide. This is compatible to the fact that trehalose molecules form a matrix around the protein, hampering its natural motion upon heating. The difference in concentration of DMSO from 5 *wt%* to 10 *wt%* has minor effect on the position of the transition, that is only slightly shifted to higher temperature but still very close to 230 K. DMSO has instead an impact on the fluctuations of the protein, that results diminished by a factor 2 in the more concentrated solution despite the fraction of DMSO molecules in the hydration layer are roughly the same in the two solutions with also trehalose (see panel a of Fig. 5.4). It is interesting to note that the change of slopes presents in the RMSDs of both the solutions with trehalose happens roughly at the same temperature (230 K) where the change of slopes in the MSDs of oxygen atoms of hydration water is located (see top panels of Fig. 5.12). The enhancement of the fluctuations of both these two components of the solutions can be connected and due to the strong mutual interaction. In the box without trehalose the change of slopes happens at two slightly different temperatures and thus the connection between them is less evident.

The observed PDTs are different from both the Strong-to-Strong Crossover temperatures calculated with the τ_{long} analysis and the change of slope in the MSDs of oxygen atoms of hydration water, thus a decisive evidence of the connection of a strong coupling in the motion of protein and surrounding water is lacking. However given the fact that the solutions studied in this work are made of different components with complex interplay between them and that the change in the dynamical behaviour observed in the different quantities happens in the same temperature range and the crossover temperatures are consistently ordered, the observed phenomenology can be interpreted as a strong hint of the presence of a connection between the motion of a macromolecule and of surrounding water.

A more in deep analysis is needed to further clarify this point.

5.6 Hydrogen Bonds

In this Section hydrogen bonds properties of hydration water are analyzed through structural quantities such as the distributions of water-water HBs per water molecule, the angular distribution function of the angle γ and

the distribution of the Orientational Tetrahedral Order parameter q . For details on these quantities and on the definition of hydrogen bond used, see Section 3.8.2.

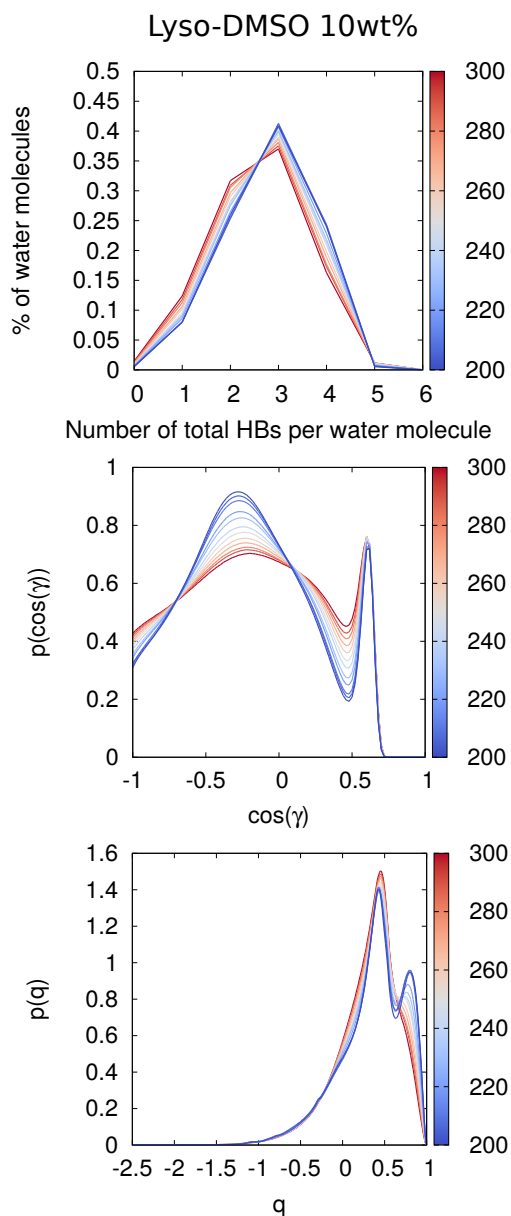


Figure 5.17: Top panel: fraction of water molecules with a given number of Hydrogen Bonds. Middle panel: distribution of $\cos(\gamma)$. Bottom panel: distribution of the Orientational Tetrahedral Order parameter. All the plots refer to lysozyme hydration water of the system with lysozyme and DMSO with a concentration of 10 wt%.

Fig. 5.17 refers to the solution with lysozyme and DMSO. From the plot on the top it can be seen that most of the water molecules tend to form three HBs with other water molecules and this tendency is enhanced upon cooling (the peak height increase with decreasing temperatures).

The fraction of water molecules with three and four HBs increases as the temperature is lowered at the expense of the fraction of water molecules with only one and two HBs. Thus the HBs network becomes more structured at low temperatures. No water molecules form more than five hydrogen bonds. The distribution of $\cos(\gamma)$ reveals that globally the hydrogen bonded water molecules tend to recover a tetrahedral structure upon cooling as can be seen from the increase of the main peak, albeit it remains always smaller than the corresponding peak seen in bulk water (see middle panel of Fig. 3.9). The second peak around 0.6 due to interstitial water is stable upon cooling. The local tetrahedral structure results strongly altered as it is evident from the fact that the distribution of q presents a peak below $q = 0.5$ that slightly decrease and moves towards lower values when the solution is cooled. A shoulder presents around $q = 0.6$ at high temperatures becomes a small peak at $q \simeq 0.8$ at low temperatures.

Fig. 5.18 allow to compare side by side the differences between the water HBs properties in the two solution with trehalose (left column for the solution with a concentration of 10 *wt%* in DMSO, right column for the solution with a 5 *wt%* concentration in DMSO). In both cases the structure of the water hydrogen bonds network results even more altered than in the case without the disaccharide. In particular most of the water molecules tend to form only two hydrogen bonds at high temperature with a small increase of the fraction corresponding to three HBs at lower temperature. When the temperatures is lowered the fractions of water molecules with zero, one and two HBs with other water molecules diminish by roughly the same quantity in the solution with more DMSO, whereas in the other one the reduction is greater in the fraction of molecules with 1 HBs. On the contrary in both solutions the increase in the fraction with three HBs is greater than the one representing the population with four HBs. There is also a small population of water molecules that is not bonded to any other water molecule. From the distribution of $\cos(\gamma)$ appears that the tetrahedrality is slightly enhanced upon cooling but the contribution coming from tetrahedrally arranged molecules is of the same order of the one coming from interstitial water being this water much less tetrahedral than bulk water overall. The change in the local tetrahedral disposition is clear also by looking at the distribution of the parameter q . The main peak is around 0.4 and at higher values of the parameter only a second small peak at low temperature appears, being a small shoulder at higher temperatures while 1 would correspond to perfect tetrahedrality.

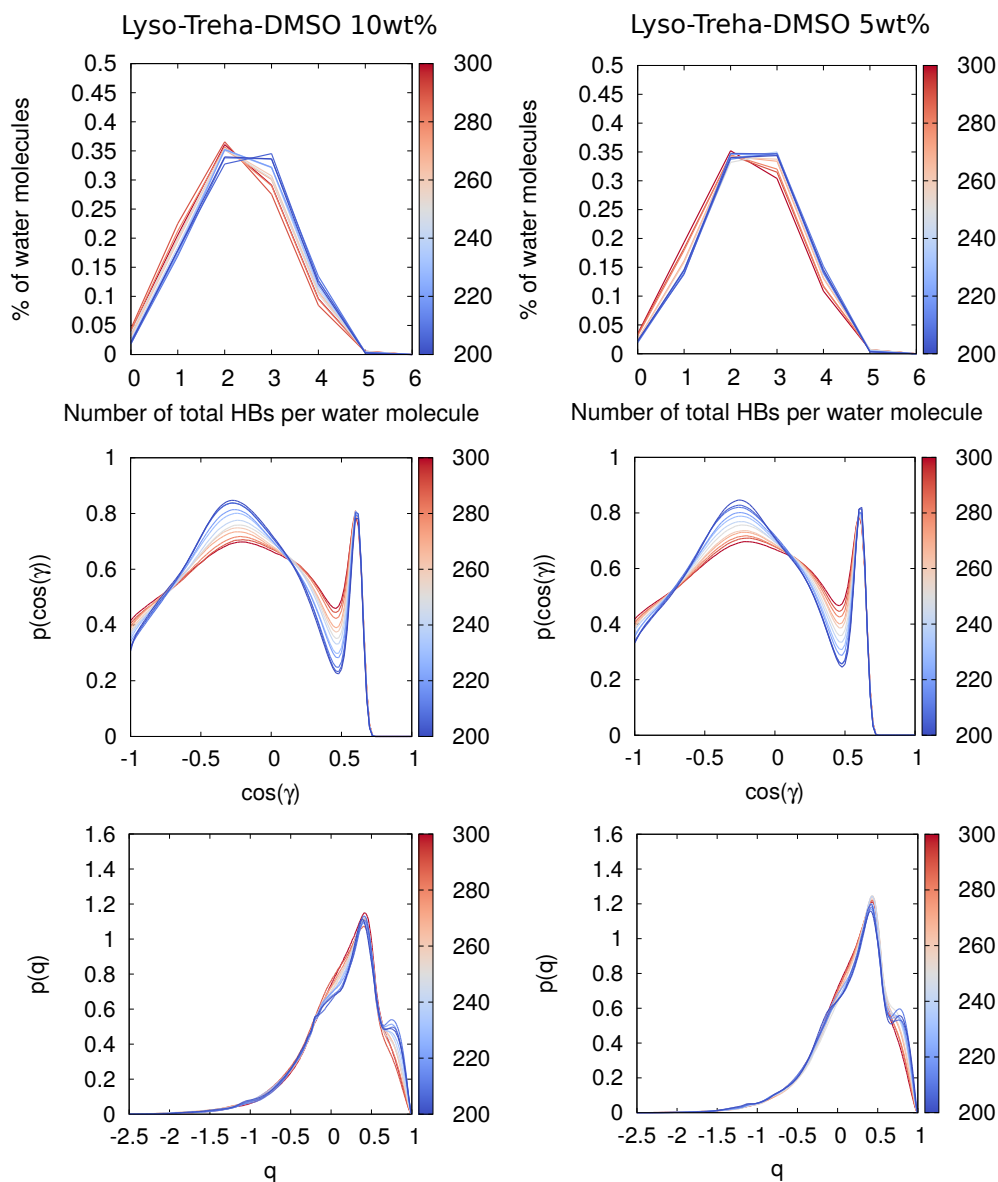


Figure 5.18: Top panels: distributions of the number of Hydrogen Bonds formed per water molecule. Middle panels: normalized angular distribution functions $p(\cos(\gamma))$ of the angle between the oxygens of three nearest neighbour water molecules. Bottom panel: normalized distribution of the Orientational Tetrahedral Order parameter q . Left panels refer to the solution with lysozyme, trehalose and DMSO with a 10 wt% concentration, right panels refer to the solution with lysozyme, trehalose and DMSO with a 5 wt% concentration.

The curves for different temperatures overlap and show a non monotonic behaviour upon cooling the solutions.

To better identify the differences between the HBs network in the three mixture and how they change upon cooling, Fig. 5.19 report the fraction of water molecules with a given number of Hydrogen Bonds (top panel), the distribution of $\cos(\gamma)$ (middle panel) and the distribution of the Orientational Tetrahedral Order parameter (bottom panel) for the highest and the lowest temperature simulated, $T = 300$ K and $T = 200$ K respectively (left column and right column).

The distribution of the fraction of water molecules hydrogen bonded with other molecules with a given number of bonds is different between the solutions with and without the disaccharide. If the trehalose is present the main peak is at 2, whereas without trehalose it is at 3. Upon cooling the fraction of water molecules hydrogen bonded three or four times increase in all the solutions. Comparing the curves for the systems with trehalose and DMSO, small differences arise upon cooling in the fractions of molecules with one, three and four HBs. This is probably due to the presence of more DMSO in the hydration layer that bonding with water diminish the number of HBs between water molecules (see Fig. 5.4 for the relative fraction of DMSO and trehalose molecules in the hydration layer). In the mixture with trehalose some water molecules make no bonds with other water molecules, either because of steric constraint and because they are fully bonded with other constituents of the mixture, most likely trehalose molecules.

The distributions of the cosine of the angle between three oxygen atoms γ reveal small differences among the three solution at the highest temperature studied. It is interesting to note that the peak at high values of $\cos(\gamma)$, pertaining to interstitial water, is the highest point in the distribution, while in bulk water it is of the same order of the second, broader peak presents at around -0.3 (see Fig. 3.9). Upon cooling, solutions with trehalose differentiate from the one with only DMSO. In particular the peak due to interstitial water diminish more in the solution without the disaccharide and in the solution with trehalose and more DMSO, that is that the contribution coming from interstitial, non ordered water is stronger in the solution with less DMSO. The peak at lower value of the cosine is higher and sharper in the solution with only DMSO while it is broader, smaller and shifted to higher values of the cosine in both the mixture with trehalose. The curves coming from the solution with 5 wt% concentration in DMSO is slightly shifted towards higher values of $\cos(\gamma)$, pointing out a more distorted HBs network. Focusing on the local tetrahedral distribution of water oxygen atoms, the distribution of the parameter q is broader and with a higher shoulder towards low values of the parameter if the concentration of DMSO is higher.

The difference in the local tetrahedral order between the two mixture with trehalose is even more evident at low temperature (left panel of the bottom row of Fig. 5.19). The peaks of the green curve (the one coming from the system with 5 wt% DMSO) are higher and at higher values of q , whereas the left tail is lower than the one of the other mixture with trehalose. The solution without the disaccharide is the most ordered one, with a fast decaying left tail and two well defined peak at high values of the parameter q , albeit the one near 1, value associated with a perfect tetrahedral disposition, is the smallest one.

Concluding it can be said that the interactions with the surface of the protein and with the other constituents of the mixture strongly change the properties of hydrogen bond network formed by water molecules in the hydration layer. Differences increase with increasing concentration of DMSO and trehalose soluted and are enhanced upon cooling. Even a small increase in the concentration of dimethyl sulfoxide produce noticeable effect on the characteristics of how the water molecules are bonded with each other. Trehalose favors disorder, DMSO alone favors more local order at low temperature and therefore likely LDL.

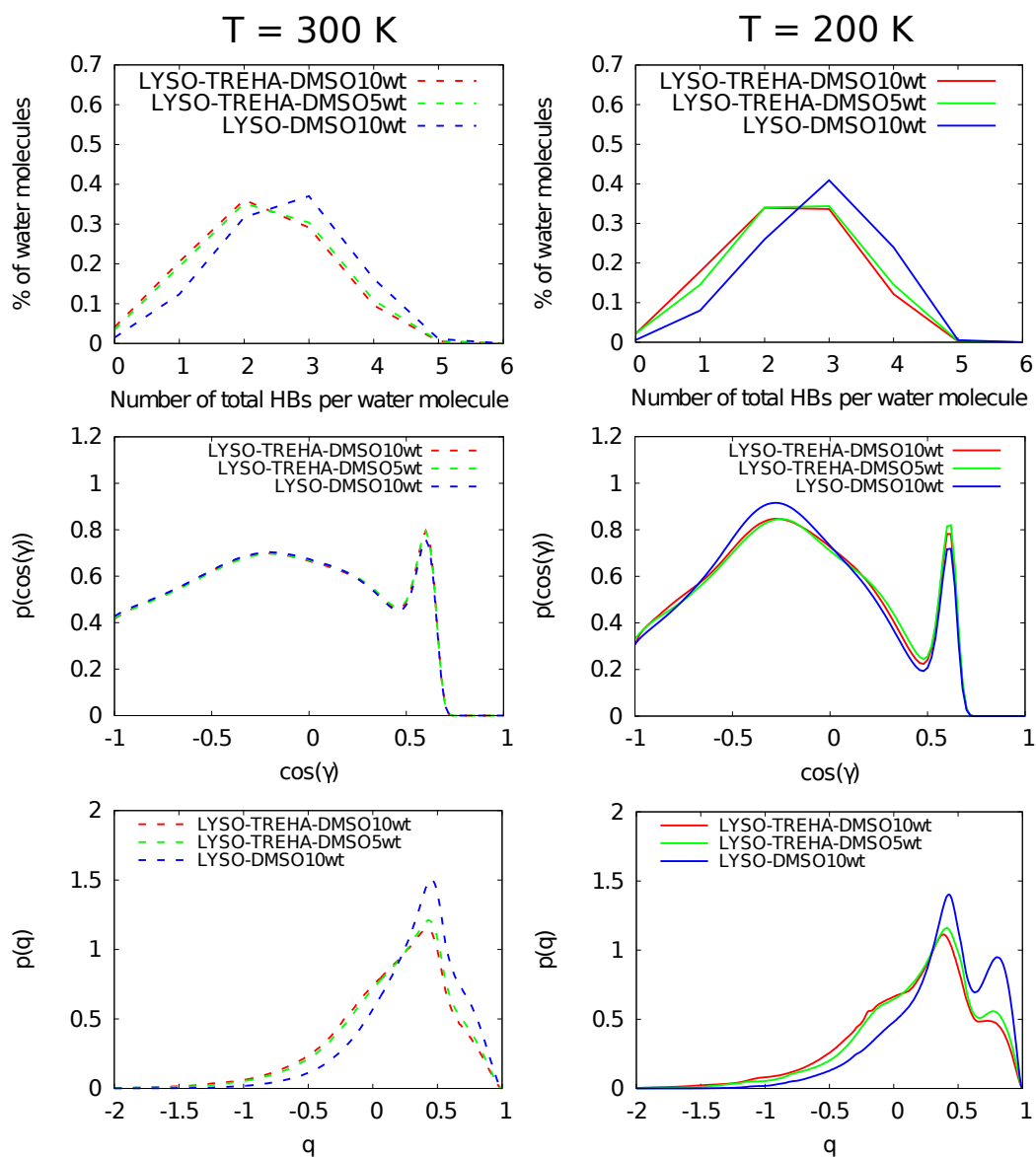


Figure 5.19: Comparison of the number of Hydrogen Bonds per water molecule (top panels), angular distribution function $p(\cos(\gamma))$ (middle panels) and distribution of the Orientational Tetrahedral Order parameter q (bottom panels) between hydration water of lysozyme in the three simulated biological solutions. Left panels refer to 300 K, right panels to 200 K.

5.7 Conclusions

Using MD simulations the dynamics and structure of water in the hydration layer of the lysozyme protein in presence of different concentration of DMSO and trehalose have been studied upon cooling. The interaction with the surface of the protein and with the other solutes change how the water behaves and the difference with respect to bulk water is even more evident at low temperature.

From a dynamical point of view, hydration water results to be slower and with a stretched dynamics with respect of bulk water at the corresponding temperature. It however retains the dynamics seen in bulk water, typical of a glassy system. In particular the short time motion and the α -relaxation phenomenology result weakly altered by the presence of other components in the mixture. SISFs show an important additional relaxation process that takes place at long times and is very slow. This process has been observed in hydration water of other biomolecules [99, 100] and recently in colloids [117] and happens at characteristic time scale that is orders of magnitude greater than τ_α . Thus, especially at low temperature the α -relaxation and the *long*-relaxation are two well defined and separated processes, driven by different microscopic phenomenology: cage effect for the α part, slow global relaxation and coupling with the motion of the components of the systems (protein and trehalose) for the *long* part. The slowly decaying correlators of hydration water are well described by the functional form composed by a Gaussian term, that account for the initial short times and fast decorrelation, and two stretched exponential with relative characteristic times and stretching exponents. A shift of the MCT crossover temperature and of the FSC temperature towards higher values has been observed, with differences arising from the concentrations of the DMSO and trehalose present in the mixture. τ_{long} steeply increases upon cooling, with final value at 200 K of the order of 10^7 ps for the solutions with trehalose and 10 wt% DMSO. Arrhenius plot of τ_{long} revealed a change in the trend of this quantity as a function of the temperature. In particular the change of slope with relative change in the activation energy has been localized at 225 K for the solution with only DMSO at at 240 K for both the solutions with also trehalose.

A change on its behaviour with changing temperatures has been observed also in the values of the MSDs of oxygen atom of hydration water have at $t = 200$ ps. The crossover temperatures are locate in a small range around 230 K and their relative order is the same of the Strong-to-Strong Crossover observed in the temperature trend of τ_{long} .

A comparison with dynamics of hydration water in an aqueous mixture with lysozyme protein was used to disentangle the contribution coming from the

DMSO from the one due to the interaction with the surface of the protein. Confronting the oxygen autocorrelator revealed that the addition of a small percentage of DMSO in the solution, of the order of the ones used for cryopreserving purpose, change the long time dynamics of hydration water, slowing it down. The Strong-to-Strong crossover of the *long*-relaxation time is located at 240 K. Thus it appears that the presence of DMSO moves that transition to lower temperatures. The $T = 240$ K crossover is restored once to DMSO trehalose is added.

Further analysis are needed to clarify the role of the combined interactions of the different solutes with water (excluded volume effect, steric constraint, water-solute hydrogen bonds).

In a pure solution it has been shown that fluctuations in the structure of a macromolecules, such as a protein, are connected with the long time regime of the dynamics of nearby water [99]. To enquire on this finding for our systems, the RMSDs of hydrogen atoms of the side chains of lysozyme have been calculated and plotted as a function of the temperatures. A PDT was revealed at circa 215 K for the solution with DMSO and no trehalose. This temperature is close to the temperature where a PDT was located experimentally in a solution of DMSO and xylanase protein [135]. It would be interesting to study systems with different concentration of DMSO in search for a threshold concentration above with the fluctuations of the protein result altered.

The presence of trehalose moves the PDT to higher values, near 230 K, closer to the PDT found by MD simulations in a mixture of pure water and lysozyme.

The PDT observed in this Thesis are lower than the dynamics crossover temperatures derived from the motion of hydration water, but their relative order is the same.

There is clearly a connection between the fluctuations of an hydrated macromolecule and the long relaxation process observed in hydration water but needs more in deep analysis to be further clarified.

Hydrogen bonds analysis of hydration water revealed marked changes in the properties of the HBs network due to the interaction with all the different components of the solutions.

The fraction of water molecules with a given number of HBs and their relative arrangement are all altered in the biological solution. This effect is even more evident at low temperature and for high concentration of DMSO and trehalose. Comparing the distribution of the quantities analyzed it results clear that a major role in the modification of the network of HBs between

water molecules is due to trehalose. However comparing data coming from the mixture with 5 *wt%* and 10 *wt%* concentration in DMSO is evident that even that small change in the concentration produces noticeable differences on how the hydration water are hydrogen bonded.

Concluding, from all the results obtained in the present work, it can be said that both dimethyl sulfoxide and trehalose act as cryoprotecting agents in that they modify the properties of hydration water of the lysozyme protein, both from a dynamical and from a structural point of view.

Chapter 6

General conclusions

This work aimed at the description of supercooled water in biological solutions, with focus on the population of water molecules that resides in the hydration layer of the biomolecule under investigation.

Using highly optimized software to perform MD simulations¹, five systems have been studied. Two of them are aqueous solutions of trehalose with different concentration of the disaccharide. The other three are composed by water, lysozyme DMSO and trehalose in different combinations.

To extract the observables of interest from the generated trajectories, different tools have been used. In particular the study of the translational dynamics (SISFs and MSDs) of hydration water and the properties of the water-water hydrogen bonds has been carried out with in-house software capable to exploit the multicore architecture of the machines in the Roma Tre High Performance Computing cluster. The code for the HBs analysis has been written with the use of the OpenMP shared memory API (see Appendix A). This enabled the use of multiple computing cores to complete a single analysis task, with a great boost in the performance.

Trehalose has been found to be very effective in modify the dynamics of water molecules at its interface. The structural α relaxation typical of glassy system is present also in water population in the hydration layer, with a slight modification of the phenomenology seen in bulk water. In particular the Fragile-to-Strong Crossover is preserved, with a shift of the temperature of transition to an higher value. This suggests that aqueous solutions can be a feasible way to enter the no man's land and study anomalies of water in a region where experiments on bulk water are difficult. In addition to the α relaxation, a slow relaxation has been observed in the long time region of the

¹The version of GROMACS used in this work has been compiled for the use of machines with multicore architecture and GPGPU acceleration.

Self Intermediate Scattering Functions. This new feature of the correlator is connected with the interaction of water molecules with trehalose molecules and it is not present in bulk water. The study of this new relaxation process leads to a connection with fluctuations of the clusters formed by trehaloses. This hypothesis has been further corroborated by the study of the Mean Square Displacement of the oxygen atom of hydration water and of selected atoms of trehalose. A complete dynamical coupling between aggregates of trehalose molecules and water molecules at the interface is observed. From the study of these two quantities a dynamical transition happens at around 250-260 K, akin to what is observed in hydrated protein upon heating. This is the first evidence of a dynamical transition in a self-assembled macroaggregate composed of small biomolecules.

Trehalose molecules have also a strong impact on the formation of water-water HBs. In particular a change in the number of HBs per water molecule has been observed. Moreover the nearby presence of trehalose molecules change also the spatial arrangement of water molecules, with a modification of the typical tetrahedral structure of the HBs network observed in bulk water.

These evidences are all connected to trehalose behaving as a good cryoprotectant, it is able to hinder the motion of surrounding water molecules and to hamper the formation of ice crystal upon cooling.

Analysis of the MD simulations concerning the composite mixture of DMSO and trehalose show effects on both the dynamics and structure of water molecules in the hydration shell of lysozyme protein.

The study of the oxygen-oxygen Self Intermediate Scattering Function revealed the presence of an α -relaxation process that is characteristic of the glassy dynamics of a supercooled liquid and an additional relaxation process that takes place on longer time scale. The phenomenology typical of glassy water is thus retained also in these multicomponent systems, although a shift towards higher temperatures is observed in the MCT temperature and in the crossover temperature from a fragile to a strong region, where activated processes drive the dynamics of water. The shift is slightly more consistent in solutions with trehalose. The characteristic long relaxation time shows a strong to strong crossover upon changing the temperature. This feature has been observed in all the biological solutions under investigation. The crossover temperature depends on the composition of the mixture: it is higher in the two solutions with trehalose. Comparison with a precedent work on MD simulations of a binary water-lysozyme solution shows that the crossover in the trend of τ_{long} is present also in the absence of other solutes but the addition to the mixture of different compounds changes the temper-

ature at which the crossover happens.

To enquire on the hypothesis of a coupling between the large time motion of a protein and that of the surrounding water, the MSDs of the oxygen atoms of hydration water and the RMSD of hydrogen atoms of the side chains of lysozyme have been calculated. Crossover temperatures are present in all these quantities and appear compatible with each other and with crossover temperatures extracted from the long relaxation process.

From a structural point of view, the water HBs network results strongly altered by the presence of the different chemical compounds, with a major effect due to trehalose. This is probably due to the strong interaction with other components (excluded volume effects and hydrogen bonding with protein and trehalose) and to the lower concentration of DMSO investigated in this work, that is the one commonly used in cryopreserving application. Nonetheless, comparing structural quantities pertaining to the two solutions with different concentration of DMSO revealed noticeable changes in the HBs network, confirming its effect in altering the structure of surrounding water.

DMSO and trehalose are important cryopreserving agents that impact the behaviours of biological solutions in several ways. Dynamics of hydration water shows a slow and long time structural relaxation in addition of the usual bulk glassy dynamics. The PDT is preserved in presence of DMSO and trehalose and its position results modified depending on the relative concentration of these two solutes. In particular trehalose seems to restore the dynamical behaviour of hydration water in a simple water-lysozyme mixture. The shift in the temperature of all the dynamical quantities studied is consistent.

Structure of water around lysozyme is altered by the presence of both the cryopreserving agents.

A strong dynamical coupling between protein and surrounding water appears and further investigations will allow a better characterization. Further studies will be also useful to disentangle the relative contribution coming from the different components of the biological solutions studied.

From the results reported in this work, the composite DMSO-trehalose mixture appears to be useful for cryopreservation in that the combined action of both the cryopreserving agents can be exploited.

Appendix A

Parallel Implementation of HBs analysis code

In this Thesis I have used in-house parallel programs for the calculation of $F_S(q_{max}, t)$ and MSDs and the GROMACS package to run MD simulations on machines with multicore architecture.

To study the hydrogen bonds network of water I had to implement a new parallel code. The analysis of the water-water hydrogen bonds properties is in fact computationally very demanding. For each molecule the software has to loop over all the other molecules and check if the conditions for the formation of an hydrogen bond are satisfied, thus the number of operations is of order N^2 , where N is the number of molecules to check.

It is useful to parallelize the code for this type of analysis in order to share the work on many computing units and diminish the time spent for the computation.

Analysis of the HBs network properties presented in this work where carried out with a C code that has been parallelized using OpenMP, a shared memory Application Programming Interface.

The main loop over the particle is the part of the code that is the most time expensive so it was the part that was parallelized. The software splits the number of particle in the system among the number of threads that work independently from each other. After all threads have finished the results are putted together and normalized. OpenMP uses shared memory, that is that different thread access data stored in the same position, this allow to reduce the memory occupied by the program. Appropriate care must be taken in order to use shared memory for the storage of positions of the particles in the system and private memory to store the temporary results of the computation of each single thread.

The code for the analysis of hydration water is composed by an additional loop over the particles that checks if each particle is within a given distance from a reference set of particle. This section of the code has been parallelized separately from the main loop, doing so the main loop has to check for the formation of an hydrogen bond on a subset of particle $N_{in} < N$, further reducing the time taken for the computation.

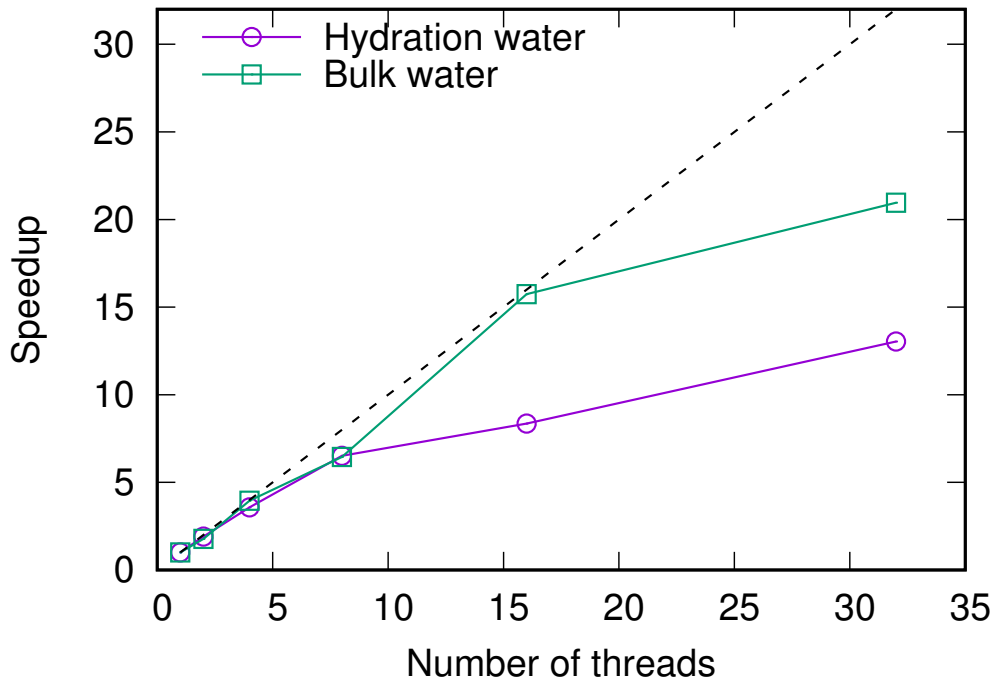


Figure A.1: Speedup as a function of threads for the analysis of water-water HBs properties for hydration water and bulk water. Dashed black lines represents an ideal linear scaling with the number of thread.

Fig. A.1 reports the speedup in the time execution of the code in the case of hydration water and bulk water (where the initial loop that checks for the distance condition is not present). As can be seen the speedup is significant and this allows to run this type of analysis in a much shorter time and to increase the statistics.

It should be noted however that the time taken from the software to complete the analysis doesn't scale linearly with the number of threads used. This could be due to a number of factors:

- Parts of the code that are not parallelized.

- Saturation of the memory bus.
- Saturation of the cache memory.
- Use of logical cores¹.

Some of these points could be addressed in order to increase the efficiency of the code, for example rewriting the loop in order to use cache and data access in a more efficient way, or binding the threads to physical cores.

However even with software that doesn't scale perfectly with the number of threads, the implementation of a parallel code has permitted to reduce significantly the computation time.

¹The software has been run on machine with Intel Xeon CPU with Hyper-Threading technology that double the number of computing units seen by the system. However the logical cores are not as performant as the physical one. In particular, depending on the specific application, they provide about 30-50% the performance of a real core.

Appendix B

List of Activities

List of publications relative to the results presented in this Thesis

- A. Iorio, G. Camisasca, P. Gallo, *Dynamics of hydration water in a multicomponent solution with DMSO and trehalose for cryopreservation*, In preparation.
- A. Iorio, G. Camisasca, P. Gallo, *Glassy dynamics of water at interface with biomolecules: a Mode Coupling Theory test*, Submitted (2018).
- A. Iorio, G. Camisasca, P. Gallo, *Slow dynamics of hydration water and the trehalose dynamical transition*, Submitted (2018).
- G. Camisasca, A. Iorio, M. De Marzio, P. Gallo, *Structure and slow dynamics of protein hydration water*, *Journal of Molecular Liquids*, vol. 268, pp. 903-910, 2018.

List of Schools and Conferences

- *Water and Water Systems - The hydrophobic effect*, Erice, July 2018. Poster and oral contribution.
- *8th International Discussion Meeting on Relaxations in Complex Systems*, Wisła, July 2017. Poster contribution.
- *Roma Tre Congress on Water under Extreme Conditions 2017*, Roma, June 2017. Poster contribution and member of the Local Organizing Committee.

- *Frontiers in Water Biophysics 2017*, Erice, May 2017. Poster contribution.

Attended Schools

- *25th Summer School on Parallel Computing*, CINECA, Roma 2017.
- *CCP5 Methods in Molecular Simulation Summer School*, Lancaster 2018.

Bibliography

- [1] P. Gallo, K. Amann-Winkel, C. A. Angell, M. A. Anisimov, F. Caupin, C. Chakravarty, E. Lascaris, T. Loerting, A. Z. Panagiotopoulos, J. Russo, J. A. Sellberg, H. E. Stanley, H. Tanaka, C. Vega, L. Xu, and L. G. M. Pettersson, “Water: A Tale of Two Liquids,” *Chemical Reviews*, vol. 116, no. 13, pp. 7463–7500, 2016. PMID: 27380438.
- [2] Mishima Osamu and Stanley H. Eugene, “The relationship between liquid, supercooled and glassy water,” *Nature*, vol. 396, pp. 329–335, nov 1998. 10.1038/24540.
- [3] P. G. Debenedetti, “Supercooled and glassy water,” *Journal of Physics: Condensed Matter*, vol. 15, no. 45, p. R1669, 2003.
- [4] P. H. Poole, F. Sciortino, T. Grande, H. E. Stanley, and C. A. Angell, “Effect of hydrogen bonds on the thermodynamic behavior of liquid water,” *Phys. Rev. Lett.*, vol. 73, pp. 1632–1635, Sep 1994.
- [5] T. M. Truskett, P. G. Debenedetti, S. Sastry, and S. Torquato, “A single-bond approach to orientation-dependent interactions and its implications for liquid water,” *The Journal of Chemical Physics*, vol. 111, no. 6, pp. 2647–2656, 1999.
- [6] W. Götze, *Complex dynamics of glass-forming liquids: a mode-coupling theory*. International series of monographs on physics, Oxford: Oxford University Press, 2008.
- [7] P. Gallo, F. Sciortino, P. Tartaglia, and S. Chen, “Slow dynamics of water molecules in supercooled states,” *Phys. Rev. Lett.*, vol. 76, pp. 2730–2733, Apr 1996.
- [8] F. Sciortino, P. Gallo, P. Tartaglia, and S. H. Chen, “Supercooled water and the kinetic glass transition,” *Phys. Rev. E*, vol. 54, pp. 6331–6343, Dec 1996.

- [9] M. Allen and D. Tildesley, *Computer Simulation of Liquids*. Oxford Science Publ, Clarendon Press, 1989.
- [10] L. Cordone, G. Cottone, A. Cupane, A. Emanuele, S. G. Levantino, and Matteo, "Proteins in saccharides matrices and the trehalose peculiarity: Biochemical and biophysical properties," *Current Organic Chemistry*, vol. 19, no. 17, pp. 1684–1706, 2015.
- [11] A. Magno and P. Gallo, "Understanding the mechanisms of bioprotection: A comparative study of aqueous solutions of trehalose and maltose upon supercooling," *The Journal of Physical Chemistry Letters*, vol. 2, no. 9, pp. 977–982, 2011.
- [12] D. Corradini, E. G. Strekalova, H. E. Stanley, and P. Gallo, "Microscopic mechanism of protein cryopreservation in an aqueous solution with trehalose," *Scientific Reports*, vol. 3, pp. 1218 EP –, Feb 2013. Article.
- [13] P. S. Belton and A. M. Gil, "Ir and raman spectroscopic studies of the interaction of trehalose with hen egg white lysozyme," *Biopolymers*, vol. 34, no. 7, pp. 957–961, 1994.
- [14] J. B. Hasted, *Liquid Water: Dielectric Properties*, pp. 255–309. Boston, MA: Springer New York, 1972.
- [15] D. Eisenberg and W. Kauzmann, *The structure and properties of water*. Oxford University Press on Demand, 1996.
- [16] F. Martin and H. Zipse, "Charge distribution in the water molecule-A comparison of methods," *Journal of Computational Chemistry*, vol. 26, no. 1, pp. 97–105, 2005.
- [17] F. J. Lovas, "Microwave spectral tables II. Triatomic molecules," *Journal of Physical and Chemical Reference Data*, vol. 7, no. 4, pp. 1445–1750, 1978.
- [18] W. C. Cmglee, "Phase diagram of water as a log-lin chart with pressure from 1 pa to 1 tpa and temperature from 0 k to 650," 2017. https://it.wikipedia.org/wiki/file:phase_diagram_of_water.svg.
- [19] T. Loerting, C. Salzmann, I. Kohl, E. Mayer, and A. Hallbrucker, "A second distinct structural "state" of high-density amorphous ice at 77 k and 1 bar," *Phys. Chem. Chem. Phys.*, vol. 3, pp. 5355–5357, 2001.

- [20] P. Ball, "Water - an enduring mystery," *Nature*, vol. 452, pp. 291 EP –, Mar 2008.
- [21] P. G. Debenedetti, *Metastable liquids: concepts and principles*. Princeton University Press, 1996.
- [22] P. Debenedetti and H. Stanley, "Supercooled and glassy water," *Physics Today*, vol. 56, pp. 40–46, 1 2003.
- [23] C. A. Angell, J. Shuppert, and J. C. Tucker, "Anomalous properties of supercooled water. Heat capacity, expansivity, and proton magnetic resonance chemical shift from 0 to -38%," *The Journal of Physical Chemistry*, vol. 77, no. 26, pp. 3092–3099, 1973.
- [24] C. A. ANGELL and H. KANNO, "Density maxima in high-pressure supercooled water and liquid silicon dioxide," *Science*, vol. 193, no. 4258, pp. 1121–1122, 1976.
- [25] R. Speedy and C. Angell, "Isothermal compressibility of supercooled water and evidence for a thermodynamic singularity at -45°C," *Journal of Chemical Physics*, vol. 65, no. 3, pp. 851–858, 1976.
- [26] A. Cavagna, "Supercooled liquids for pedestrians," *Physics Reports*, vol. 476, no. 4, pp. 51 – 124, 2009.
- [27] Johari G. P., Hallbrucker Andreas, and Mayer Erwin, "The glass-liquid transition of hyperquenched water," *Nature*, vol. 330, pp. 552–553, dec 1987. 10.1038/330552a0.
- [28] A. Hallbrucker, E. Mayer, and G. P. Johari, "Glass-liquid transition and the enthalpy of devitrification of annealed vapor-deposited amorphous solid water: a comparison with hyperquenched glassy water," *The Journal of Physical Chemistry*, vol. 93, no. 12, pp. 4986–4990, 1989.
- [29] V. Velikov, S. Borick, and C. A. Angell, "The Glass Transition of Water, Based on Hyperquenching Experiments," *Science*, vol. 294, no. 5550, pp. 2335–2338, 2001.
- [30] C. A. Angell, "Liquid Fragility and the Glass Transition in Water and Aqueous Solutions," *Chemical Reviews*, vol. 102, no. 8, pp. 2627–2650, 2002. PMID: 12175262.

- [31] O. Mishima, L. D. Calvert, and E. Whalley, "An apparently first-order transition between two amorphous phases of ice induced by pressure," *Nature*, vol. 314, pp. 76 EP –, Mar 1985.
- [32] M. M. Koza, H. Schober, H. E. Fischer, T. Hansen, and F. Fujara, "Kinetics of the high- to low-density amorphous water transition," *Journal of Physics: Condensed Matter*, vol. 15, no. 3, p. 321, 2003.
- [33] O. Mishima and Y. Suzuki, "Propagation of the polyamorphic transition of ice and the liquid-liquid critical point," *Nature*, vol. 419, pp. 599 EP –, Oct 2002.
- [34] Poole Peter H., Sciortino Francesco, Essmann Ulrich, and Stanley H. Eugene, "Phase behaviour of metastable water," *Nature*, vol. 360, pp. 324–328, nov 1992. 10.1038/360324a0.
- [35] S. Sastry, P. G. Debenedetti, F. Sciortino, and H. E. Stanley, "Singularity-free interpretation of the thermodynamics of supercooled water," *Phys. Rev. E*, vol. 53, pp. 6144–6154, Jun 1996.
- [36] C. A. Angell, "Insights into phases of liquid water from study of its unusual glass-forming properties," *Science*, vol. 319, no. 5863, pp. 582–587, 2008.
- [37] P. Gallo and H. E. Stanley, "Supercooled water reveals its secrets," *Science*, vol. 358, no. 6370, pp. 1543–1544, 2017.
- [38] K. H. Kim, A. Späh, H. Pathak, F. Perakis, D. Mariedahl, K. Amann-Winkel, J. A. Sellberg, J. H. Lee, S. Kim, J. Park, K. H. Nam, T. Katayama, and A. Nilsson, "Maxima in the thermodynamic response and correlation functions of deeply supercooled water," *Science*, vol. 358, no. 6370, pp. 1589–1593, 2017.
- [39] F. Franks and R. S. o. C. G. Britain), *Water: A Matrix of Life*. RSC paperbacks, Royal Society of Chemistry, 2000.
- [40] J. H. Crowe, L. M. Crowe, and S. A. Jackson, "Preservation of structural and functional activity in lyophilized sarcoplasmic reticulum," *Archives of Biochemistry and Biophysics*, vol. 220, no. 2, pp. 477 – 484, 1983.
- [41] J. L. Green and C. A. Angell, "Phase relations and vitrification in saccharide-water solutions and the trehalose anomaly," *The Journal of Physical Chemistry*, vol. 93, no. 8, pp. 2880–2882, 1989.

- [42] M. V. Fedorov, J. M. Goodman, D. Nerukh, and S. Schumm, "Self-assembly of trehalose molecules on a lysozyme surface: the broken glass hypothesis," *Phys. Chem. Chem. Phys.*, vol. 13, pp. 2294–2299, 2011.
- [43] L. Zhang, L. Wang, Y.-T. Kao, W. Qiu, Y. Yang, O. Okobiah, and D. Zhong, "Mapping hydration dynamics around a protein surface," *Proceedings of the National Academy of Sciences*, vol. 104, no. 47, pp. 18461–18466, 2007.
- [44] T. Li, A. A. Hassanali, Y.-T. Kao, D. Zhong, and S. J. Singer, "Hydration dynamics and time scales of coupled water-protein fluctuations," *Journal of the American Chemical Society*, vol. 129, no. 11, pp. 3376–3382, 2007.
- [45] A. Paciaroni, E. Cornicchi, M. Marconi, A. Orecchini, C. Petrillo, M. Haertlein, M. Moulin, and F. Sacchetti, "Coupled relaxations at the protein-water interface in the picosecond time scale," *J R Soc Interface*, vol. 6, pp. S635–S640, Oct 2009. rsif20090182[PII].
- [46] D. Ringe and G. A. Petsko, "The 'glass transition' in protein dynamics: what it is, why it occurs, and how to exploit it," *Biophysical Chemistry*, vol. 105, no. 2, pp. 667 – 680, 2003. Walter Kauzmann's 85th Birthday.
- [47] P. W. Fenimore, H. Frauenfelder, B. H. McMahon, and R. D. Young, "Bulk-solvent and hydration-shell fluctuations, similar to a- and b-fluctuations in glasses, control protein motions and functions," *Proc Natl Acad Sci U S A*, vol. 101, pp. 14408–14413, Oct 2004. 10114408[PII].
- [48] B. F. Rasmussen, A. M. Stock, D. Ringe, and G. A. Petsko, "Crystalline ribonuclease a loses function below the dynamical transition at 220 k," *Nature*, vol. 357, pp. 423 EP –, Jun 1992.
- [49] S. Chen, L. Liu, E. Fratini, P. Baglioni, A. Faraone, and E. Mamontov, "Observation of fragile-to-strong dynamic crossover in protein hydration water," *Proceedings of the National Academy of Sciences*, vol. 103, no. 24, pp. 9012–9016, 2006.
- [50] G. Schirò, M. Fomina, and A. Cupane, "Communication: Protein dynamical transition vs. liquid-liquid phase transition in protein hydration water," *The Journal of Chemical Physics*, vol. 139, no. 12, p. 121102, 2013.

- [51] K. Wood, A. Frölich, A. Paciaroni, M. Moulin, M. Härtlein, G. Zaccai, D. J. Tobias, and M. Weik, “Coincidence of dynamical transitions in a soluble protein and its hydration water: direct measurements by neutron scattering and md simulations,” *Journal of the American Chemical Society*, vol. 130, no. 14, pp. 4586–4587, 2008. PMID: 18338890.
- [52] G. Schirò, Y. Fichou, F.-X. Gallat, K. Wood, F. Gabel, M. Moulin, M. Härtlein, M. Heyden, J.-P. Colletier, A. Orecchini, A. Paciaroni, J. Wuttke, D. J. Tobias, and M. Weik, “Translational diffusion of hydration water correlates with functional motions in folded and intrinsically disordered proteins,” *Nature Communications*, vol. 6, pp. 6490 EP –, Mar 2015. Article.
- [53] P. Kumar, Z. Yan, L. Xu, M. G. Mazza, S. V. Buldyrev, S. Chen, S. Sastry, and H. E. Stanley, “Glass transition in biomolecules and the liquid-liquid critical point of water,” *Phys. Rev. Lett.*, vol. 97, p. 177802, Oct 2006.
- [54] M. Lagi, X. Chu, C. Kim, F. Mallamace, P. Baglioni, and S.-H. Chen, “The low-temperature dynamic crossover phenomenon in protein hydration water: Simulations vs experiments,” *The Journal of Physical Chemistry B*, vol. 112, no. 6, pp. 1571–1575, 2008. PMID: 18205352.
- [55] A. G. Markelz, J. R. Knab, J. Y. Chen, and Y. He, “Protein dynamical transition in terahertz dielectric response,” *Chemical Physics Letters*, vol. 442, no. 4, pp. 413 – 417, 2007.
- [56] A. Paciaroni, S. Cinelli, and G. Onori, “Effect of the environment on the protein dynamical transition: A neutron scattering study,” *Biophysical Journal*, vol. 83, no. 2, pp. 1157 – 1164, 2002.
- [57] E. Cornicchi, M. Marconi, G. Onori, and A. Paciaroni, “Controlling the protein dynamical transition with sugar-based bioprotectant matrices: a neutron scattering study,” *Biophys J*, vol. 91, pp. 289–297, Jul 2006. 16617083[pmid].
- [58] R. Zwanzig, “Memory effects in irreversible thermodynamics,” *Phys. Rev.*, vol. 124, pp. 983–992, Nov 1961.
- [59] H. Mori, “Transport, collective motion, and brownian motion,” *Progress of Theoretical Physics*, vol. 33, no. 3, pp. 423–455, 1965.

- [60] D. R. Reichman and P. Charbonneau, “Mode-coupling theory,” *Journal of Statistical Mechanics: Theory and Experiment*, vol. 2005, no. 05, p. P05013, 2005.
- [61] L. M. C. Janssen, “Mode-coupling theory of the glass transition: A primer,” *Frontiers in Physics*, vol. 6, p. 97, 2018.
- [62] W. Gotze and L. Sjogren, “Scaling properties in supercooled liquids near the glass transition,” *Journal of Physics C: Solid State Physics*, vol. 21, no. 18, p. 3407, 1988.
- [63] J. Hansen and I. McDonald, *Theory of Simple Liquids*. Academic Press, 2006.
- [64] U. Bengtzelius, W. Gotze, and A. Sjolander, “Dynamics of supercooled liquids and the glass transition,” *Journal of Physics C: Solid State Physics*, vol. 17, no. 33, p. 5915, 1984.
- [65] F. H. Stillinger and P. G. Debenedetti, “Glass transition thermodynamics and kinetics,” *Annual Review of Condensed Matter Physics*, vol. 4, no. 1, pp. 263–285, 2013.
- [66] W. Kob and H. C. Andersen, “Testing mode-coupling theory for a supercooled binary lennard-jones mixture i: The van hove correlation function,” *Phys. Rev. E*, vol. 51, pp. 4626–4641, May 1995.
- [67] W. Kob and H. C. Andersen, “Testing mode-coupling theory for a supercooled binary lennard-jones mixture. ii. intermediate scattering function and dynamic susceptibility,” *Phys. Rev. E*, vol. 52, pp. 4134–4153, Oct 1995.
- [68] P. Gallo and M. Rovere, “Mode coupling and fragile to strong transition in supercooled tip4p water,” *The Journal of Chemical Physics*, vol. 137, no. 16, p. 164503, 2012.
- [69] F. W. Starr, J. K. Nielsen, and H. E. Stanley, “Hydrogen-bond dynamics for the extended simple point-charge model of water,” *Phys. Rev. E*, vol. 62, pp. 579–587, Jul 2000.
- [70] M. De Marzio, G. Camisasca, M. Rovere, and P. Gallo, “Mode coupling theory and fragile to strong transition in supercooled tip4p/2005 water,” *The Journal of Chemical Physics*, vol. 144, no. 7, p. 074503, 2016.

- [71] L. Xu, P. Kumar, S. V. Buldyrev, S. Chen, P. H. Poole, F. Sciortino, and H. E. Stanley, "Relation between the Widom line and the dynamic crossover in systems with a liquid-liquid phase transition," *Proceedings of the National Academy of Sciences of the United States of America*, vol. 102, no. 46, pp. 16558–16562, 2005.
- [72] L. Liu, S.-H. Chen, A. Faraone, C.-W. Yen, and C.-Y. Mou, "Pressure dependence of fragile-to-strong transition and a possible second critical point in supercooled confined water," *Phys. Rev. Lett.*, vol. 95, p. 117802, Sep 2005.
- [73] P. Gallo, M. Rovere, and S. Chen, "Dynamic Crossover in Supercooled Confined Water: Understanding Bulk Properties through Confinement," *The Journal of Physical Chemistry Letters*, vol. 1, no. 4, pp. 729–733, 2010.
- [74] B. J. Alder and T. E. Wainwright, "Studies in Molecular Dynamics. I. General Method," *The Journal of Chemical Physics*, vol. 31, no. 2, pp. 459–466, 1959.
- [75] A. Rahman, "Correlations in the Motion of Atoms in Liquid Argon," *Phys. Rev.*, vol. 136, pp. A405–A411, Oct 1964.
- [76] H. J. C. Berendsen, J. P. M. Postma, W. F. van Gunsteren, A. DiNola, and J. R. Haak, "Molecular dynamics with coupling to an external bath," *The Journal of Chemical Physics*, vol. 81, no. 8, pp. 3684–3690, 1984.
- [77] Y. Liu, A. Z. Panagiotopoulos, and P. G. Debenedetti, "Low-temperature fluid-phase behavior of ST2 water," *The Journal of Chemical Physics*, vol. 131, no. 10, p. 104508, 2009.
- [78] H. J. C. Berendsen, J. R. Grigera, and T. P. Straatsma, "The missing term in effective pair potentials," *The Journal of Physical Chemistry*, vol. 91, no. 24, pp. 6269–6271, 1987.
- [79] A. D. MacKerell, D. Bashford, M. Bellott, R. L. Dunbrack, J. D. Evanseck, M. J. Field, S. Fischer, J. Gao, H. Guo, S. Ha, D. Joseph-McCarthy, L. Kuchnir, K. Kuczera, F. T. K. Lau, C. Mattos, S. Michnick, T. Ngo, D. T. Nguyen, B. Prodhom, W. E. Reiher, B. Roux, M. Schlenkrich, J. C. Smith, R. Stote, J. Straub, M. Watanabe, J. Wiórkiewicz-Kuczera, D. Yin, and M. Karplus, "All-atom empirical potential for molecular modeling and dynamics studies of proteins,"

The Journal of Physical Chemistry B, vol. 102, no. 18, pp. 3586–3616, 1998. PMID: 24889800.

- [80] A. D. Mackerell, M. Feig, and C. L. Brooks, “Extending the treatment of backbone energetics in protein force fields: Limitations of gas-phase quantum mechanics in reproducing protein conformational distributions in molecular dynamics simulations,” *Journal of Computational Chemistry*, vol. 25, no. 11, pp. 1400–1415, 2004.
- [81] N. Foloppe and A. D. MacKerell, Jr., “All-atom empirical force field for nucleic acids: I. parameter optimization based on small molecule and condensed phase macromolecular target data,” *Journal of Computational Chemistry*, vol. 21, no. 2, pp. 86–104, 2000.
- [82] S. E. Feller and A. D. MacKerell, “An improved empirical potential energy function for molecular simulations of phospholipids,” *The Journal of Physical Chemistry B*, vol. 104, no. 31, pp. 7510–7515, 2000.
- [83] O. Guvench, S. N. Greene, G. Kamath, J. W. Brady, R. M. Venable, R. W. Pastor, and A. D. MacKerell, “Additive empirical force field for hexopyranose monosaccharides,” *J Comput Chem*, vol. 29, pp. 2543–2564, Nov 2008. 18470966[pmid].
- [84] O. Guvench, E. R. Hatcher, R. M. Venable, R. W. Pastor, and A. D. MacKerell, “Charmm additive all-atom force field for glycosidic linkages between hexopyranoses,” *J Chem Theory Comput*, vol. 5, pp. 2353–2370, Aug 2009. 20161005[pmid].
- [85] R. Metzler and J. Klafter, “The random walk’s guide to anomalous diffusion: a fractional dynamics approach,” *Physics Reports*, vol. 339, no. 1, pp. 1 – 77, 2000.
- [86] P. Kumar, K. T. Wikfeldt, D. Schlesinger, L. G. M. Pettersson, and H. E. Stanley, “The boson peak in supercooled water,” *Scientific Reports*, vol. 3, pp. 1980 EP –, Jun 2013. Article.
- [87] Z. Wang, K.-H. Liu, P. Le, M. Li, W.-S. Chiang, J. B. Leão, J. R. D. Copley, M. Tyagi, A. Podlesnyak, A. I. Kolesnikov, C.-Y. Mou, and S.-H. Chen, “Boson peak in deeply cooled confined water: A possible way to explore the existence of the liquid-to-liquid transition in water,” *Phys. Rev. Lett.*, vol. 112, p. 237802, Jun 2014.

- [88] A. Cupane, M. Fomina, and G. Schirò, “The boson peak of deeply cooled confined water reveals the existence of a low-temperature liquid-liquid crossover,” *The Journal of Chemical Physics*, vol. 141, no. 18, p. 18C510, 2014.
- [89] Z. Wang, A. I. Kolesnikov, K. Ito, A. Podlesnyak, and S.-H. Chen, “Pressure effect on the boson peak in deeply cooled confined water: Evidence of a liquid-liquid transition,” *Phys. Rev. Lett.*, vol. 115, p. 235701, Dec 2015.
- [90] F. Mallamace, C. Corsaro, D. Mallamace, Z. Wang, and S.-H. Chen, “The boson peak in confined water: An experimental investigation of the liquid-liquid phase transition hypothesis,” *Frontiers of Physics*, vol. 10, p. 106103, Dec 2015.
- [91] P. Gallo, M. Rapinesi, and M. Rovere, “Confined water in the low hydration regime,” *The Journal of Chemical Physics*, vol. 117, no. 1, pp. 369–375, 2002.
- [92] J. R. Errington and P. G. Debenedetti, “Relationship between structural order and the anomalies of liquid water,” *Nature*, vol. 409, pp. 318 EP –, Jan 2001.
- [93] A. Iorio, G. Camisasca, and P. Gallo, “Slow dynamics of hydration water and the trehalose dynamical transition,” Submitted, 2018.
- [94] B. Hess, C. Kutzner, D. van der Spoel, and E. Lindahl, “GROMACS 4: Algorithms for Highly Efficient, Load-Balanced, and Scalable Molecular Simulation,” *Journal of Chemical Theory and Computation*, vol. 4, no. 3, pp. 435–447, 2008. PMID: 26620784.
- [95] B. R. Brooks, C. L. Brooks, A. D. MacKerell, L. Nilsson, R. J. Petrella, B. Roux, Y. Won, G. Archontis, C. Bartels, S. Boresch, A. Caffisch, L. Caves, Q. Cui, A. R. Dinner, M. Feig, S. Fischer, J. Gao, M. Hodoscek, W. Im, K. Kuczera, T. Lazaridis, J. Ma, V. Ovchinnikov, E. Paci, R. W. Pastor, C. B. Post, J. Z. Pu, M. Schaefer, B. Tidor, R. M. Venable, H. L. Woodcock, X. Wu, W. Yang, D. M. York, and M. Karplus, “Charmm: The biomolecular simulation program,” *J Comput Chem*, vol. 30, pp. 1545–1614, Jul 2009. 19444816[pmid].
- [96] L. A. Báez and P. Clancy, “Existence of a density maximum in extended simple point charge water,” *The Journal of Chemical Physics*, vol. 101, no. 11, pp. 9837–9840, 1994.

- [97] D. Corradini, M. Rovere, and P. Gallo, "A route to explain water anomalies from results on an aqueous solution of salt," *The Journal of Chemical Physics*, vol. 132, no. 13, p. 134508, 2010.
- [98] D. Corradini, Z. Su, H. E. Stanley, and P. Gallo, "A molecular dynamics study of the equation of state and the structure of supercooled aqueous solutions of methanol," *The Journal of Chemical Physics*, vol. 137, no. 18, p. 184503, 2012.
- [99] G. Camisasca, M. De Marzio, D. Corradini, and P. Gallo, "Two structural relaxations in protein hydration water and their dynamic crossovers," *The Journal of Chemical Physics*, vol. 145, no. 4, p. 044503, 2016.
- [100] G. Camisasca, A. Iorio, M. D. Marzio, and P. Gallo, "Structure and slow dynamics of protein hydration water," *Journal of Molecular Liquids*, vol. 268, pp. 903 – 910, 2018.
- [101] L. Lupi, L. Comez, M. Paolantoni, S. Perticaroli, P. Sassi, A. Morresi, B. M. Ladanyi, and D. Fioretto, "Hydration and aggregation in mono- and disaccharide aqueous solutions by gigahertz-to-terahertz light scattering and molecular dynamics simulations," *The Journal of Physical Chemistry B*, vol. 116, no. 51, pp. 14760–14767, 2012. PMID: 23205713.
- [102] S. Corezzi, P. Sassi, M. Paolantoni, L. Comez, A. Morresi, and D. Fioretto, "Hydration and rotational diffusion of levoglucosan in aqueous solutions," *The Journal of Chemical Physics*, vol. 140, no. 18, p. 184505, 2014.
- [103] D. Fioretto, L. Comez, S. Corezzi, M. Paolantoni, P. Sassi, and A. Morresi, "Solvent sharing models for non-interacting solute molecules: The case of glucose and trehalose water solutions," *Food Biophysics*, vol. 8, pp. 177–182, Sep 2013.
- [104] P. M. Mehl, "Solubility and glass transition in the system α -d-trehalose/water," *Journal of thermal analysis*, vol. 49, pp. 817–822, Aug 1997.
- [105] A. Paciaroni, A. R. Bizzarri, and S. Cannistraro, "Neutron scattering evidence of a boson peak in protein hydration water," *Phys. Rev. E*, vol. 60, pp. R2476–R2479, Sep 1999.

- [106] A. Paciaroni, A. R. Bizzarri, and S. Cannistraro, “Molecular-dynamics simulation evidences of a boson peak in protein hydration water,” *Phys. Rev. E*, vol. 57, pp. R6277–R6280, Jun 1998.
- [107] S. Perticaroli, J. D. Nickels, G. Ehlers, and A. P. Sokolov, “Rigidity, secondary structure, and the universality of the boson peak in proteins,” *Biophys J*, vol. 106, pp. 2667–2674, Jun 2014. 24940784[pmid].
- [108] M. Paolantoni, L. Comez, M. E. Gallina, P. Sassi, F. Scarponi, D. Fioretto, and A. Morresi, “Light scattering spectra of water in trehalose aqueous solutions: Evidence for two different solvent relaxation processes,” *The Journal of Physical Chemistry B*, vol. 113, no. 22, pp. 7874–7878, 2009. PMID: 19422249.
- [109] L. Comez, L. Lupi, A. Morresi, M. Paolantoni, P. Sassi, and D. Fioretto, “More is different: Experimental results on the effect of biomolecules on the dynamics of hydration water,” *The Journal of Physical Chemistry Letters*, vol. 4, no. 7, pp. 1188–1192, 2013. PMID: 26282040.
- [110] F. Mallamace, S.-H. Chen, M. Broccio, C. Corsaro, V. Crupi, D. Majolino, V. Venuti, P. Baglioni, E. Fratini, C. Vannucci, and H. E. Stanley, “Role of the solvent in the dynamical transitions of proteins: The case of the lysozyme-water system,” *The Journal of Chemical Physics*, vol. 127, no. 4, p. 045104, 2007.
- [111] F. W. Starr, F. Sciortino, and H. E. Stanley, “Dynamics of simulated water under pressure,” *Phys. Rev. E*, vol. 60, pp. 6757–6768, Dec 1999.
- [112] Y. Xu, N. G. Petrik, R. S. Smith, B. D. Kay, and G. A. Kimmel, “Growth rate of crystalline ice and the diffusivity of supercooled water from 126 to 262 k,” *Proceedings of the National Academy of Sciences*, vol. 113, no. 52, pp. 14921–14925, 2016.
- [113] M. D. Marzio, G. Camisasca, M. M. Conde, M. Rovere, and P. Gallo, “Structural properties and fragile to strong transition in confined water,” *The Journal of Chemical Physics*, vol. 146, no. 8, p. 084505, 2017.
- [114] F. Mallamace, M. Broccio, C. Corsaro, A. Faraone, U. Wanderlingh, L. Liu, C. Mou, and S. H. Chen, “The fragile-to-strong dynamic crossover transition in confined water: nuclear magnetic resonance results,” *The Journal of Chemical Physics*, vol. 124, no. 16, p. 161102, 2006.

- [115] P. Gallo, D. Corradini, and M. Rovere, “Fragile to strong crossover at the widom line in supercooled aqueous solutions of nacl,” *The Journal of Chemical Physics*, vol. 139, no. 20, p. 204503, 2013.
- [116] S. K. Ramadugu, Y.-H. Chung, J. Xia, and C. J. Margulis, “When sugars get wet. a comprehensive study of the behavior of water on the surface of oligosaccharides,” *The Journal of Physical Chemistry B*, vol. 113, no. 31, pp. 11003–11015, 2009. PMID: 19588947.
- [117] M. Zanatta, L. Tavagnacco, E. Buratti, M. Bertoldo, F. Natali, E. Chiessi, A. Orecchini, and E. Zaccarelli, “Evidence of a low-temperature dynamical transition in concentrated microgels,” *Science Advances*, vol. 4, no. 9, 2018.
- [118] A. R. Bizzarri, A. Paciaroni, and S. Cannistraro, “Glasslike dynamical behavior of the plastocyanin hydration water,” *Phys. Rev. E*, vol. 62, pp. 3991–3999, Sep 2000.
- [119] E. Yamamoto, T. Akimoto, M. Yasui, and K. Yasuoka, “Origin of sub-diffusion of water molecules on cell membrane surfaces,” *Scientific Reports*, vol. 4, pp. 4720 EP –, Apr 2014. Article.
- [120] S. Magazù, G. Maisano, F. Migliardo, and C. Mondelli, “Mean-square displacement relationship in bioprotectant systems by elastic neutron scattering,” *Biophysical Journal*, vol. 86, no. 5, pp. 3241 – 3249, 2004.
- [121] S. Magazù, G. Maisano, F. Migliardo, C. Mondelli, and G. Romeo, “An elastic neutron scattering on dynamical transition in hydrogen-bonded systems,” *Journal of Molecular Structure*, vol. 700, no. 1, pp. 225 – 227, 2004. Horizons in Hydrogen Bond Research 2003. A collection of Papers from the XVth International Conference.
- [122] M. De Marzio, G. Camisasca, M. Rovere, and P. Gallo, “Fragile to strong crossover and widom line in supercooled water: A comparative study,” *Frontiers of Physics*, vol. 13, p. 136103, Nov 2017.
- [123] F. Mallamace, C. Branca, C. Corsaro, N. Leone, J. Spooren, H. E. Stanley, and S.-H. Chen, “Dynamical crossover and breakdown of the stokes-einstein relation in confined water and in methanol-diluted bulk water,” *The Journal of Physical Chemistry B*, vol. 114, no. 5, pp. 1870–1878, 2010. PMID: 20058894.
- [124] F. Mallamace, C. Corsaro, P. Baglioni, E. Fratini, and S.-H. Chen, “The dynamical crossover phenomenon in bulk water, confined water

- and protein hydration water,” *Journal of Physics: Condensed Matter*, vol. 24, no. 6, p. 064103, 2012.
- [125] A. Iorio, G. Camisasca, and P. Gallo, “Dynamics of hydration water in a multicomponent solution with dmsO and trehalose for cryopreservation,” In preparation.
- [126] A. Idrissi, B. A. Marekha, M. Barj, F. A. Miannay, T. Takamuku, V. Raptis, J. Samios, and P. Jedlovszky, “Local structure of dilute aqueous dmsO solutions, as seen from molecular dynamics simulations,” *The Journal of Chemical Physics*, vol. 146, no. 23, p. 234507, 2017.
- [127] N. Zhang, W. Li, C. Chen, and J. Zuo, “Molecular dynamics simulation of aggregation in dimethyl sulfoxide–water binary mixture,” *Computational and Theoretical Chemistry*, vol. 1017, pp. 126 – 135, 2013.
- [128] S. Roy, S. Banerjee, N. Biyani, B. Jana, and B. Bagchi, “Theoretical and computational analysis of static and dynamic anomalies in water-dmsO binary mixture at low dmsO concentrations,” *The Journal of Physical Chemistry B*, vol. 115, no. 4, pp. 685–692, 2011. PMID: 21186810.
- [129] A. Luzar and D. Chandler, “Structure and hydrogen bond dynamics of water–dimethyl sulfoxide mixtures by computer simulations,” *The Journal of Chemical Physics*, vol. 98, no. 10, pp. 8160–8173, 1993.
- [130] J. Solocinski, Q. Osgood, M. Wang, A. Connolly, M. A. Menze, and N. Chakraborty, “Effect of trehalose as an additive to dimethyl sulfoxide solutions on ice formation, cellular viability, and metabolism,” *Cryobiology*, vol. 75, pp. 134 – 143, 2017.
- [131] G. Chen, A. Yue, Z. Ruan, Y. Yin, R. Wang, Y. Ren, and L. Zhu, “Comparison of the effects of different cryoprotectants on stem cells from umbilical cord blood,” *Stem Cells International*, vol. 2016, 2016.
- [132] J. B. Mandumpal, C. A. Kreck, and R. L. Mancera, “A molecular mechanism of solvent cryoprotection in aqueous dmsO solutions,” *Phys. Chem. Chem. Phys.*, vol. 13, pp. 3839–3842, 2011.
- [133] J. Lin, B. Novak, and D. Moldovan, “Molecular dynamics simulation study of the effect of dmsO on structural and permeation properties of dmpc lipid bilayers,” *The Journal of Physical Chemistry B*, vol. 116, no. 4, pp. 1299–1308, 2012. PMID: 22191390.

- [134] M. J. Abraham, T. Murtola, R. Schulz, S. Páll, J. C. Smith, B. Hess, and E. Lindahl, “GROMACS: High performance molecular simulations through multi-level parallelism from laptops to supercomputers,” *SoftwareX*, vol. 1–2, pp. 19–25, 2015.
- [135] V. Réat, R. Dunn, M. Ferrand, J. L. Finney, R. M. Daniel, and J. C. Smith, “Solvent dependence of dynamic transitions in protein solutions,” *Proceedings of the National Academy of Sciences*, vol. 97, no. 18, pp. 9961–9966, 2000.